

ADA 120817

12

ARL-TR-82-51

Copy No. 23

THE RISE TIME OF N WAVES  
PRODUCED BY SPARKS

Lori Beth Orenstein

APPLIED RESEARCH LABORATORIES  
THE UNIVERSITY OF TEXAS AT AUSTIN  
POST OFFICE BOX 8029, AUSTIN, TEXAS 78712-8029

5 October 1982

Technical Report

APPROVED FOR PUBLIC RELEASE;  
DISTRIBUTION UNLIMITED.

DTIC  
SERIALIZED  
OCT 28 1982  
H

Prepared for:

OFFICE OF NAVAL RESEARCH  
DEPARTMENT OF THE NAVY  
ARLINGTON, VA 22217



FILE COPY

82 10 3 054

UNCLASSIFIED

SECURITY CLASSIFICATION OF THIS PAGE (When Data Entered)

REPORT DOCUMENTATION PAGE		READ INSTRUCTIONS BEFORE COMPLETING FORM
1. REPORT NUMBER	2. GOVT ACCESSION NO.	3. RECIPIENT'S CATALOG NUMBER
	AD-A120817	
4. TITLE (and Subtitle) THE RISE TIME OF N WAVES PRODUCED BY SPARKS		5. TYPE OF REPORT & PERIOD COVERED Technical Report
		6. PERFORMING ORG. REPORT NUMBER ARL-TR-82-51
7. AUTHOR(s) Lori Beth Orenstein		8. CONTRACT OR GRANT NUMBER(s) N00014-75-C-0867
9. PERFORMING ORGANIZATION NAME AND ADDRESS Applied Research Laboratories The University of Texas at Austin Austin, Texas 78712		10. PROGRAM ELEMENT, PROJECT, TASK AREA & WORK UNIT NUMBERS
11. CONTROLLING OFFICE NAME AND ADDRESS Office of Naval Research Department of the Navy Arlington, Virginia 22217		12. REPORT DATE October 1982
		13. NUMBER OF PAGES 119
14. MONITORING AGENCY NAME & ADDRESS (if different from Controlling Office)		15. SECURITY CLASS. (of this report) UNCLASSIFIED
		15a. DECLASSIFICATION/DOWNGRADING SCHEDULE
16. DISTRIBUTION STATEMENT (of this Report)		
17. DISTRIBUTION STATEMENT (of the abstract entered in Block 20, if different from Report) Approved for public release; distribution unlimited.		
18. SUPPLEMENTARY NOTES		
19. KEY WORDS (Continue on reverse side if necessary and identify by block number)		
N wave electric spark amplitude rise time	half duration step shock thermoviscous gas relaxing gas	dispersion finite amplitude distortion
20. ABSTRACT (Continue on reverse side if necessary and identify by block number) The rise time of spark produced N waves in air has been measured with a microphone of very wide bandwidth. The purpose was to determine the extent to which vibrational relaxation affects the rise time. Electric sparks having energies between 0.06 J and 26.5 J were used. The N waves had pressure amplitudes in the range 0.15-15.0 mbar, half durations 7.5-41.5 $\mu$ sec, and rise times 0.65-7.0 $\mu$ sec. The measurements were taken at source-receiver distances of 0.1-5.5 m. Data were taken under three different conditions: constant spark energy, constant half duration, and constant amplitude.		

DTIC  
OCT 28 1982  
H

DD FORM 1 JAN 73 1473

EDITION OF 1 NOV 65 IS OBSOLETE

UNCLASSIFIED

SECURITY CLASSIFICATION OF THIS PAGE (When Data Entered)

\* MICROSEC

20. (cont'd.)

Theoretical predictions in common use for the rise time of a plane step shock in a thermoviscous gas and in a relaxing gas were reviewed. The measurements show, however, that these predictions are not really applicable to the head shock of our spherical N waves. An alternative theoretical prediction was obtained by using a computer algorithm to predict the waveform of a propagating N wave. The algorithm includes finite amplitude distortion, spherical spreading, absorption based on the ANSI standard for still air, and dispersion appropriate for oxygen relaxation. The predicted waveforms, including amplitude, half duration, and rise time, are in good agreement with the measured waveforms. Further computer calculations show that the measured rise times cannot be attributed to relaxation (including dispersion) or thermoviscous absorption alone. Both mechanisms are important for the N waves in our experiment.

Accession For	
NTIS GRA&I	<input checked="" type="checkbox"/>
DTIC TAB	<input type="checkbox"/>
Unannounced	<input type="checkbox"/>
Justification	
By _____	
Distribution/	
Availability Codes	
Dist	Avail and/or Special
A	



## FOREWORD

This technical report is an adaptation of the master's thesis of the same title by Lori B. Orenstein. Ms. Orenstein was enrolled in the Department of Mechanical Engineering of The University of Texas at Austin and received her degree in August 1982.

Since the printing of the thesis the author has made a few substantive revisions that are included in this report, primarily at the end of Chapter 5 and in Chapter 6. Correction of a small error in the calculation of dispersion in computer program LB01 (line 70; see Appendix B) led to a small improvement in the waveforms of the computed N waves. Figures 3.2 and 5.5 (and Table 5.2) were revised accordingly. Additional waveform computations, which allowed a comparison of the effects of thermoviscous absorption by itself, relaxation absorption (and dispersion) by itself, and combined thermoviscous and relaxation absorption (and dispersion), led to two new figures, Figs. 5.6 and 5.7, and a discussion of their implications. The new material strengthens the main conclusions in Chapter 6.

This research was carried out at Applied Research Laboratories and was supported by the Office of Naval Research under Contract N00014-75-C-0867. Scientific Officer for ONR was Dr. Logan E. Hargrove.

David T. Blackstock  
Supervisor

## TABLE OF CONTENTS

	<u>Page</u>
FOREWORD	iii
LIST OF FIGURES	ix
GLOSSARY OF IMPORTANT SYMBOLS	xi
CHAPTER 1 INTRODUCTION AND REVIEW OF THE LITERATURE	1
A. Introduction	1
B. Literature Review	5
1. Theoretical Literature	5
2. Experimental Literature	11
C. Outline of the Study	12
CHAPTER 2 ANALYTICAL PREDICTIONS	13
A. Introduction	13
B. Thermoviscous Model	14
C. Relaxation Model	18
D. Discussion	26
CHAPTER 3 WAVE PROPAGATION ALGORITHM	28
A. Introduction	28
B. Theory	28
1. Absorption	28
2. Nonlinear Distortion	30

PREVIOUS PAGE  
IS BLANK

	<u>Page</u>
C. Wave Propagation Algorithm	31
1. Driver Program	32
a. Input Scheme	32
b. Step Size Calculation	34
c. Application of Absorption	36
d. Application of Nonlinear Distortion	38
e. Data Output	39
2. Subroutines	39
a. DABSORP	39
b. RESAMP	40
c. NWPLOT	40
d. FQPLOT	41
3. Frequency Domain Analysis	41
D. Results	42
CHAPTER 4 EXPERIMENT	45
A. Apparatus	45
1. Spark Source	45
2. Optical Bench	47
3. Receiving System	47
4. Data Capture and Storage	56
B. Calibration	57
C. Alignment and Procedure	68
D. Limits on Rise Time Measurement Capability	70
CHAPTER 5 MEASUREMENTS AND COMPARISONS WITH THEORETICAL PREDICTIONS	74
A. Introduction	74

	<u>Page</u>
B. Comparison with Thermoviscous and Relaxation Models	74
1. Rise Time versus Inverse Peak Pressure	75
a. Constant Spark Energy	75
b. Constant Half Duration	78
c. Constant Amplitude	78
2. Slope of the Rise ( $m_1$ ) versus Peak Pressure Squared	81
a. Constant Spark Energy	81
b. Constant Half Duration	81
C. Comparison with Computer Propagation Algorithm	81
CHAPTER 6 CONCLUSIONS AND RECOMMENDATIONS FOR FURTHER WORK	89
APPENDIX A DERIVATION OF THE EQUATION OF STATE FOR A RELAXING MEDIUM <sup>28</sup>	93
APPENDIX B PROGRAM AND SUBROUTINE LISTINGS	96
REFERENCES	110

## LIST OF FIGURES

<u>Figure</u>		<u>Page</u>
1.1	N Wave Pressure Signature	2
2.1	Step Shock Profile in a Relaxing Medium	21
2.2	Rise Time Prediction	25
3.1	Flowchart of Computer Propagation Algorithm	33
3.2	Sample Computed Waveforms and Important Parameters	44
4.1	Experimental Arrangement	46
4.2	Electrode Configuration	48
4.3	Photograph of a Spark Discharge	49
4.4	Microphone and Preamplifier	52
4.5	Effects of Limited Frequency Response on an Ideal N Wave	55
4.6	Ideal N Wave (Above) and Idealization of Measured N Waves (Below)	60
4.7	Microphone Calibration Data (Old System)	61
4.8	Microphone Calibration Data (New System)	63
4.9	Flange for Calibration in 2 in. Tube	65
4.10	Tube Calibration Apparatus	66
4.11	Comparison Method Calibration Data	67
4.12	Definition of Rise Time	71
4.13	Sample Experimental Waveforms	72
5.1	First Method of Analysis: Constant Spark Energy	77
5.2	First Method of Analysis: Constant Half Duration	79
5.3	Constant Peak Amplitude Run	80

<u>Figure</u>		<u>Page</u>
5.4	Second Method of Comparison	82
5.5	Comparison of Measured and Computed Waveforms	84
5.6	Computed Waveform for Various Absorption Mechanisms	86
5.7	Rise Time versus Distance for Various Absorption Mechanisms	87

## GLOSSARY OF IMPORTANT SYMBOLS

$c$	vibrational specific heat
$c_0$	small signal, adiabatic sound speed
$c_f$	frozen sound speed
$c_{ph}$	phase speed
$f$	frequency
$f_s$	sampling frequency of FFT
$j$	$\sqrt{-1}$
$k$	$(\omega/c_0)$
$m$	dispersion, $(c_f^2 - c_0^2)/c_0^2$
$m_1$	slope of the initial rise at the midpoint
$m_2$	slope of the linear decay
$p$	total pressure
$p$	excess pressure (over ambient pressure)
$p_0$	ambient pressure
$r$	radial coordinate, source-receiver distance
$\Delta r$	step size
$t$	dimensional time coordinate
$t'$	retarded time
$t_r$	rise time
$u$	particle velocity
$v$	shock speed

x	axial coordinate
$\Delta x$	distance between microphones in tube calibration
z	spherical wave distance ( $r_0 \ln(r/r_0)$ )
$\bar{z}$	shock formation distance (spherical waves)
B	correction factor in comparison calibration
$C_{IN}$	input capacitance of preamplifier
D	ratio of parameters representing dispersion and nonlinearity
E	peak input voltage of N wave
$N_2$	nitrogen
$O_2$	oxygen
P	peak pressure amplitude ( $\Delta p$ )
$P_0$	peak pressure amplitude at position $r_0$
Pr	Prandtl number
S	sensitivity of preamplifier (mbar/V)
$\bar{S}$	sensitivity of preamplifier (dB re 1V/ $\mu$ bar)
T	half duration
$T_0$	half duration at position $r_0$
TV1	thermoviscous prediction with $\mu_v/\mu=0$
TV2	thermoviscous prediction with $\mu_v/\mu=0.6$
$\bar{U}$	particle velocity Fourier coefficient
$Z_{in}$	input impedance of preamplifier
$\alpha$	atmospheric absorption
$\beta$	coefficient of nonlinearity $(\gamma+1)/2$
$\gamma$	ratio of specific heats
$\gamma_e$	equilibrium ratio of specific heats
$\gamma_f$	frozen ratio of specific heats

$\delta$	diffusion coefficient
$\eta$	dispersion
$\theta_{HP}$	half power beamwidth
$\mu$	shear coefficient of viscosity
$\mu_V$	bulk viscosity
$\nu$	kinematic viscosity $\mu/c_0$
$\xi$	internal coordinate
$\rho$	density
$\rho_0$	ambient density
$\rho'$	$(\rho - \rho_0)$
$\sigma$	dimensionless distortion variable
$\tau$	relaxation time
$\omega$	angular frequency ( $2\pi f$ )
$\zeta$	$\alpha - j\eta$

1

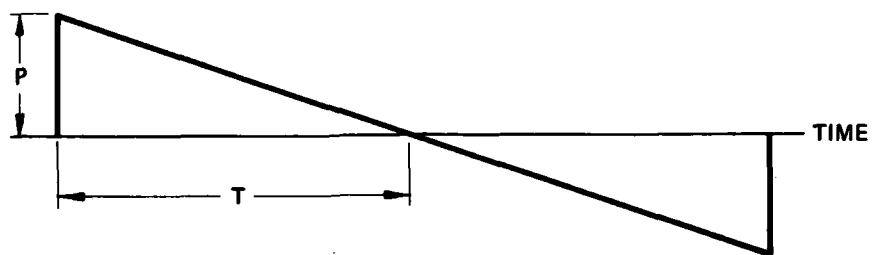
CHAPTER 1  
INTRODUCTION AND REVIEW OF THE LITERATURE

In this thesis we describe an experimental study of the rise time of spark produced, spherically spreading N waves of finite amplitude. The main purpose of the study was to determine the effects of oxygen and/or nitrogen relaxation on the rise time.

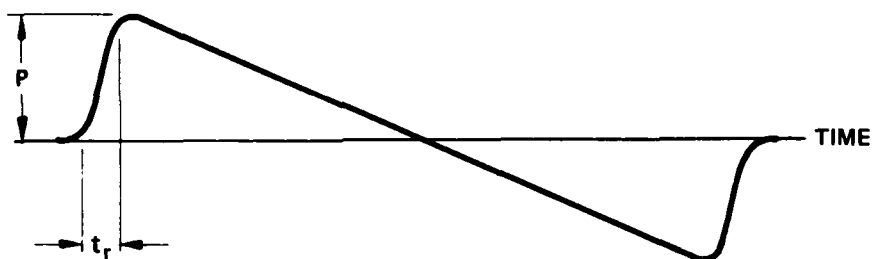
A. Introduction

The idealized pressure signature of an N wave is shown in Fig. 1(a). The wave begins with a condensation headed by a shock, which raises the local pressure above its ambient value. The amount the local pressure exceeds the ambient pressure is called the excess pressure and is denoted by the symbol  $p$ . Following the shock, the excess pressure decays linearly to a rarefaction. Finally, a tail shock returns the local pressure to its ambient value. The peak value of the excess pressure is called the amplitude and is denoted by the symbol  $P$ . The time elapsed in the condensation phase is called the half duration and is denoted by the symbol  $T$ . In reality, the shock portions of the waveform have a finite rise time  $t_r$ . A more realistic pressure signature of an N wave is shown in Fig. 1(b).

We chose to study only the condensation because for our N waves, that can be generated in the laboratory, the rarefaction is not a mirror image of the condensation. In particular, the tail shock is not as well formed as the head shock. In addition, the rarefaction phase is more likely to be contaminated with reflected and/or diffracted signals.



(a) IDEAL



(b) REAL

**FIGURE 1.1**  
**N WAVE PRESSURE SIGNATURE**

The spark produced N waves resemble the sonic boom pressure signal created by supersonic aircraft. Sonic boom waveforms have been observed to have extremely long rise times. The long rise times have been attributed to inhomogeneity of the atmosphere,<sup>1,2</sup> turbulence,<sup>3,4</sup> and oxygen and/or nitrogen relaxation.<sup>5,6</sup> In our spark experiments, which are carried out indoors in a laboratory, atmospheric inhomogeneity and turbulence are of course not present. We are therefore able to study the effect of relaxation by itself. There is another important difference between our spark produced N waveforms and actual sonic boom waveforms. Although we can accurately recreate the amplitude of a sonic boom, the half durations we observe are shorter by a factor  $10^{-4}$ .

According to lossless, linear theory, sound waves are propagated with constant energy and uniform wave velocity. However, the acoustic waveform of an N wave is in general altered from that predicted by lossless, linear theory by two sets of physical effects. The first set consists of the various absorption mechanisms. These include the molecular transport processes (viscosity, heat conduction, and species diffusion), rotational relaxation of nitrogen and oxygen molecules (modeled as bulk viscosity), and vibrational relaxation of nitrogen and oxygen molecules (caused by large departures from equilibrium in some of the internal degrees of freedom). The second set consists of the nonlinear propagation effects described in finite amplitude theory. These effects cause high amplitude sound waves to distort. There is a steepening of the compression phase of the waveform and an easing of the expansion phase. The absorption mechanisms tend to counteract the steepening process but aid the easing process. If the nonlinear effects

are strong enough, shocks form but, because of absorption, they have a finite rise time.

The N waves used in this study were created by sparks. The sparks were made by applying a potential across a capacitor and allowing it to discharge through an air gap between two electrodes. The amplitude and half duration of the N wave were altered by changing the potential applied, the capacitance, the length of the gap between the electrodes, and the distance between the spark source and the receiving apparatus. Each time the N wave was altered, we measured its amplitude, rise time, and half duration. The results were compared with the theoretical predictions.

Most theoretical predictions for N wave rise time are obtained from solutions for a steady or a step shock. The boundary conditions for a step shock are used, rather than those of an N wave, because the equations of motion are much more difficult to solve for an N wave. However, there is some question whether it is valid to compare our measured N wave rise times with rise times predicted for step shocks. An N wave only approximates a step shock in the limit as the half duration goes to infinity. If the half duration is very short, as in our case, a step shock is actually a poor approximation for an N wave.

Two different models are used to analytically predict the rise time, the thermoviscous model and the relaxation model. In the thermoviscous model, Burgers' equation is chosen to describe nonlinear propagation in a quiet thermoviscous gas. The absorption mechanisms considered are viscosity, heat conduction, species diffusion, and rotational relaxation of nitrogen and oxygen molecules. In some cases

Stokes's assumption is made and rotational relaxation is ignored. In the relaxation model, a "Burgers-like" equation is chosen to describe finite amplitude propagation in a relaxing gas. Because the form of this equation is known only for a mono-relaxing gas, the most dominant mode of relaxation must be chosen and, since the relaxation time for oxygen is much longer than that for nitrogen or carbon dioxide (except when the relative humidity is less than 10%), oxygen is assumed to be the dominant mode of relaxation. The other vibrational modes are said to be in equilibrium. Although thermoviscous effects may be included in the relaxation model, they are ignored in the model considered here.

Because of the questionable applicability of the step shock solutions to our N waves, we developed a computer algorithm which simulates finite amplitude propagation in quiet, but real, air. The wave propagation algorithm may be used for arbitrary signals, including our N waves. The ANSI standard S1.26-1978<sup>7</sup> was used to specify the effects of viscosity, heat conduction, rotational relaxation, vibrational relaxation of oxygen and nitrogen molecules, and dispersion due to oxygen relaxation. The theory of finite amplitude waves was used to determine the nonlinear propagation effects. Spherical spreading was also included in the algorithm. Given the initial waveform and the propagation distance, we were able to predict the local waveform and also the rise time.

## B. Literature Review

### 1. Theoretical Literature

The theoretical approach to nonlinear propagation in the atmosphere started with the investigation of finite amplitude propagation

in a lossless fluid. Stokes (1848)<sup>8</sup> showed that Poisson's<sup>9</sup> solution implies a steepening of the compression parts of the waveform and an easing of the expansion parts. Using an arbitrary curve he demonstrated that the peaks travel faster than the zeroes of the wave and the troughs travel slower. As time increases the compression portions become steeper. Eventually a discontinuity is formed, at which time the equations of motion are no longer valid. Using conservation of mass and momentum, he found conditions under which the discontinuity can be propagated. Rankine<sup>10</sup> (1870) found that unless heat conduction from particle to particle is included, there is a loss of energy in the propagation of a finite longitudinal disturbance that is not accounted for. By including heat conduction in his analysis he found a form of a finite longitudinal wave that propagates without changing its shape. Rayleigh (1910)<sup>11</sup> found that, although heat conduction is a good dissipation mechanism for condensation shocks, rarefaction shocks are impossible. The reason is that heat transfer by means of conduction requires that heat pass from a hotter body to a colder body, and in the case of a rarefaction shock, heat would pass from a colder body to a hotter body. Rayleigh applied Rankine's method for the more general case, where viscosity is included. Taylor (1910)<sup>12</sup> used different arguments to come to the same conclusion as Rayleigh, namely, that only compression shocks are possible. He obtained an approximate solution of the nonlinear equations of motion for a viscous, heat conducting gas. His solution is valid for weak shocks. From this solution arises the term Taylor shock thickness. The model equation for waves that can contain shocks in a thermoviscous gas

$$c_0^2 u_x - \beta u u_{t'} = \frac{\delta}{2c_0} u_{t'} t' \quad , \quad (1.1)$$

where  $t' = t - x/c_0$ , and

$$\delta = \nu \left\{ \frac{4}{3} + \frac{\mu_v}{\mu} + \frac{\gamma - 1}{Pr} \right\} \quad . \quad (1.1a)$$

The small signal sound speed is  $c_0$ ,  $\beta = (\gamma + 1)/2$ , and  $\gamma$  is the ratio of specific heats. The absorption mechanisms are included in  $\delta$ . Viscous absorption is represented by  $4\nu/3$ , where  $\nu = \mu/\rho_0$ .  $\nu$  is kinematic viscosity,  $\mu$  is the shear coefficient of viscosity, and  $\rho_0$  is the ambient density. Absorption due to heat conduction is represented by  $\nu(\gamma - 1)/Pr$ , where  $Pr$  is the Prandtl number. Rotational relaxation is included in the term  $\nu(\mu_v/\mu)$ , where  $\mu_v$  is the bulk viscosity.

Burgers (1948)<sup>13</sup> proposed an equation of the general form of Eq. (1.1). Hopf (1950)<sup>14</sup> and Cole (1951)<sup>15</sup> found the general solution of Burgers' equation. Lighthill (1956)<sup>16</sup> showed that Burgers' equation is a good approximation for the exact wave equation for a thermoviscous medium.

Polyakova, Soluyan, and Khokhlov (1962)<sup>17</sup> were the first to derive an equation for finite amplitude propagation in a relaxing medium. The equation is similar in form to Burgers' equation,

$$\tau \left[ u_x - \frac{\beta}{c_0^2} u u_{t'} \right]_{t'} + \left[ u_x - \frac{\beta}{c_0^2} u u_{t'} \right] = \frac{m\tau}{2c_0} u_{t'} t' \quad , \quad (1.2)$$

where  $\tau$  is the relaxation time and  $m$  is the dispersion. A sound wave passing through a relaxing fluid may cause a change in the thermodynamic

equilibrium of the fluid. The fluid requires a finite amount of time ( $\tau$ ) to reestablish equilibrium. If the frequency of the sound wave is very high the fluid cannot maintain perfect thermodynamic equilibrium. In this case the vibrational energy becomes effectively "frozen"; the fluid behaves as if there were no vibrational modes. The ratio of specific heat  $\gamma$  reverts to its classical value,  $\gamma_f = 7/5$ . The sound speed has the frozen value  $c_f$  because of its direct relation to  $\gamma_f$ . If, however, the frequency is very low, the changes take place so slowly that the vibrational mode is always in equilibrium and the ratio of specific heats is the equilibrium value

$$\gamma_e = \frac{7/2 + c}{5/2 + c} < \gamma_f \quad ,$$

where  $c$  is the vibrational specific heat ( $c_{vib}/R$ ). The equilibrium sound speed ( $c_0$ ) is directly related to  $\gamma_e$ . The parameter  $m$  in Eq. (1.2) is a measure of the dispersion of the medium,

$$m = \frac{c_f^2 - c_0^2}{c_0^2} \quad .$$

Because there are now two values for  $\gamma$ , there should be two values for  $\beta$ , i.e.,

$$\beta_e = \frac{\gamma_e + 1}{2} \quad , \quad \beta_f = \frac{\gamma_f + 1}{2} \quad .$$

Because  $\gamma_e$  and  $\gamma_f$  are almost the same, and  $\beta$  is the coefficient of a small term (the nonlinear term), Polyakova et al. make no distinction between the two  $\beta$ 's. Presumably, they use  $\beta_f$ .

Polyakova et al.<sup>17</sup> solved Eq. (1.2) for a steady step shock. They found that the solution is continuous for only a small range of amplitudes. The restriction on amplitude had been found earlier by Lighthill (1956).<sup>16</sup> The shock velocity is

$$v = c_0 + \frac{\beta}{2} u_{\text{jump}} ,$$

where we have assumed that the shock is traveling into a quiet fluid and  $u_{\text{jump}}$  is the magnitude of the discontinuity (or jump) in particle velocity. Now, as long as

$$c_0 < v < c_f ,$$

the shock is continuous. A shock which meets that restriction is called "fully dispersed". If the shock velocity is greater than the frozen sound speed it is called "partly dispersed". Polyakova et al. also discussed the problem of a steady step shock in a viscous, relaxing fluid. No analytical solution for the profile was found. Ockenden and Spence (1969)<sup>18</sup> used a slightly more exact set of equations for finite amplitude propagation in a relaxing fluid. They made a distinction between  $\beta_f$  and  $\beta_e$ . The equation of motion simplifies to Eq. (1.2) when  $\gamma_e = \gamma_f$ . Ockenden and Spence also studied the steady step shock in a viscous, heat conducting, and relaxing fluid, but found no solution for the shock profile. Hodgson and Johanneson (1971, 1979)<sup>19,20</sup> and Lighthill (1956)<sup>16</sup> assumed that the shock waves had taken shape and used a combination of the Rankine-Hugoniot shock relations, the equation of state, and the relaxation equation. They presented an exact solution for the structure of the step shock with no further assumptions than that the vibrational specific heat and the relaxation frequency are constant. The actual

profile was found using a numerical method. Morfey (1979)<sup>21</sup> summarized Hodgson and Johanneson's predictions for rise time and maximum allowable amplitude.

All of the aforementioned work on relaxation was on finite amplitude propagation in a mono-relaxing gas. Clark and Rogers (1964)<sup>22</sup> took up the problem of several relaxing modes. They found that if the relaxation time of one mode is much longer than that of the others, one may assume that all the modes that have short relaxation times are in equilibrium. In the case of real air, the relaxation time of oxygen is much longer than that of the other modes except for relative humidities less than 10%. Since relative humidities as low as 10% are rarely found in the real atmosphere, we assume that we are dealing with a single relaxing mode.

All of the solutions mentioned above are found using the boundary conditions for a step shock. Very little has been written about the solution for the N wave. It has generally been assumed that the step shock is a good approximation for the sonic boom waveform. Crighton and Scott (1978)<sup>23</sup> solved both Burgers' equation and the equivalent equation for a relaxing gas for an N wave. However, the solutions are not in a form from which we can find a rise time prediction. Honma, Glass, and Tsumita (1981, 1982)<sup>24,25</sup> have solved the Navier-Stokes equations numerically including vibrational relaxation of oxygen and nitrogen for explosions of a pressurized air sphere. They compared the computed waveforms with Holst-Jensen's<sup>26</sup> experimental data and found good agreement.

## 2. Experimental Literature

There have been very few laboratory measurements of N wave rise time in air. We could find only two such studies, one by Wright<sup>27</sup> and the other by Holst-Jensen.<sup>26</sup>

Wright used an experimental setup similar to ours; that is, he used sparks created by discharging a capacitor across two electrodes. The range of propagation distances used was 10-200 cm. Wright reported data runs at two different spark energies. The N wave amplitude at a distance of 20 cm was 3.62 mbar in the first and 7.86 mbar in the second run. The associated half durations at an amplitude of 0.65 mbar and an unspecified distance were 8.2  $\mu$ sec and 17.0  $\mu$ sec. The range of rise times he obtained was 0.5-2.2  $\mu$ sec. Wright compared his measured rise times with those predicted using the thermoviscous model and obtained fair agreement. He found, however, that as the amplitude of the N wave decreased, the measured rise time fell short of the theoretical prediction. The departure of the measured rise time from the predicted rise time began at a larger amplitude in the waveforms with shorter half durations.

Holst-Jensen used both sparks and exploding wires to create N waves. He was able to obtain N waves of very long half duration. His experiment was conducted in a very large room, and because the amplitude of the N waves decreases very rapidly due to spherical spreading, he was able to obtain waveforms with small amplitudes and long half durations. He created an N wave with a large amplitude and a long half duration but captured his first waveform for analysis at 4.08 m. This process allowed the amplitude to decrease significantly while the half durations increased slightly (due to nonlinear convection). The range

of measurement distance was 4.08-21.60 m. The measured amplitudes were small ( $<0.80$  mbar). The N waves Holst-Jensen recorded were more like sonic boom waveforms than those recorded by Wright because of their longer half durations and smaller amplitudes. The experimental rise times he obtained were in better agreement with those predicted by the relaxation model than Wright's. However, like Wright, he found that the rise time depends on the half duration in addition to the amplitude.

C. Outline of the Study

Chapter 2 contains a description of the analytical models used to predict rise time. The computer propagation algorithm is discussed in Chapter 3. In Chapter 4 we describe the equipment and procedures and in Chapter 5 present the results. Chapter 6 contains our conclusions and recommendation for further work. Appendix A contains derivation of the equation of state for a relaxing fluid. Listings of the driver program and subroutines used in the computer propagation algorithm are found in Appendix B.

CHAPTER 2  
ANALYTICAL PREDICTIONS

A. Introduction

In this chapter we summarize the analytical models that have been used to predict shock rise time. Basically, we use two different models. In the thermoviscous model, the absorption processes that affect the shock rise time are determined by the molecular transport processes (viscosity, heat conduction, and species diffusion) and the rotational relaxation of nitrogen and oxygen molecules. In the second model, called the relaxation model, the absorption is determined by the vibrational relaxation of nitrogen and oxygen molecules.

The general theoretical approach found in the literature, for both cases, is to solve the conservation equations for a step shock (a shock connecting two steady flow fields) in a medium having the appropriate dissipative mechanism. The solution thus gives the profile of a steady shock wave. Since the profile is known, a prediction for the rise time can be found. This approach can be expected to work only for shocks that are almost steady. It is questionable whether the shocks in our experimental N waves, which have very short half duration, are steady enough to approximate step shock. An alternative approach based on a computer algorithm that may be used for waves of arbitrary shape is described in Chapter 3.

### B. Thermoviscous Model

As noted in Chapter 1, Burgers' equation is a reasonable approximation of the exact equations of motion for progressive waves in thermoviscous fluids. The form of Burgers' equation that is useful for experiments in which the time waveform of the sound wave is measured is

$$c_0^2 u_{xx} - \beta u u_{tt} = \frac{\delta}{2c_0} u_{ttt} \quad , \quad (2.1)$$

where

$$\delta = v \left\{ \frac{4}{3} + \frac{\mu_v}{\mu} + \frac{\gamma - 1}{Pr} \right\} \quad . \quad (2.2)$$

Viscosity, heat conduction, species diffusion, and rotational relaxation are included in the "diffusion coefficient"  $\delta$ . Several authors invoke Stokes's assumption, i.e.,  $\mu_v/\mu=0$ . In making this assumption one ignores the rotational relaxation effects. Stokes's assumption does hold for the monatomic gases, but not for air. If we make use of the experimental data of Greenspan (1959),<sup>26</sup> we find that for dry air  $\mu_v/\mu=0.6$ .

Now let us solve Burgers' equation for a steady shock. There are constant conditions (no gradients) far ahead of and far behind such a shock. Since the shock is steady, it travels with a constant velocity  $c_0$ . The shock velocity is given as<sup>16</sup>

$$v = c_0 + \beta \frac{u_a + u_b}{2} \quad ,$$

where  $u_a$  is the particle velocity ahead of the shock and  $u_b$  is the particle velocity behind the shock. Choosing  $v=c_0$  requires that  $u_b=-u_a$ . If all the parts of the wave travel with the velocity  $c_0$ , then  $u=u(t')$

only. Therefore  $u_x=0$ . Our boundary conditions are

$$u \rightarrow -u_1 \quad \text{as} \quad t' \rightarrow -\infty \quad , \quad (2.3a)$$

$$u \rightarrow +u_1 \quad \text{as} \quad t' \rightarrow +\infty \quad , \quad (2.3b)$$

$$u_{t'} = 0 \quad \text{at} \quad t' = \pm\infty \quad . \quad (2.3c)$$

Moreover, we choose an origin such that

$$u = 0 \quad \text{at} \quad t' = 0 \quad . \quad (2.3d)$$

Since  $u_x=0$ , Eq. (2.1) becomes

$$-\beta u u_{t'} = \frac{\delta}{2c_0} u_{t't'} \quad ,$$

which may be integrated once to obtain

$$\frac{\beta u^2}{2} + \frac{\delta}{2c_0} u_{t'} = C_1$$

The constant  $C_1$  may be determined by applying the boundary conditions of Eqs. (2.3). The equation becomes

$$\frac{\delta}{\beta c_0} \frac{du}{dt'} = u_1^2 - u^2 \quad . \quad (2.4)$$

This equation may be solved by separation of variables. If Eq. (2.3d) is substituted the result is

$$u = u_1 \tanh\left(\frac{\beta c_0 u_1}{\delta} t'\right) \quad . \quad (2.5)$$

Equation (2.5) describes the profile of the shock. (A good approximation of this profile is given by the sketch labeled D=100 in Fig. 2.1.)

There are several definitions for the rise time in popular use (see discussion in Chapter 4). By principle, the definition we use is

$$t_r = \Delta u / \left( \frac{du}{dt'} \right)_{\max} \quad , \quad (2.6a)$$

where  $\Delta u$  is the jump in the magnitude of the particle velocity and  $\left( \frac{du}{dt'} \right)_{\max}$  is the maximum slope of the head shock. In this case  $\Delta u = 2u_1$ . Note that a closely related definition for rise time is

$$t_r = \Delta u / \left( \frac{du}{dt'} \right)_{\text{midpoint}} \quad , \quad (2.6b)$$

where  $\left( \frac{du}{dt'} \right)_{\text{midpoint}}$  is the slope of a tangent to the head shock at its midpoint, i.e., at  $p=0.5P$ . For the thermoviscous model, Eqs. (2.6a) and (2.6b) are the same. For the relaxation model, however, the two equations are different.

To find the rise time of the shock in a thermoviscous medium, we first note that the hyperbolic tangent function has its maximum slope at the midpoint ( $t'=0$  in Eq. (2.5)), where  $u=0$ . Equation (2.4) therefore yields

$$\left( \frac{du}{dt'} \right)_{\max} = \left( \frac{du}{dt'} \right)_{\text{midpoint}} = \frac{\beta c_0 (\Delta u)^2}{4\delta} \quad . \quad (2.7a)$$

Accordingly, application of either Eq. (2.6a) or Eq. (2.6b) leads to

$$t_r = \frac{4\delta}{\beta c_0 \Delta u} \quad .$$

If we want to find  $t_r$  in terms of the magnitude of the jump in pressure, we can rewrite  $\Delta u$  using the impedance relation and find that

$$t_r = \frac{4\rho_0\delta}{\beta\Delta p} \quad (2.7b)$$

In general, we find that the rise time is inversely proportional to  $\Delta p$ . In addition, the rise time is directly proportional to the diffusion coefficient  $\delta$  which is directly proportional to the kinematic viscosity  $\nu$ .

Substituting the known qualities for air at a specific temperature, we can find an expression for rise time in terms of inverse peak pressure. For air at 25°C,<sup>27</sup>

$$\nu = 1.559 \times 10^{-5} \text{ m}^2/\text{sec},$$

$$\rho_0 = 1.18 \text{ kg/m}^3,$$

$$\beta = 1.2,$$

$$\gamma = 1.4, \text{ and}$$

$$1/Pr = 1.41.$$

We employ two predictions based on the thermoviscous model. In the first case, TV1, Stokes's assumption is used ( $\mu_v/\mu=0$ ). In the second case, TV2, Greenspan's data is used ( $\mu_v/\mu=0.6$ ). The respective rise time predictions are as follows:

$$\text{Case TV1: } \delta = 2.958 \times 10^{-5} \quad t_r = 1.16/\Delta p$$

$$\text{Case TV2: } \delta = 3.893 \times 10^{-5} \quad t_r = 1.53/\Delta p,$$

where  $\Delta p$  is given in mbar and  $t_r$  is in  $\mu\text{sec}$ . In other words, if  $\Delta p = 1.0$  mbar,  $t_r = 1.16 \mu\text{sec}$  for case TV1 and  $t_r = 1.53 \mu\text{sec}$  for case TV2. (A plot of  $\Delta p \cdot t_r$  for Case TV2 is given in Fig. 2.2.) The rise

time predictions found in this section are compared with our experimental results in Chapter 5.

### C. Relaxation Model

Our analysis for a relaxing medium basically follows that of Polyakova, Soluyan, and Khokhlov<sup>17</sup> and Rudenko and Soluyan.<sup>28</sup> They combine the continuity equation and the momentum equation with the following equation of state (see Appendix A for the derivation).

$$\left(1 + \tau \frac{d}{dt}\right)p = \left(1 + \tau \frac{d}{dt}\right) \left[ c_0^2 \rho' + \frac{1}{2} \left( \frac{\partial^2 p}{\partial \rho^2} \right)_{\epsilon_0} \rho'^2 \right] + m \tau c_0^2 \frac{d\rho'}{dt} \quad (2.8)$$

where  $m = (c_f^2 - c_0^2) / c_0^2$  is the dispersion. After making the appropriate approximations, they obtain Eq. (1.2), which is repeated here for convenience,

$$\tau \left[ u_x - \frac{\beta}{c_0^2} uu_{t'} \right]_{t'} + \left[ u_x - \frac{\beta}{c_0^2} uu_{t'} \right] = \frac{m\tau}{2c_0} u_{t't'} \quad .$$

A steady shock solution of Eq. (1.2) is easily obtained. The boundary conditions are given by Eq. (2.3a, b, c) and the origin is set by Eq. (2.3d). Again, by choosing the shock velocity to be  $c_0$ , we restrict  $u$  to be a function of  $t'$  only. As a result the  $u_x$  terms drop out and we obtain

$$\frac{\beta\tau}{c_0} (uu_{t'})_{t'} + \frac{\beta}{c_0} (uu_{t'}) + \frac{m\tau}{2} u_{t't'} = 0 \quad .$$

Rearranging and integrating once, we find that

$$uu_{t'} + \frac{u^2}{2\tau} + \frac{mc_0}{2\beta} u_{t'} = C_1 \quad . \quad (2.9)$$

Substituting the boundary conditions into Eq. (2.9), we find that  $C_1 = u_1^2/2\tau$ . Equation (2.9) can now be written as

$$\left(u + \frac{mc_0}{2\beta}\right) u_{t'} = \frac{u_1^2 - u^2}{2\tau} ,$$

or

$$\frac{2\left(u + \frac{mc_0}{2\beta}\right)}{u_1^2 - u^2} du = \frac{dt'}{\tau} . \quad (2.10)$$

Expanding the left-hand side and integrating once we obtain

$$-\ln(u_1^2 - u^2) + \frac{c_0 m}{2\beta u_1} \ln\left(\frac{u_1 + u}{u_1 - u}\right) = \frac{t'}{\tau} + C_2 .$$

If we invoke Eq. (2.3d),  $C_2 = -\ln(u_1^2)$ . Substituting this result gives us

$$\frac{t'}{\tau} = \ln\left(\frac{u_1^2}{u_1^2 - u^2}\right) + \frac{mc_0}{\beta \Delta u} \ln\left(\frac{u_1 + u}{u_1 - u}\right)$$

or

$$\frac{t'}{\tau} = \ln\left(\frac{u_1^2}{u_1^2 - u^2}\right) + D \ln\left(\frac{u_1 + u}{u_1 - u}\right) , \quad (2.11)$$

where

$$D = \frac{mc_0}{\beta \Delta u} . \quad (2.11a)$$

Equation (2.11) may be written as

$$\frac{t'}{\tau} = \ln \left[ \frac{(1 + u/u_1)^{D-1}}{(1 - u/u_1)^{D+1}} \right] \quad (2.12)$$

Equation (2.12) describes the profile of the shock. The profile has a different shape depending on the value of the parameter  $D$ , which is a ratio of the parameters representing dispersion and non-linearity. In Fig. 2.1 the shock profile is shown for various values of  $D$ . In computing these profiles, we did not locate the zero of the wave at  $t'=0$ . Another starting point was chosen. As a result, the  $t'$  origin varies from plot to plot. If  $D \gg 1$ , the nonlinear effects are weak and the profile becomes a hyperbolic tangent function (i.e., the shock profile is perfectly skew symmetric). The profile is the same as that of a shock in a thermoviscous medium (see Eq. (2.5)). As  $D$  decreases but is still greater than 1, the shape of the profile begins to lose its perfect skew symmetric shape. The shock profiles for  $D \gg 1$  and  $D > 1$  are called fully dispersed. At  $D=1$ , there is a cusp at  $u=-u_1$ . For  $D < 1$  the profile becomes multivalued. Since a multivalued waveform is physically impossible, we expect that the profile becomes discontinuous. In this case the shock becomes frozen and is called partly dispersed. We can use Eq. (2.12) to predict the rise time for fully dispersed shocks only. If thermoviscous effects are included, the discontinuous section in a partly dispersed shock becomes continuous. However, we have not attempted a solution for both effects.

The expression for  $D$  is found in Eq. (2.11a). If we invoke the impedance relation, we can find  $D$  in terms of the pressure jump  $\Delta p$ ,

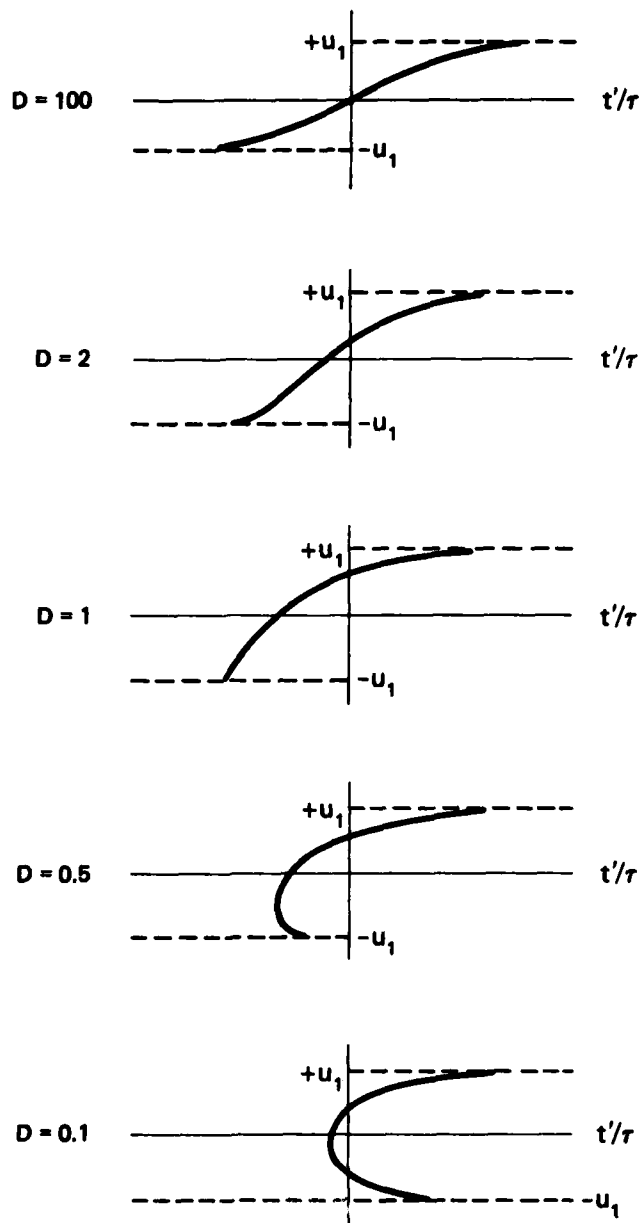


FIGURE 2.1  
STEP SHOCK PROFILE IN A RELAXING MEDIUM

$$D = \frac{\rho_o c_o^2}{\beta \Delta p} .$$

We can determine the maximum allowable peak pressure for which we can predict the rise time by setting  $D=1$  and solving for  $\Delta p$ ,

$$\Delta p_{\max} = \frac{\rho_o c_o^2}{\beta} .$$

Since the dispersion, density, and sound speed change with temperature, we need to choose a particular temperature for the calculation. In our experiment the temperature was fairly constant at 25°C. The value for  $m$  is calculated by using the harmonic oscillator equation<sup>5,6</sup> to calculate the vibrational specific heat of oxygen. From this result we find  $\gamma_e$ . The dispersion is defined as

$$m = \frac{c_f^2 - c_o^2}{c_o^2}$$

or

$$= \frac{\gamma_f - \gamma_e}{\gamma_e} .$$

The value for  $\gamma_f$  is always 1.4. For 25°C

$$\gamma_e = 1.3989$$

$$m = 7.39 \times 10^{-4}$$

$$\rho_o = 1.18 \text{ kg/m}^3$$

$$c_o = 345.94 \text{ m/sec, and}$$

$$\beta = 1.205.$$

At this temperature, the maximum pressure jump is (oxygen relaxation only)

$$\Delta p_{\max} = 0.866 \text{ mbar.}$$

Above this limit the shocks are partly dispersed. We cannot compare any data for pressure jumps above 0.866 mbar with the predictions from this model.

Recall the discussion of the definition of rise time on p. 16. If the rise time based on the slope at the midpoint is calculated, we use

$$\left(\frac{du}{dt'}\right)_{\text{midpoint}} = \left[ \frac{u_1^2 - u^2}{2\tau(u + Du_1)} \right]_{t'=0} = \frac{\Delta u}{4\tau D} \quad , \quad (2.13a)$$

and use of Eq. (2.6b) leads to

$$t_r = 4\tau D = \frac{4\tau mc_0}{\beta \Delta u} \quad . \quad (2.13b)$$

If we want to find  $t_r$  in terms of  $\Delta p$ , the magnitude of the jump in pressure, we can rewrite  $\Delta u$  using the impedance relation and find that

$$t_r = \frac{4\tau m \rho_0 c_0^2}{\beta \Delta p} \quad . \quad (2.14)$$

On the other hand, the rise time calculated by means of Eq. (2.6a) requires the value of the maximum slope, which is found to be

$$\left(\frac{du}{dt'}\right)_{\text{max}} = \frac{\Delta u}{2\tau} \left( D - \sqrt{D^2 - 1} \right) \quad . \quad (2.15a)$$

Substitution of this value in Eq. (2.6a) leads to (after some manipulation)

$$t_r = 2\tau \left( D + \sqrt{D^2 - 1} \right) \quad . \quad (2.15b)$$

Now consider the limiting cases. The limit as  $D \rightarrow \infty$  is

$$t_r = 4\tau D \quad ,$$

in agreement with Eq. (2.13b), as one would expect (see the plot for  $D=100$  in Fig. 2.1). At the other extreme,  $D=1$ , the rise time is

$$t_r = 2\tau \quad .$$

Thus, when  $D=1$ , the value of the rise time based on the maximum slope is half that based on the slope at the midpoint of the shock.

The choice between Eqs. (2.13b) and (2.15b) was eventually made on the basis of experimental data. For the N waves we measured, we found that the maximum slope of the head shock occurred at the shock midpoint. It therefore seemed reasonable to use Eq. (2.13b) as the expression for the relaxation model and Eq. (2.6b) as the definition on which the experimental measurement is based.

In Fig. 2.2 we plot the rise time times  $\Delta p$  versus the relative humidity for several temperatures (based on Eq. (2.14)). For comparison the curve TV2 is included. The rise time is heavily dependent on the humidity and temperature. The dependence is mainly a result of the dependence of the relaxation time on humidity and temperature. For example, at 35% relative humidity, 15°C, the relaxation time  $\tau = 9.38 \mu\text{sec}$ . At 100% humidity, 30°C, the relaxation time  $\tau = 0.931 \mu\text{sec}$ . The dispersion  $m$ , the density, and the equilibrium sound speed have a slight dependence on temperature. In order to compare the predictions from the model with the experimental data we choose the relative humidity and temperature and find  $\Delta p \cdot t_r$ . For example, at 60% relative humidity, 25°C,

$$\Delta p \cdot t_r = 9.638 \quad ,$$

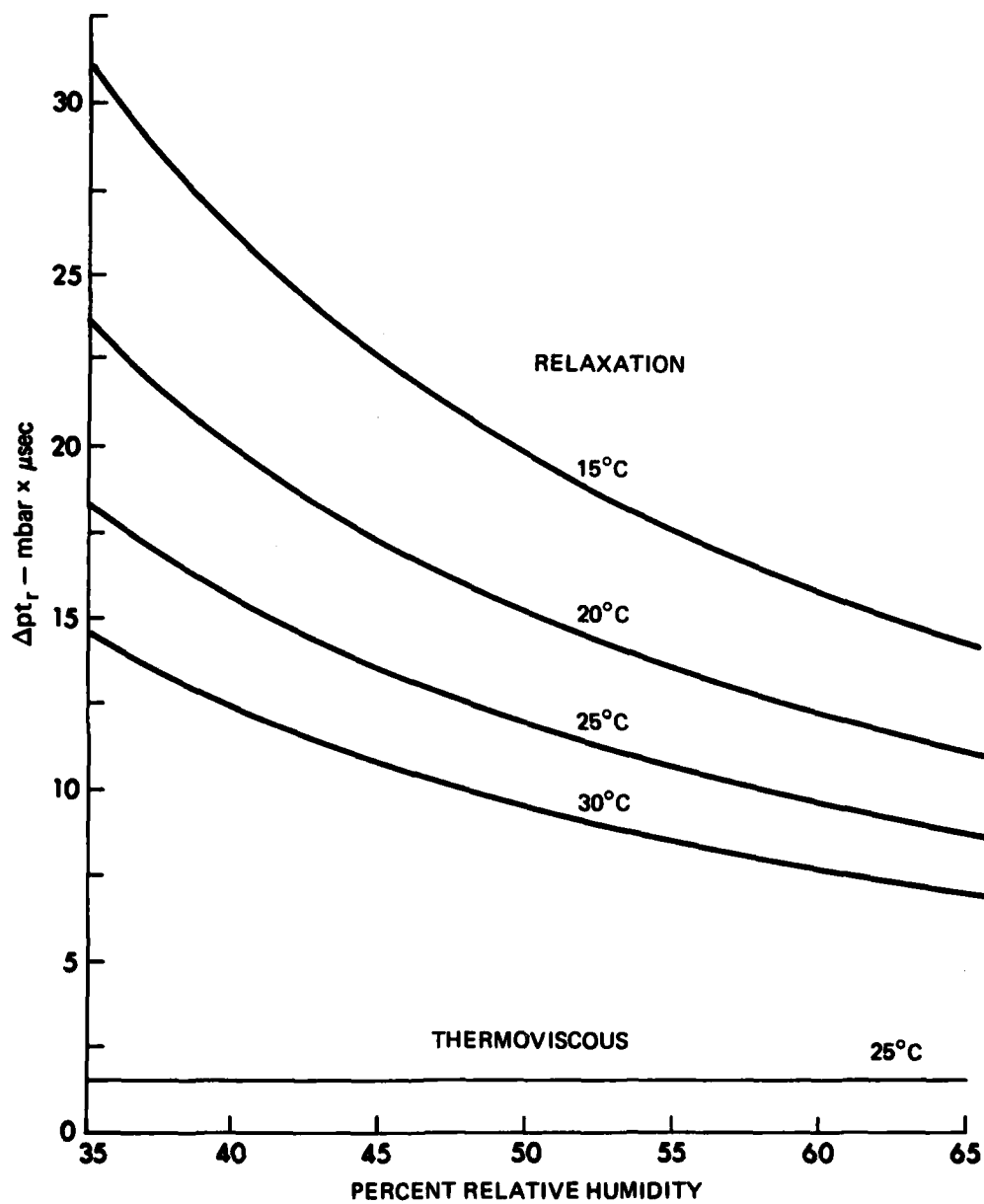


FIGURE 2.2  
RISE TIME PREDICTION

where  $\Delta p$  is in mbar and  $t_r$  is in  $\mu\text{sec}$ . Under these conditions the rise time is  $\approx$ six times longer in a relaxing medium than in a thermoviscous medium. The appropriate representation for  $t_r$  is used for comparison with our experimental data in Chapter 5.

#### D. Discussion

Before comparing our experimental rise times with those calculated using the models described in this chapter, we must decide whether the models fit our experiment. First, the rise time predictions are for plane waves, whereas our experimental data are for spherical waves. We assume that the plane wave formulas are valid if the amplitude of the N wave is changing slowly enough that the shock can adjust rapidly enough to follow the change. This assumption may be poor close to the source, but it is valid at great distances. Second, and more important, the theoretical solutions are for a step shock. This assumption is valid for sonic booms because the sonic boom waveform has an extremely long half duration ( $\sim 0.2$  sec). The slope behind the head shock is very, very gentle. Our N waves, however, have very short half durations ( $\sim 0.02$  msec). The slope behind the head shock is very steep, and may therefore affect the rise time.

To obtain better solutions we would need to derive the rise time predictions directly for an N wave. Since the shock profile is not steady (the amplitude decreases linearly behind the head shock), the simplification  $u_x = 0$  cannot be used. Instead, the full equation (Eqs. (2.1) or (1.2)) must be solved. Both Burgers' equation and Eq. (1.2) have been solved for an N wave.<sup>21</sup> However, in neither case was a rise time prediction made. As an alternative to attempting an analytical solution, we

used a computer propagation algorithm similar to those described by Pestorius,<sup>29</sup> Anderson,<sup>30</sup> Theobald,<sup>31</sup> and Essert.<sup>32</sup> The algorithm is described in the next chapter.

CHAPTER 3  
WAVE PROPAGATION ALGORITHM

A. Introduction

In this chapter we present our alternative to the analytical models, the wave propagation algorithm. The algorithm is based on the assumption that over a small enough propagation distance the effects of nonlinear distortion and absorption are independent and may therefore be computed separately and then added. The algorithm is applicable to arbitrary waveforms, even ones containing discontinuities; therefore it is ideal for dealing with our N waves. It is designed to calculate the shape of the waveform as a function of distance. The computer language used in the algorithm is FORTRAN. The programs were run on a CDC Cyber Series 170 computer.

The theoretical basis of the algorithm is presented in Section B below. The calculations that constitute the "absorption step" and the "nonlinear distortion step" are given. In Section C we examine the algorithm in general. The driver program is discussed, part by part, and the subroutines explained. Two sample computed waveforms are shown in Section D.

B. Theory

1. Absorption

Consider a single frequency component of an arbitrary spherical wave. If the (complex) amplitude of the component is  $\bar{U}_0$  at a distance  $r_0$ , the amplitude  $\bar{U}$  at a distance  $r$  is, in the absence of nonlinear

distortion, given by

$$\bar{U} = \frac{r_0 \bar{U}_0}{r} e^{-\zeta(r-r_0)} .$$

The factor  $e^{-jk(r-r_0)}$  does not appear because the wave is represented in the time domain in terms of the retarded time  $t'=t-(r-r_0)/c_0$ . If  $r=r_0+\Delta r$ , where  $\Delta r$  is the propagation distance step,

$$\bar{U} = \frac{r_0}{r_0 + \Delta r} \bar{U}_0 e^{-\zeta(r-r_0)} , \quad (3.1)$$

where

$$\zeta = \alpha - j\eta , \quad (3.1a)$$

$\alpha$  is the attenuation, and  $\eta$  is the dispersion parameter,

$$\eta = \omega \left( \frac{1}{c_0} - \frac{1}{c_{ph}} \right) . \quad (3.1b)$$

For a thermoviscous medium,  $\alpha = \delta\omega^2/2c_0^3$  and  $\eta=0$ . For a relaxing medium the absorption is

$$\alpha = \frac{m\tau\omega^2}{2c_0(1+\omega^2\tau^2)} ,$$

where  $m=(c_f^2-c^2)/c_0^2$  and the dispersion associated with it is

$$\eta = \omega\tau\alpha .$$

For the real atmosphere,  $\alpha$  is given by the ANSI standard, which is discussed in the section on application of absorption. The dispersion is  $\eta=\omega(\tau\alpha)_{O_2}$ . The application of Eq. (3.1) is called the absorption step. It includes spherical spreading, as well as absorption and dispersion.

## 2. Nonlinear Distortion

The distortion of the waveform is caused by a relative time shift of the wavelets. A wavelet is a point on the waveform. The time shift is due to the dependence of the wavelet propagation speed  $dx/dt$  on the wavelet amplitude  $u$ , in particular

$$\frac{dx}{dt} = c_0 + \beta u \quad , \quad (3.2)$$

where  $\beta = (\gamma + 1)/2$  and  $\gamma$  is the ratio of specific heats. Given a time waveform, at a distance  $r = r_0$ , consider the typical wavelet  $u_i$ , whose time coordinate is  $t_i$ . The value of  $t_i$  at  $r = r_0 + \Delta r$  is

$$\begin{aligned} t_{i_{\text{new}}} &= t_{i_{\text{old}}} + \frac{\Delta r}{dx/dt} \\ &= t_{i_{\text{old}}} + \frac{\Delta r}{c_0 + \beta u_i} \quad , \end{aligned} \quad (3.3)$$

or, if the binomial expansion is used,

$$\begin{aligned} t_{i_{\text{new}}} &= t_{i_{\text{old}}} + \frac{\Delta r}{c_0} \left( 1 - \frac{\beta u_i}{c_0} + \text{higher order terms} \right) \\ &= t_{i_{\text{old}}} + \frac{\Delta r}{c_0} - \frac{\beta u_i \Delta r}{c_0^2} \quad . \end{aligned} \quad (3.4)$$

When we compute the new time waveform, we shift the entire waveform by an amount  $\Delta r/c_0$ . That is, we express  $u$  in terms of the retarded time  $t' = t - (\Delta r/c_0)$ . Equation (3.4) now becomes

$$t'_{i_{\text{new}}} = t'_{i_{\text{old}}} - \frac{\beta u}{c_0^2} \quad . \quad (3.5)$$

Thus, after a distance step  $\Delta r$ , the wavelet appears at time  $t'_{i_{\text{new}}}$  instead of  $t'_{i_{\text{old}}}$ . We call the application of Eq. (3.5) the distortion step. We use a plane wave relation, Eq. (3.2), to calculate the distortion for a

spherical wave. The justification for this is that although the amplitude  $u_j$  is fixed during the  $n$ th distortion step, it drops because of absorption and spherical spreading during the  $N+1$ th absorption step. During the  $n+1$ th distortion step, therefore,  $u_j$  is smaller by the appropriate amount.

### C. Wave Propagation Algorithm

In general, the wave propagation algorithm involves the implementation of Eqs. (3.1) and (3.5) alternately in small steps ( $\Delta r$ ). The initial waveform is input at  $r=r_0$ . The waveform is transformed from the time domain to the frequency domain, via a fast Fourier transform (FFT), and absorption is applied (Eq. (3.1)) over the first step. The waveform is then transformed back to the time domain by an inverse FFT  $[(\text{FFT})^{-1}]$  and nonlinear distortion is applied (Eq. (3.5)) over the first step. The propagation distance  $r$  becomes  $(r_0+\Delta r)$ , and the process is repeated for the next step. The loop continues until  $r$  equals a specified propagation distance.

Several important details have been left out of the discussion above. First, it is important that we take small steps to ensure that no shocks form during a nonlinear distortion step. We apply the absorption step before the distortion step to take care of the possibility that the initial waveform contains a true discontinuity. Open air absorption is sufficient to prevent a multivalued waveform, assuming the step is small. We ensure that the step size is small by calculating the shock formation distance after each absorption-distortion step. We then use this calculation to select the next value of  $\Delta r$ . Pestorius<sup>29</sup> found that a step size of one-tenth the shock formation distance is sufficiently small

to prevent shocks from forming in the subsequent steps. Although Pestorius looked at plane waves, not spherical waves, we assume that his findings are applicable to our problem. We also improve the efficiency of our program in recalculating the step size, by taking advantage of the fact that  $\Delta r$  can be increased as the wave gets weaker. As a result, we can reduce the number of trips back and forth from the time domain to the frequency domain. The second omission is that after the distortion step the time increments between the points in the waveform are no longer equally spaced. The FFT routine we use requires that the time increments be equally spaced. We find equally spaced time increments using the subroutine RESAMP.

The wave propagation algorithm is implemented by a driver program, LB01. A listing of the program is found in Appendix B. A flowchart of the algorithm is shown in Fig. 3.1.

1. Driver Program

- a. Input Scheme

The input to the program is the time waveform of the N wave received at the initial position  $r_0$ . A data file is created by reading the voltage levels from the digital oscilloscope in 0.5  $\mu$ sec time increments. A buffer of zeroes is included on either side of the data to prevent an end point problem similar to that encountered by Pestorius.<sup>29</sup> The number of data points (N) in the waveform is the total duration (including zeroes) divided by the time increment ( $\Delta t$ ).

At the end of the data file we list several constants used in the program. Other constants are input on the terminal. Some of the

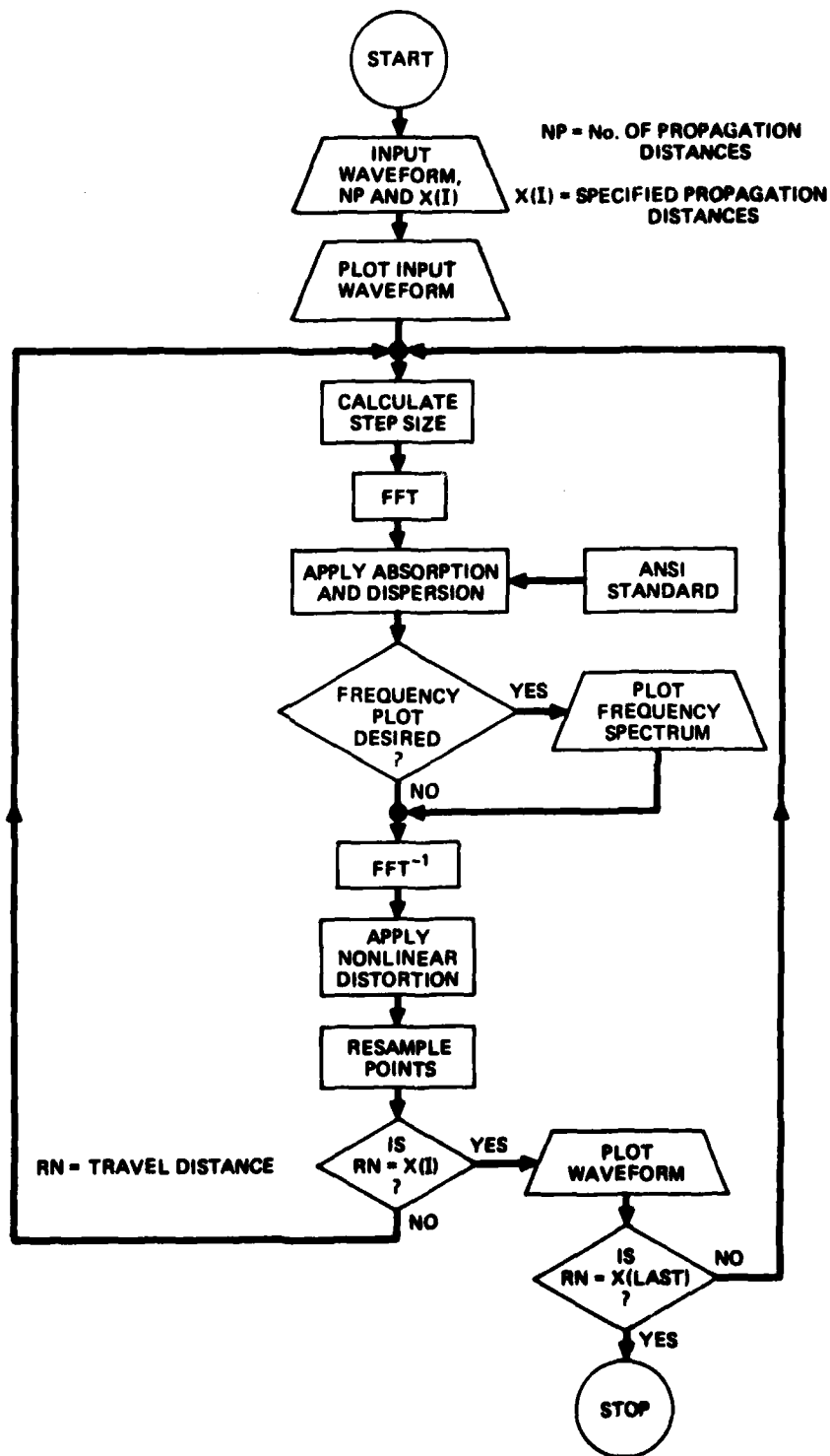


FIGURE 3.1  
 FLOWCHART OF COMPUTER PROPAGATION ALGORITHM

important parameters and constants are as follows.

- P the real one-dimensional amplitude array containing N amplitude coordinates ( $u_i$ ) of the waveform (in mV).
- A the complex amplitude array containing the frequency components of the waveform (used only in the frequency domain).
- T the real one-dimensional time array containing N time coordinates ( $t_i$ ) of the waveform (in seconds).
- X the real one-dimensional array describing the source-receiver distances (including the input distance) at which we want an output.
- NP the number of distances in array X.
- N the number of points in the waveform.
- DELT the time increment between points.
- IOPT the plotting option.
- FCON the conversion factor for converting the P array to a particle velocity array.
- PNORM a normalizing factor used in the plot routine.
- RN the propagation distance.
- SSI the incremental step size ( $\Delta r$ ) used to cover the distances X(I).

b. Step Size Calculation

The step size is calculated for each pass of the absorption and nonlinear distortion. This allows us to reduce the calculation time by taking advantage of the slowing down of the distortion caused by spherical

spreading. The step size is calculated using a relation for the distortion variable.

$$\sigma = \frac{z}{\bar{z}},$$

where  $z = r_0 \ln(r/r_0)$  and  $\bar{z}$  is the value of  $z$  when shock formation occurs ( $\sigma=1$ ). The shock forms at the place in the waveform where the waveform has its maximum slope. We find that

$$\bar{z} = \frac{c_0^2}{\beta(f')_{\max}},$$

where  $f'$  is the slope. Combining the information above we find that

$$\sigma = \frac{r_0}{c_0^2/\beta(f')_{\max}} \ln\left(\frac{r}{r_0}\right), \quad (3.6)$$

and

$$\sigma + \Delta\sigma = \frac{r_0}{c_0^2/\beta(f')_{\max}} \ln\left(\frac{r + \Delta r}{r_0}\right). \quad (3.7)$$

Subtract Eq. (3.6) from (3.7) to obtain

$$\Delta\sigma = \frac{r_0}{c_0^2/\beta(f')_{\max}} \ln\left(1 + \frac{\Delta r}{r}\right).$$

Solving for  $\Delta r$  we find that

$$\Delta r = r_0(e^Q - 1), \quad (3.8)$$

where

$$Q = \frac{\Delta\sigma}{r(c_0^2/\beta f'_{\max})^{-1}}.$$

We can generalize Eq. (3.8) for any step size  $\Delta r_n$  by replacing  $r_0$  with  $r_{n-1}$ , the last propagation distance. On the basis of Pestorius's experience<sup>29</sup> we choose  $\Delta\sigma=0.1$ . We use a subroutine NWSLOPE to calculate the slope of the head shock (the steepest part of the waveform). The head shock of the input waveform usually contains only three or four points. Therefore, we use a scheme in which we find the slope over the central portion of the head shock. We first decide between which two points we want to compute the slope. The points are located at certain fractions of the N wave amplitude (AMAX). The fractions (F1 and F2) are input from the terminal. The time increments (T1 and T2) corresponding to (F1·AMAX) and (F2·AMAX) are found by performing a linear interpolation between the two points bounding (F1·AMAX) and (F2·AMAX), respectively. The slope is then calculated using the following equation:

$$\text{SLOPE} = (F2-F1) \cdot \text{AMAX}/(T2-T1) \quad . \quad (3.9)$$

We can now write Eq. (3.8) in code. The variable AXSTP, in code, corresponds with  $\Delta\sigma c_0^2/\beta$ . Q now becomes

$$Q = \text{AXSTP}/(\text{RN} \cdot \text{SLOPE}) \quad .$$

Finally the step size increment (SSI) is

$$\text{SSI} = \text{RN}(e^Q - 1) \quad . \quad (3.10)$$

### c. Application of Absorption

We transform from the time domain to the frequency domain to apply absorption and dispersion to the waveform. The absorption we consider is actual atmospheric absorption (quiet air). The Applied Research Laboratories computer library subroutine FFTCC was used to transform to the frequency domain. The absorption and dispersion are calculated by the function DABSORP, which is a modified version of the

function ABSORP, also to be found in the user library. It is a digital implementation of ANSI document S1.26-1978, "Standard Method for the Calculation of the Absorption of Sound by the Atmosphere".<sup>7</sup> This function allows one to compute the absorption coefficient for a given frequency, ambient temperature, ambient pressure, and relative humidity. A more detailed discussion of the function is found in the discussion of the subroutines.

The absorption coefficients are calculated in the following manner. The number of frequencies at which we compute absorption coefficients is  $NF=N/2$ , where  $N$  is the number of points in the waveform. There is no absorption coefficient for the dc component. We compute only  $N/2$  coefficients because the highest frequency we can discern is half the sampling frequency ( $f_s=1/DELT$ ). The frequency increment is

$$DELF = \frac{1}{N * DELT} ,$$

where  $DELT$  is the time increment between points. The frequencies at which the absorption coefficients are calculated are found by multiplying  $DELF$  times  $J$ , where  $J$  is a counter from 1 to  $NF$ . The value for the absorption coefficient (in dB/m) at each frequency is then computed by DABSORP. Thermoviscous absorption, rotational relaxation of nitrogen and oxygen, and vibration relaxation of nitrogen and oxygen are included in the absorption coefficient. In addition to the absorption coefficient, the function returns the value of the oxygen relaxation frequency and the absorption coefficient due to oxygen relaxation. We find the quantity  $n$ , which is related to the dispersion (see Eqs. (3.1a) and (3.1b)), from

these values. Since the absorption coefficient is in dB/m we need to modify Eq. (3.1),

$$\bar{U} = \frac{r_0}{r_0 + \Delta r} \bar{U}_0 10^{-\zeta(r-r_0)/20} \quad (3.11)$$

For our case

$$\begin{aligned} \alpha &= \alpha_{TV} + \alpha_{N_2} + \alpha_{O_2} \\ &= \frac{\delta\omega^2}{2c_0^3} + \frac{(m\tau)_{N_2} \omega^2}{(1+\omega^2\tau_{N_2}^2)} + \frac{(m\tau)_{O_2} \omega^2}{(1+\omega^2\tau_{O_2}^2)} \end{aligned}$$

and

$$\eta = \omega(\tau\alpha)_{O_2}$$

In the program the complex variable  $(-\zeta)$  is named ALFA and the spherical spreading factor  $r_0/(r_0 + \Delta r)$  is named SPREAD. Eq. (3.11) is written in code as

$$A(J) = \text{SPREAD}/N * A(J)_{old} 10^{(\text{ALFA} * \text{SSI}/20)}$$

The factor  $1/N$  is needed for normalization because of certain properties of the subroutine FFTCC.

#### d. Application of Nonlinear Distortion

After the absorption step is taken we transform back to the time domain to apply the nonlinear distortion. The distortion is applied using Eq. (3.5). In our program the term  $\beta\Delta r/c_0^2$  is named DISFAC. Equation (3.5) is represented in code as

$$T(J) = [(J-1) * \text{DELT}] - [\text{DISFAC} * P(J)]$$

where  $((J-1)*\text{DELT})=T(J)_{old}$ .

After the distortion step, the time increment between points is no longer the same throughout the waveform. The FFT routine we use requires data sampled at equal time increments. To resample the data points at equal time increments we used a subroutine called RESAMP. This subroutine is discussed in the section describing the subroutines.

e. Data Output

The program returns to the step size calculation after re-sampling the data points. When the propagation distance reaches one of the specified propagation distances, the time waveform is plotted by means of the subroutine NWPLOT. If a frequency spectrum has also been specified, it is plotted at this time using the subroutine FQPLOT. A plot file is created in both plot subroutines. These subroutines are discussed in the next section.

The entire process is repeated until the waveform reaches its final propagation distance. At the end of the program the plot file is sent to a Nicolet Zeta Research plotter, which draws the waveforms.

2. Subroutines

a. DABSORP

The function DABSORP is a modified version of the Applied Research Laboratories computer library function ABSORP. DABSORP is accurate to within  $\pm 10\%$  over the temperature range 255.4°K (0°F) to 310.9°K (100°F) at relative humidities from 0% to 100%, frequencies 100 Hz to 10 MHz, and ambient pressures from 0 to 2 atm. It was necessary to modify ABSORP to include the effect of dispersion due to oxygen relaxation. Our modification utilizes a separate calculation of the absorption coefficient due to oxygen relaxation (OALPH). The

modified function passes the value of OALPH as well as the value for the relaxation frequency of oxygen (FRO) to the driver program. The absorption coefficient used in the absorption step (ALFA) is defined as

$$\begin{aligned} \text{ALFA} &= -\zeta \\ &= -\alpha + j\eta \\ &= \text{ALR} + j(\text{ALI}) \end{aligned}$$

where

$$\text{ALR} = -\alpha = -\text{DASORP}, \text{ and}$$

$$\text{ALI} = \eta = \omega\tau\alpha = \frac{f}{f_0} \alpha$$

$$= F * \text{OALPH}/\text{FRO} \quad .$$

F is the frequency at which we calculate the absorption coefficient. A listing of DABSORP is found in Appendix B.

b. RESAMP

The nonlinear distortion step shifts the time values of the data points by an amount proportional to their particle velocity. The subroutine RESAMP uses a point-slope formula to interpolate between the unequally spaced time values, to find values at equal time intervals, so that the FFT routine can be used. The subroutine call is

CALL RESAMP (P,T,WK,NR,N,DELT,IERR).

WK is a scratch array of dimension NR. IERR is an error flag which returns 1 if a sampling error is encountered and 0 on no error. A listing of RESAMP is found in Appendix B.

c. NWPLOT

This subroutine is used to plot time waveforms at the desired propagation distances. For each run, the amplitude of each waveform is

normalized to the amplitude of the input waveform. If the ratio  $P/P_{NORM}$  is small, it is multiplied by an appropriate scale factor. As a result, all of the waveforms (even those at large propagation distances) are large enough for us to analyze accurately. The subroutine call is

```
CALL NWPLOT (P,T,N,PNORM,IRESULT,TMIC,RN) .
```

$P_{NORM}$  is the amplitude of the input waveform.  $IRESULT$  is the result file which returns a listing of the P and T arrays at each specified propagation distance.  $TMIC$  is the number of  $\mu\text{sec/in.}$  specified for X axis.  $RN$  is the propagation distance. A listing of  $NWPLOT$  is found in Appendix B.

d. FQPLOT

$FQPLOT$  plots the frequency spectrum of the N wave. The spectrum is plotted on a log-log scale normalized to the peak particle velocity so that at the fundamental frequency the amplitude is 0 dB. Use of this subroutine is optional. Selection is made in the driver program by picking  $IOPT$  equal to 0 (frequency plot only) or 2 (frequency plot and time waveform). The subroutine call is

```
CALL FQPLOT (A,DELT,N,IFIRST) .
```

$IFIRST$  is a flag that signals the first propagation step. A listing of  $FQPLOT$  can be found in Appendix B.

3. Frequency Domain Analysis

In an effort to determine the effect of dispersion of the N wave, we performed many computer propagations, both with and without dispersion. We found very little difference between the time waveforms that were computed with dispersion and those that were computed without dispersion. The effect of dispersion on a finite amplitude sine wave

has been studied by Blackstock.<sup>33</sup> In order to check whether the dispersion was working correctly in our program, we input a sine wave and computed the amplitude of the fundamental, second harmonic, and third harmonic. Our results did not agree with those predicted by Blackstock. We discovered that the FFT routine was the cause of our discrepancy. As noted in the section describing the application of absorption, the number of filters or frequency components depends on the number of points in the waveform. These filters have a  $(\sin x)/x$  weighting function associated with them. Therefore, the amplitudes returned by the program are not for discrete frequencies but for a frequency "band". To get a more accurate measurement of the amplitudes we employed an aperture shading subroutine called APWT in which Taylor<sup>34</sup> weighting was used. The peak-to-sidelobe ratio was 30 dB. After the routine was incorporated in the program, we found that the computed amplitudes agreed well with the analytical predictions. As a further check we ran the program with and without the weighting to determine whether the time waveforms were affected as much as the frequency spectrum. We found the difference between the runs was negligible, and concluded that whatever was done in the FFT was undone by the  $(FFT)^{-1}$ . It was concluded that the aperture shading was needed only if one desires a frequency analysis of the waveform. Since only time waveforms were analyzed, we decided to delete the aperture weighting subroutine. However, a listing of APWT and TAYLOR is found in Appendix B, and should be included if a frequency analysis is done.

#### D. Results

We obtained very good agreement between our experimental waveforms and the computed generated waveforms. The results are discussed in more detail in Chapter 5. Two sample output waveforms are shown in Fig. 3.2. The amplitudes of the waveforms are found in the result file generated by the driver program. The value  $m_1$  is the maximum slope of head shock. The maximum slope for our measured waveforms is consistently the slope of the tangent to the head shock at  $p = 0.5 P$ . Therefore, we adopt this method for measuring our waveforms. The rise time is simply the amplitude  $P$  divided by  $m_1$ . The half duration  $T$  is the time between the foot shock and the zero crossing of the expansion phase. We have defined the shock foot to occur at the intersection of the tangent line with the time axis. This definition is consistent with our experimental observations.

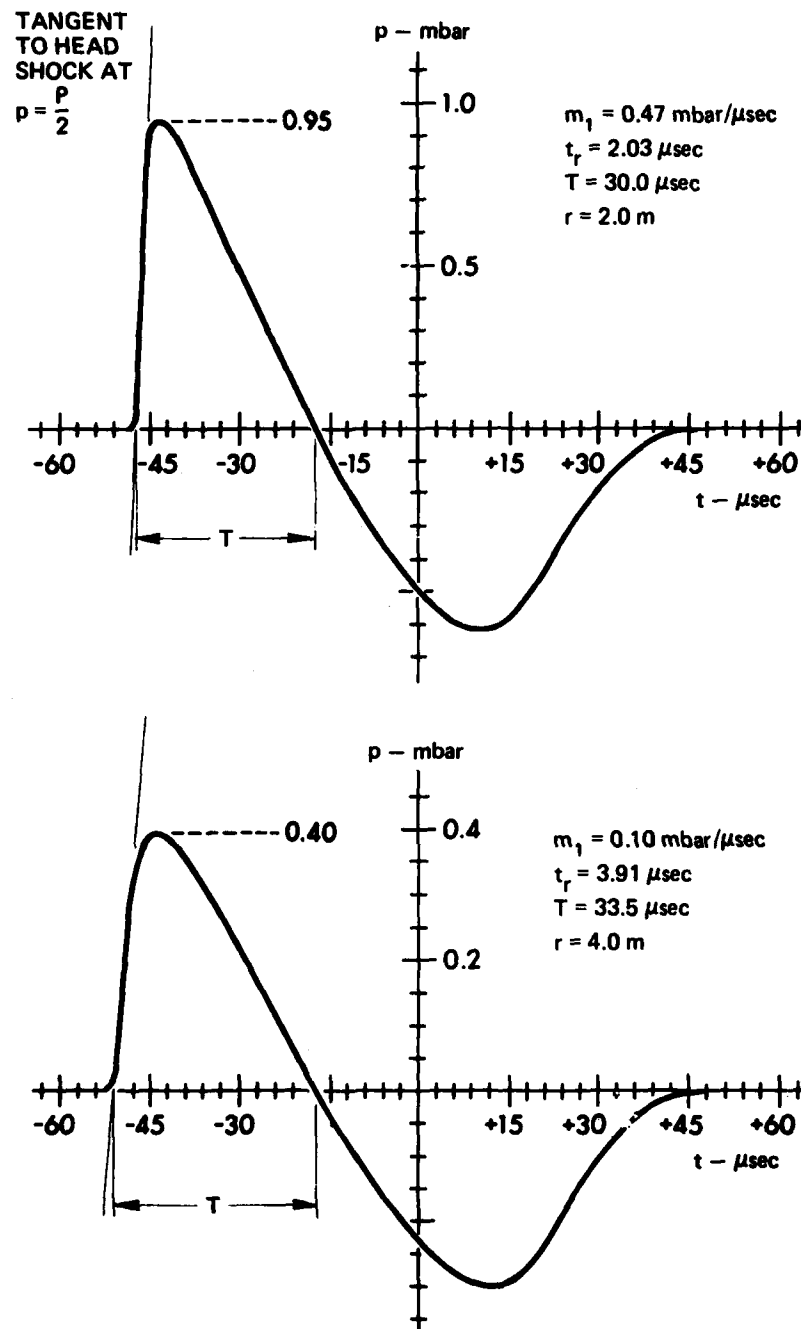


FIGURE 3.2  
 SAMPLE COMPUTED WAVEFORMS  
 AND IMPORTANT PARAMETERS  
 SPARK ENERGY = 9.88 J

## CHAPTER 4

### EXPERIMENT

This chapter contains a detailed description of the measurement apparatus and method. A few sample measurements are shown.

#### A. Apparatus

The measurements system has four main parts: spark source, optical bench, receiving system, and data capture and storage. The arrangement of the system is shown in Fig. 4.1. The important features of each are described in the following paragraphs.

##### 1. Spark Source

A Grozier Technical Systems Incorporated Model 51-4 spark generator was used to provide energy for the spark by charging a 1.0  $\mu\text{F}$  capacitor to 0-4 kV. The capacitance was allowed to discharge across a gap between two diametrically opposed tungsten electrodes. Typical gap lengths were between 1 and 5 mm.

A third electrode, located perpendicular to the gap, was used to trigger the discharge at a set voltage. The advantages of this system are flexibility and reproducibility. Without the trigger electrode we are restricted to one voltage, the natural breakdown potential, for each gap length. Moreover, the natural breakdown potential varies from spark to spark. With the trigger in use, when the voltage across the capacitor reaches the voltage preset by the operator, a small spark jumps from the 3rd electrode and stimulates breakdown. The operator is therefore able to control the spark energy, which largely determines amplitude and half

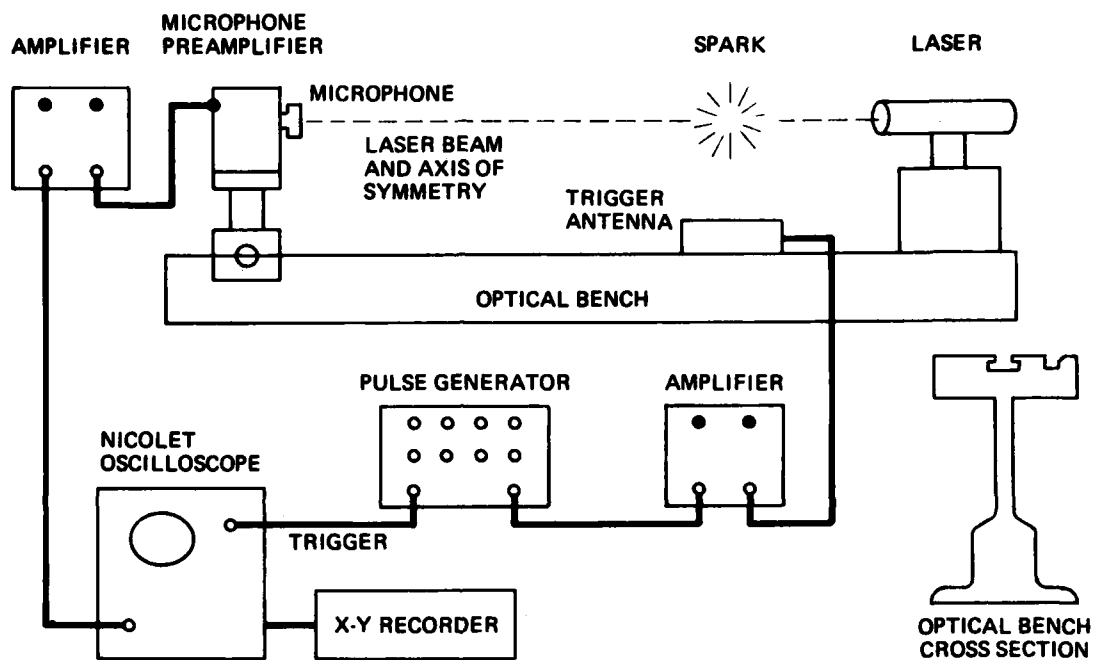


FIGURE 4.1  
EXPERIMENTAL ARRANGEMENT

duration of the N wave. The breakdown voltage was monitored by a Simpson Model 260 voltmeter.

The electrode configuration is shown in Fig. 4.2. Each electrode was 1/16 in. in diameter and its point was ground to a cone of half-angle approximately 30°. A polypropylene block was machined to support the electrodes. The electrodes were held in threaded aluminum dowels. The spark gap could be adjusted symmetrically by turning the dowels. A photograph of an actual spark discharge is found in Fig. 4.3; neutral density filters were used to cut down on the light generated by the spark. It is clear that the breakdown does not really take place along a specific path but in a general region around the electrodes.

## 2. Optical Bench

The I-beam rails used in this experiment were designed by Anderson<sup>30</sup> and are described in his thesis. They were made in the machine shop at Applied Research Laboratories. Two rails were used as an optical bench; the first one 12 ft long and the second one 8 ft long. The rails were clamped on a heavy table and leveled to within 0.0005 in./ft. A Hughes Model 3193H laser was used to align the tracks of the two rails.

## 3. Receiving System

The condenser microphone used was based on designs and construction techniques developed over the years by previous students at Applied Research Laboratories. The first microphones were built by Cornet,<sup>35</sup> who modified designs by Wright.<sup>27</sup> Anderson<sup>30</sup> improved the construction process and was able to obtain a high degree of consistency from one microphone to the next. Basically, a condenser microphone consists of a metallic diaphragm, which is exposed to the sound field, a

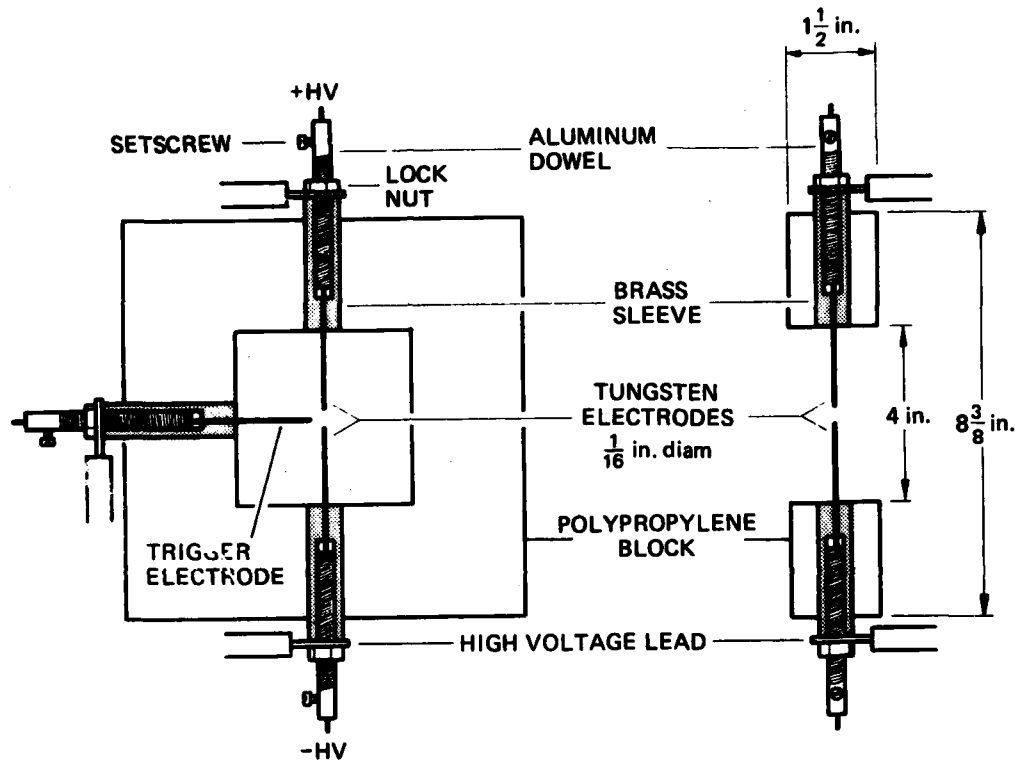
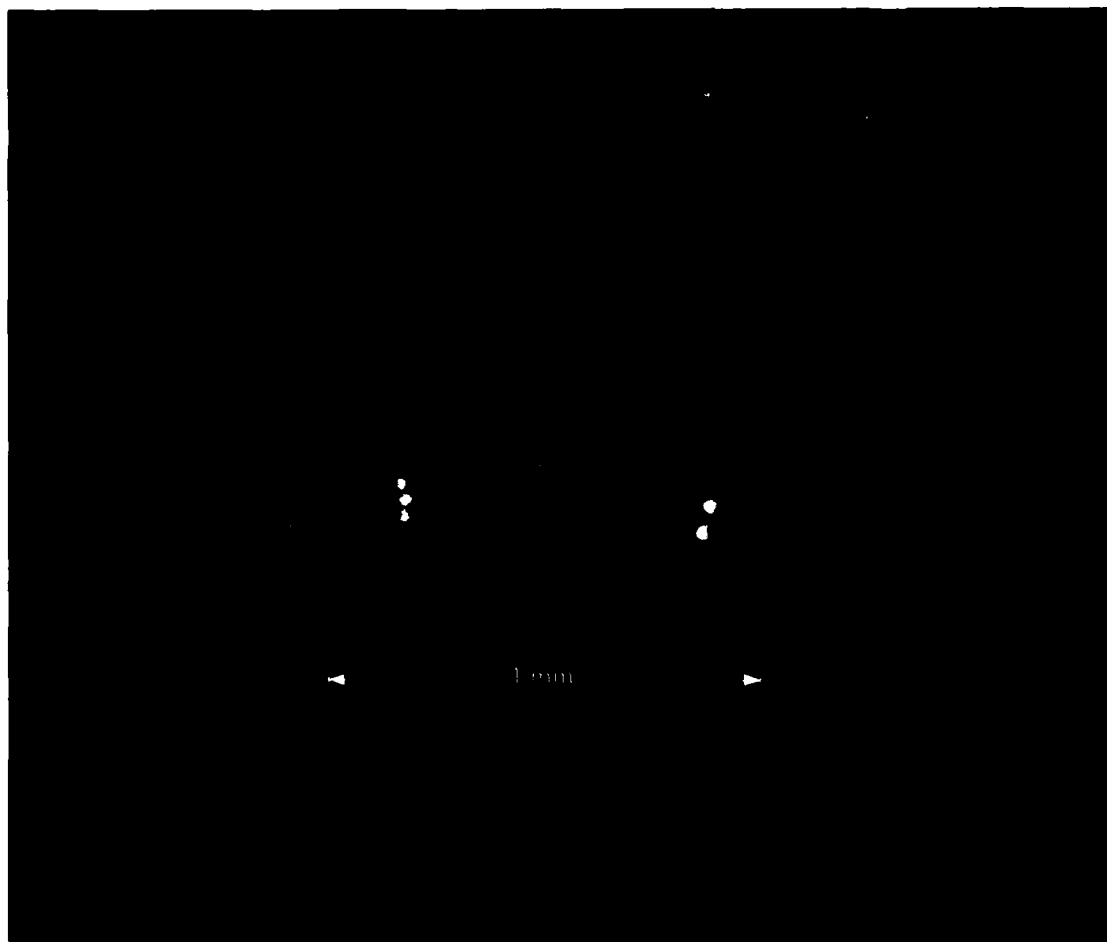


FIGURE 4.2  
ELECTRODE CONFIGURATION



**FIGURE 4.3**  
**PHOTOGRAPH OF A SPARK DISCHARGE**

compressible dielectric layer (commonly air), and a metallic backplate. The diaphragm and the backplate, separated by the dielectric, act as a condenser, across which is imposed a dc bias voltage (typically about 200 V). Sound pressure on the diaphragm changes the spacing between it and the backplate, thus altering the capacitance of the microphone. If a constant charge is maintained on the condenser plates a corresponding voltage is induced, which is fed to the input of a preamplifier.

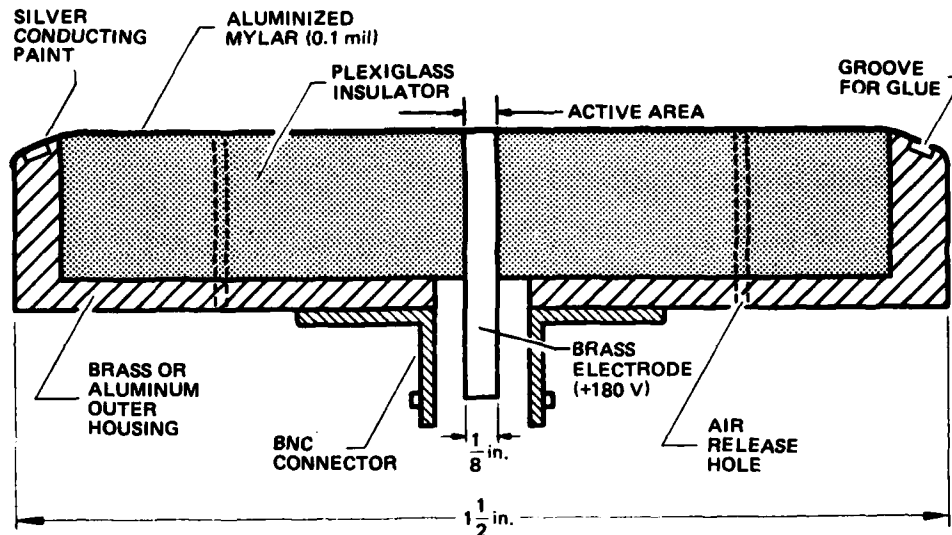
Cornet's and Anderson's microphones were built utilizing the case of a standard BNC connector as an outer housing. A plexiglass insulator was machined and force-fit or cemented into the outer housing. A small hole was drilled in the insulator for the backplate electrode, which was then fit into the hole and cemented in place. The diaphragm material used was 1/8 mil mylar metalized on one side. The mylar was laid, metalized side up, directly on the backplate surface. The only air gap (and only stiffness) was provided by tiny pockets of air trapped in the microscopically rough surface of the backplate.

Diffraction at the outer edges of the microphone face gives rise to an inverted replica of the incident wave. If the outer housing is small, the diffracted signal arrives shortly after the incident wave and interferes with it. If the microphone housing is made sufficiently large, however, the diffracted signal is delayed long enough that it may be ignored. Cornet and Anderson loosely fit a plane, plexiglass baffle about the microphone housing to delay the diffracted signal. Our first rise time measurements were made with this system. However, it was very difficult to fit the baffle securely on the microphone housing. There tended to be a gap or step at the baffle-microphone juncture. The

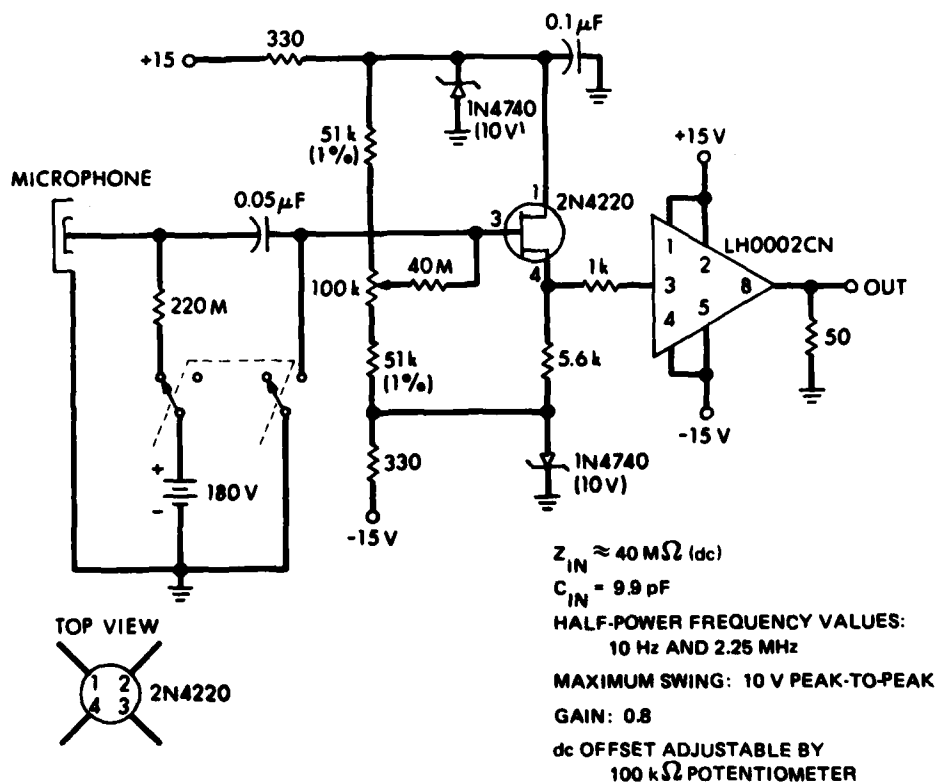
discontinuity at the juncture apparently gave rise to diffracted waves, which contaminated the received signal.

We modified the microphone design hoping to avoid signal contamination. New microphones combining the microphone and baffle in one system were built. The diameter of the microphone housing was expanded to 1.5 in. The remainder of the front surface of the microphone is extra insulator area to act as a baffle. A cutaway view of our microphone is shown in Fig. 4.4(a). The outer housing is machined from brass or aluminum. A BNC connector is attached beneath the housing. Cornet's method of fitting the insulator and backplate in the housing was used.

The procedure used to finish the backplate is the most critical step in the construction of the microphone. First, a lathe was used to machine the face of the microphone flat. Next, the backplate was smoothed using No. 600 silicon carbon sandpaper. The microphone was then placed in an ultrasonic cleaner to remove the grit particles. Finally, the surface was buffed and polished. This process created a random distribution of air filled microscopic cavities, each having a different resonance frequency. The mass of the diaphragm of each cavity and the spring formed by the air trapped in the cavity is modeled as a small oscillator. The resonance frequency of the microphone is determined by the overall resonance of all the cavities operating in parallel. The response of many oscillators in parallel, each having a different resonance frequency, is much flatter than that for a single oscillator; see Cornet.<sup>35</sup> As a result, the microphone is less likely to ring. To make the resonance frequency of each individual oscillator as high as possible, the oscillator mass should be as small as possible, i.e., the mylar should be as



(a) CUTAWAY VIEW OF THE MICROPHONE



(b) FIELD EFFECT TRANSISTOR PREAMPLIFIER

FIGURE 4.4  
 MICROPHONE AND PREAMPLIFIER

thin as possible. The mylar used for our microphones was 1/10 mil (Sheldahl Company, Northfield, Minnesota 55057).

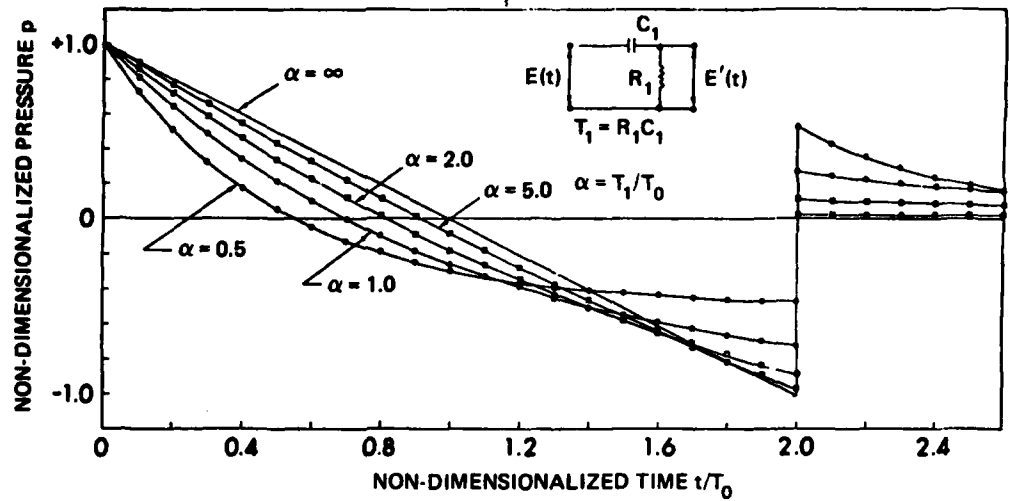
We designed the backplate such that the measurement of rise time would not be limited by the spherical waves we intend to use. A backplate diameter of 1/8 in. was chosen. The difference between the time a spherical wave of radius 10 cm reaches the center of the backplate and the time it reaches the edge of the backplate is 0.04  $\mu$ sec. We assume that the microphone is effectively a point detector because the active area is very small. In particular, if the source and microphone are misaligned by  $1^\circ$ , the response to a 1.6 MHz signal is down 0.4 dB. Below 56 kHz the microphone is omnidirectional ( $\theta_{HP}=90^\circ$ ) within  $\pm 3$  dB.

The FET preamplifier constructed by Cornet was used in our early experiments. We found that the dynamic range was insufficient for measuring strong signals close to the spark. L. A. Thompson designed a new preamplifier, similar in design to Cornet's, that has a much greater dynamic range and a better frequency response. A circuit diagram is shown in Fig. 4.4(b). The maximum voltage swing is 10 V peak to peak. The low and high frequency 3 dB down points are 10 Hz and 2.25 MHz, respectively. The input capacitance is 9.9 pF, approximately one-fifth that of Cornet's preamplifier. The preamplifier contains the bias voltage (180 V) for the microphone. Also included is a line driver, which drives a 50  $\Omega$  cable without much loss. The switch shown is used to disconnect the batteries so they do not drain while the preamplifier is not in use. An early difficulty with the preamplifier was a dc offset in the output. A 100 k $\Omega$  potentiometer was installed in the circuit to allow the offset to be balanced out.

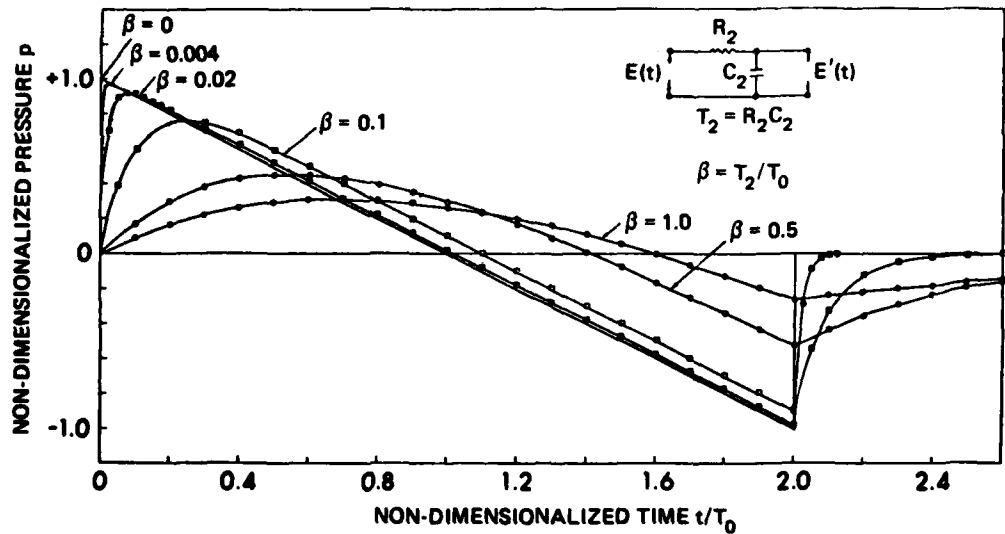
In increasing the frequency response of the microphone-preamplifier system, we lost quite a bit of sensitivity. To avoid the cable noise interfering with the signal, it was necessary to amplify the signal before sending it to the oscilloscope. We used an HP461A amplifier for this purpose.

There were some limitations on our receiving system. The HP461A amplifier has a low frequency 3 dB down point of 360 Hz. The FET preamplifier has a high frequency 3 dB down point of 2.25 MHz, and the microphone has a high frequency 3 dB down point of about 1 MHz. The rolloff at the low frequency end is determined by the HP461A amplifier (18 dB/octave). The FET preamplifier rolls off at the high frequency end at 6 dB/octave. The high frequency rolloff of the system, however, is set by the condenser microphone. Generally, a condenser microphone rolls off at 12 dB/octave. However, since our microphone is really many small microphones, each with a different resonance frequency, in parallel, the rolloff is expected to be much gentler.

Crocker<sup>36</sup> has developed a model for the effect of limited bandwidth of a receiver on response to an ideal N wave. The model is valid only for rolloffs of 6 dB/octave. Therefore we cannot adjust our waveforms using the results. However, we use his model to get a general idea of the effects of our limited bandwidth. Crocker<sup>36</sup> dealt with the low frequency limitation, which can be modeled as a high pass filter, and the high frequency limitation, which can be modeled as a low pass filter separately. His analysis is shown in Fig. 4.5. In the case of low frequency limitation, the effects vary depending on the ratio  $\alpha = T_1/T_0$ , where  $T_1$  is the RC time constant of the high pass filter. As  $\alpha$  decreases



(a) LOW FREQUENCY LIMITED (HIGH PASS FILTER)



(b) HIGH FREQUENCY LIMITED (LOW PASS FILTER)

**FIGURE 4.5**  
**EFFECTS OF LIMITED FREQUENCY RESPONSE ON AN IDEAL N-WAVE**

From the report by M. J. Crocker, "Measurement of Sonic Boom with Limited Frequency Response Instrumentation: A Theoretical Study," Wyle Labs Research Staff Report WR 66-20, April 1966.

from infinity to zero, the midsection of the wave distorts, thus decreasing the half duration (see Fig. 4.5(a)). Using the model to estimate the reduction in half duration for our system we found that the maximum error is 4.1%. The high frequency limitation is determined by the ratio  $\beta = T_2/T_0$ , where  $T_2$  is the RC time constant of the low pass filter. As  $\beta$  grows from zero to infinity, the rise time increases, amplitude decreases, and the half duration increases (see Fig. 4.5(b)). For our high frequency 3 dB down point (1 MHz), we find that  $T_2 = 1 \mu\text{sec}$ . For an N wave with  $T_0 = 20 \mu\text{sec}$  (a typical value for our experimental N waves), this gives  $\beta = 1/20 = 0.05$ . By interpolating between the  $\beta = 0.02$  and  $\beta = 0.1$  curves, one can see that a rise time of order  $t_r = 0.2 T_0 = 4 \mu\text{sec}$  is indicated. However, we were able to measure rise times as low as  $1 \mu\text{sec}$ . Therefore, we conclude that Crocker's model for the high frequency limitation does not fit our receiving system.

#### 4. Data Capture and Storage

The signal from the preamplifier, after going through the HP461A amplifier, was input to a Nicolet Model 2090-III digital oscilloscope equipped with a Model 206-2 plug-in unit. A magnetic disk memory was used to store signals for further analysis. The disk is divided into 8 "tracks", each having a capacity of 4096 data points. Each "track" can be divided into "quarters", each having a capacity of 1024 data points. Use of an entire "track" permitted the storage of 2 msec of data with a time resolution of  $0.5 \mu\text{sec/point}$  and 12-bit accuracy. Electromagnetic radiation was picked up by a loop antenna, amplified by a HP450A amplifier, and then used to open the gate of a Chronetics, Inc., Model PG-11 pulse generator, which in turn triggered the oscilloscope. A delay set by the

width of the pulse from the Chronetics unit made it possible to hold the oscilloscope trigger until the acoustic wave arrived at the microphone. Captured waveforms were either saved on the disk or plotted directly on HP7045A X-Y recorder.

### B. Calibration

The technique used to calibrate the microphone-preamplifier system has been described by Davy and Blackstock<sup>37</sup> and, in more detail, by Cornet,<sup>35</sup> Anderson,<sup>30</sup> Cobb,<sup>38</sup> and Essert.<sup>32</sup> The technique is based upon the lengthening and excess attenuation of an outgoing spherical N wave. We use only the positive half of our spark produced N waves, because the negative half is not sufficiently close to the ideal N wave shape. The peak pressure amplitude  $P$  and half duration  $T$  of an ideal, spherically spreading N wave at radial distance  $r$  are related to the pressure  $P_0$  and half duration  $T_0$  at some reference position  $r_0$  by the following:

$$rP = r_0 P_0 \left[ 1 + \sigma_0 \ln\left(\frac{r}{r_0}\right) \right]^{-1/2}, \quad (4.1)$$

$$T = T_0 \left[ 1 + \sigma_0 \ln\left(\frac{r}{r_0}\right) \right]^{1/2}, \quad (4.2)$$

where

$$\sigma_0 = \frac{(\gamma+1) r_0 P_0}{2 \rho_0 c_0^3 T_0} \quad (4.3)$$

Equation (4.1) is multiplied by Eq. (4.2) to find

$$TrP = T_0 r_0 P_0, \quad (4.4)$$

which shows that the triple product has the same value regardless of the distance. The peak pressure  $P$  and the peak voltage  $E$  are related by

$$P = E/S \quad , \quad (4.5)$$

where S is the sensitivity of the microphone-preamplifier system.

Combining Eqs. (4.3), (4.4), and (4.5) yields

$$S = \frac{2\rho_0 c_0^3 \sigma_0 T_0^2}{(\gamma+1) \overline{\text{Tr}E}} \quad . \quad (4.6)$$

We have replaced  $T_0 r_0 E_0$  by  $\overline{\text{Tr}E}$ , an average value of the triple product, in Eq. (4.6) because the accuracy of an average is greater than that of a single measurement. The parameter  $\overline{\text{Tr}E}$  is determined from measurements of the N wave amplitude and half duration at various distances. If Eq. (4.2) is squared, the result is

$$T^2 = T_0^2 + \sigma_0 T_0^2 \ln\left(\frac{r}{r_0}\right) \quad .$$

The quantity  $\sigma_0 T_0^2$  may thus be found by plotting data for  $T^2$  against  $\ln(r/r_0)$  and measuring the slope of the straight line that results. A least squares fit is used.

Although with the Grozier spark generator a spark could be obtained at a consistent breakdown voltage, it was found that T and P varied slightly with each spark. To reduce this variability we used a special procedure developed by Essert.<sup>32</sup> An "average" waveform was found as follows: At each measurement position ten N waveforms were captured and stored on the disk. The values for T and P were recorded for each waveform. Average values for T and P were found from the data. Then we captured several waveforms until we found one that had the average values of T and P. This waveform was plotted on the X-Y recorder and used for further analysis.

Ringling and a finite rise time were found in the measured waveforms. It was necessary to idealize the measured waveforms, since the calibration procedure is based on an ideal N wave. The ringing in the linear decay portion of the waveform was smoothed out by assuming that the actual waveform passed through the center of oscillations. We placed the idealized head shock at a point midway between the foot and the peak of the measured waveform. The procedure is shown in Fig. 4.6. The peak voltage  $E$  and half duration  $T$  were determined from the ideal waveform and used in the calculations for calibration. For further descriptions on the idealizing procedure, see Cobb,<sup>38</sup> Anderson,<sup>30</sup> and Essert.<sup>32</sup>

Two different microphone-preamplifier systems were used in our experiment. The first system consisted of one of the small microphones, with fitted baffle, and Cornet's preamplifier. N waves were recorded at eight source-receiver distances from 10 to 180 cm for a spark energy of 1.04 J. The temperature was 75°F and the relative humidity 66%. Figure 4.7 shows the calculation of  $\overline{\text{Tr}E}$  and  $\sigma_0 T_0^2$ . The results are summarized as follows

$$\overline{\text{Tr}E} = 144.4 \text{ } \mu\text{sec} \times \text{cm} \times \text{V}, \text{ standard deviation} = 3.26\%,$$

$$\sigma_0 T_0^2 = 20.223 \text{ } \mu\text{sec}^2, \text{ correlation coefficient} = 0.996,$$

and, finally,

$$S = 5.68 \text{ mbar/V}$$

or

$$\bar{S} = -75.09 \text{ dB re } 1 \text{ V}/\mu\text{bar},$$

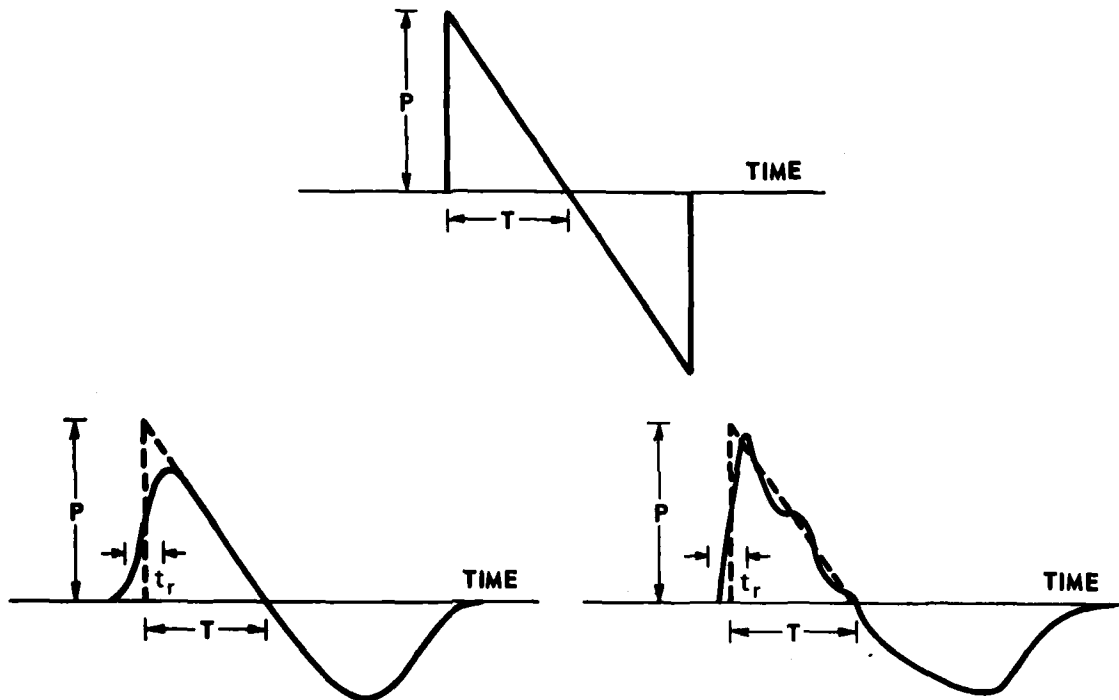


FIGURE 4.6  
IDEAL N WAVE (ABOVE) AND IDEALIZATIONS OF MEASURED N WAVES (BELOW)

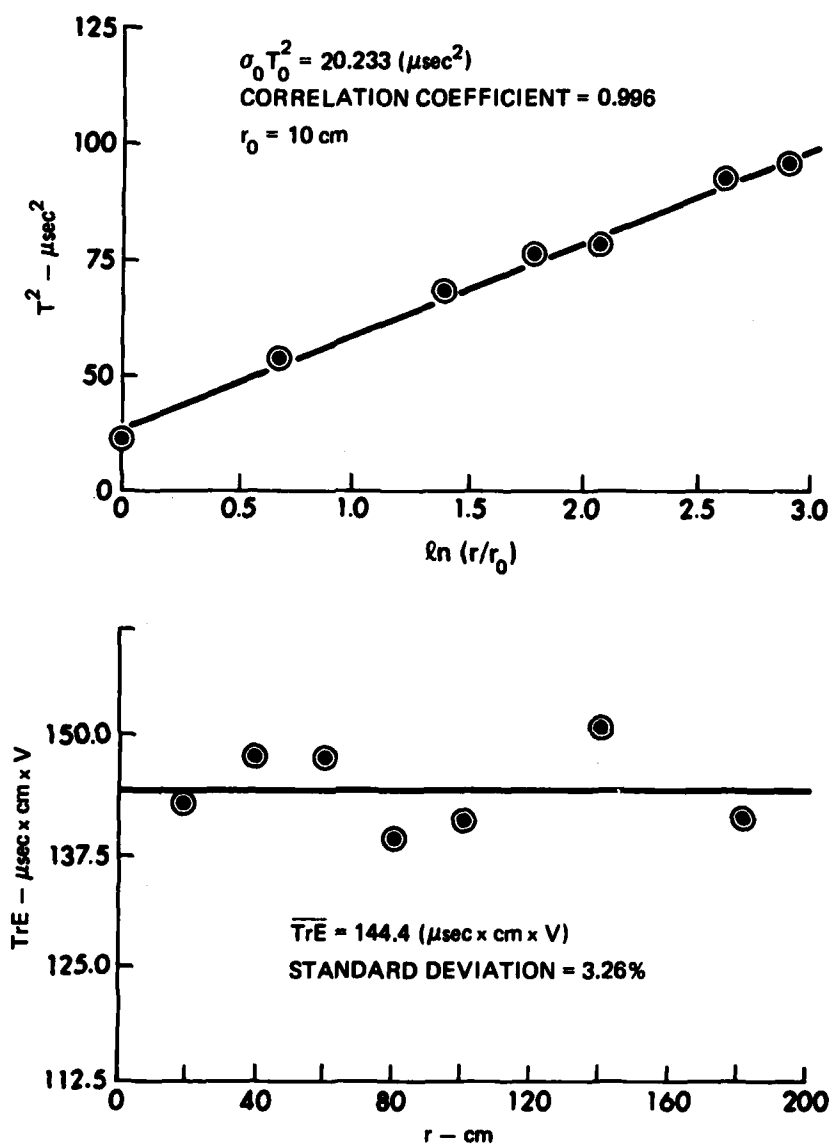


FIGURE 4.7  
 MICROPHONE CALIBRATION DATA  
 (OLD SYSTEM)

where  $\bar{S} = 20 \log \left( \frac{S}{S_{\text{ref}}} \right)$ , and  $S_{\text{ref}}$  is the reference sensitivity 1 V/ $\mu\text{bar}$ . This value is the sensitivity of the entire microphone-preamplifier system.

The second system consisted of the new preamplifier and the new, larger microphone. In the calibration run for this system N waves were recorded at ten source-receiver distances from 30 to 200 cm for a spark energy of 4.35 J. The temperature was 73°F and the relative humidity 43%. The methods described above were used to find  $\overline{\text{TrE}}$  and  $\sigma_0 T_0^2$ . The results are summarized as follows (see Fig. 4.8).

$$\overline{\text{TrE}} = 27.357 \text{ } \mu\text{sec} \times \text{cm} \times \text{V}, \text{ standard deviation} = 6.9\%$$

$$\sigma_0 T_0^2 = 151.92 \text{ } \mu\text{sec}^2, \text{ correlation coefficient} = 0.987,$$

and, finally

$$S = 225.23 \text{ mbar/V}$$

or

$$\bar{S} = -107.05 \text{ dB re } 1 \text{ V}/\mu\text{bar}.$$

This is the value of the sensitivity of the microphone-preamplifier system, with 0 dB gain from the HP461A amplifier.

Since the calibration method used was an unconventional one, a completely different calibration was performed to check our results. We used a comparison method, in which the same sound field is measured with two different microphones, one of which has a known calibration. The other microphone was our new one. A plane wave field in a 2 in. diam tube was chosen to make this calibration. The tube was 3.283 ft long. A JBL Model 375 horn driver was attached on one end of the tube. On the other end we attached a flange, specially machined to hold our microphone (designated microphone MM) and a Bruel and Kjaer (B&K) 1/4 in.

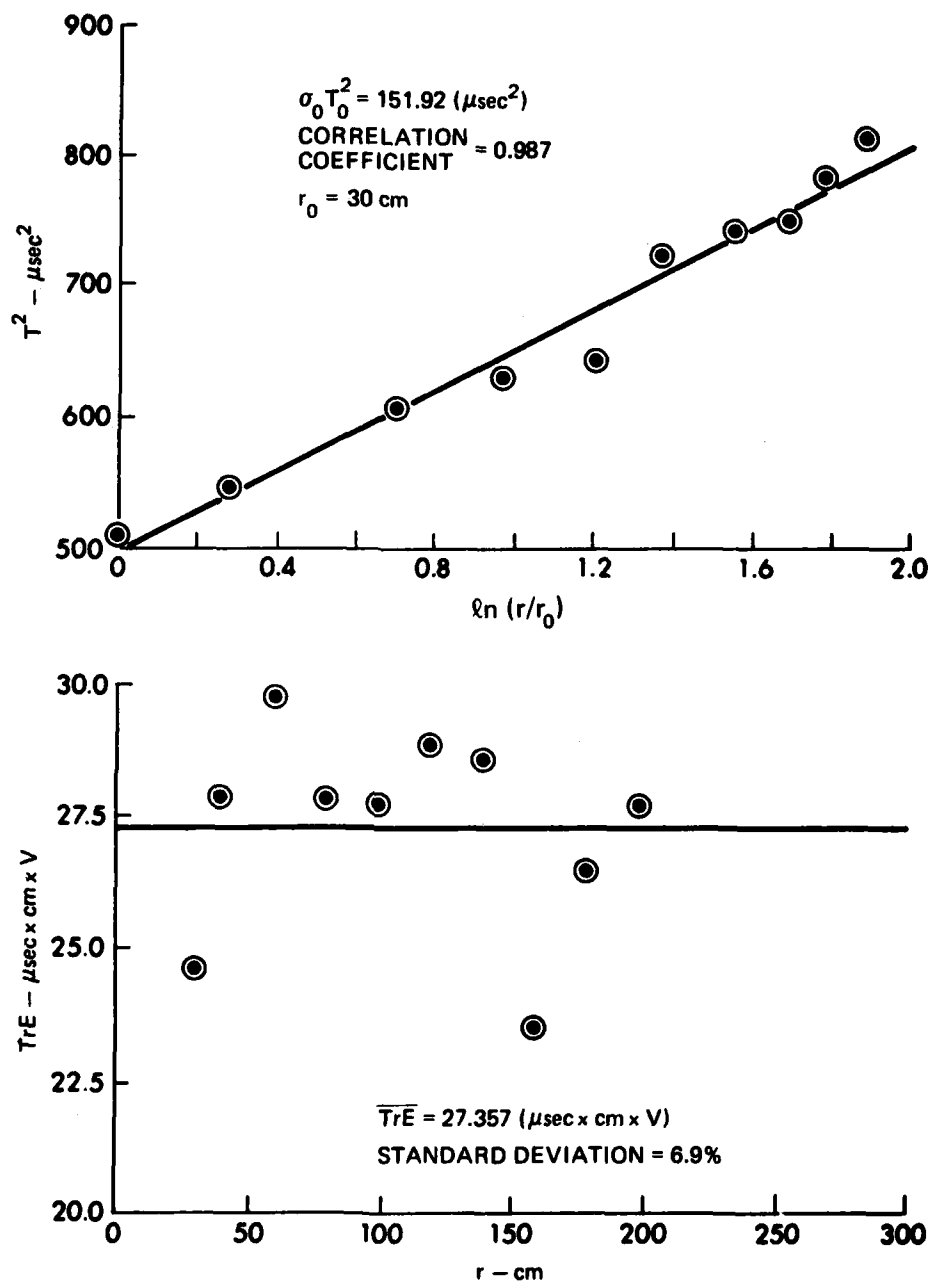


FIGURE 4.8  
 MICROPHONE CALIBRATION DATA  
 (NEW SYSTEM)

microphone. A cutaway view of the flange is shown in Fig. 4.9. Both microphones were mounted flush with the inner wall of the flange. Pulsed sine waves at test frequencies of 0.5, 1, 2, and 4 kHz were sent down the tube via the driver, and the signal was picked up with both microphones. Prior to the calibration run the B&K microphone was calibrated with a pistonphone. The output signals from the two microphones were captured on the Nicolet oscilloscope, which was triggered by the pulser, and their amplitudes recorded in millivolts (see Fig. 4.10 for setup). The sensitivity of microphone MM was calculated as follows.

$$\bar{S}_{MM} = 20 \log \left[ \frac{S_{MM}}{S_{ref}} \right] = 20 \log \left[ \left( \frac{S_{BK}}{S_{ref}} \right) \left( \frac{E_{MM}}{E_{BK}} \right) \right], \quad (4.7)$$

where  $S_{BK}$  is the sensitivity of the B&K microphone,  $S_{ref}$  is the reference sensitivity (1 V/ $\mu$ bar),  $E_{MM}$  is the output voltage of microphone MM, and  $E_{BK}$  is the output voltage of the B&K microphone. A plot of sensitivity versus frequency gives the frequency response of the microphone-preamplifier system (see Fig. 4.11). Since we expected the frequency response to be flat in the frequency region that we measured (0.5-4 kHz), the best measure of sensitivity was an average of the values at the four test frequencies.

Since the two microphones were physically separated, they measured slightly different sound fields. We account for this by adjusting the amplitude recorded by the B&K microphone to the value it would have been if it had been in exactly the same position as microphone MM. If the incident wave at microphone MM is described by

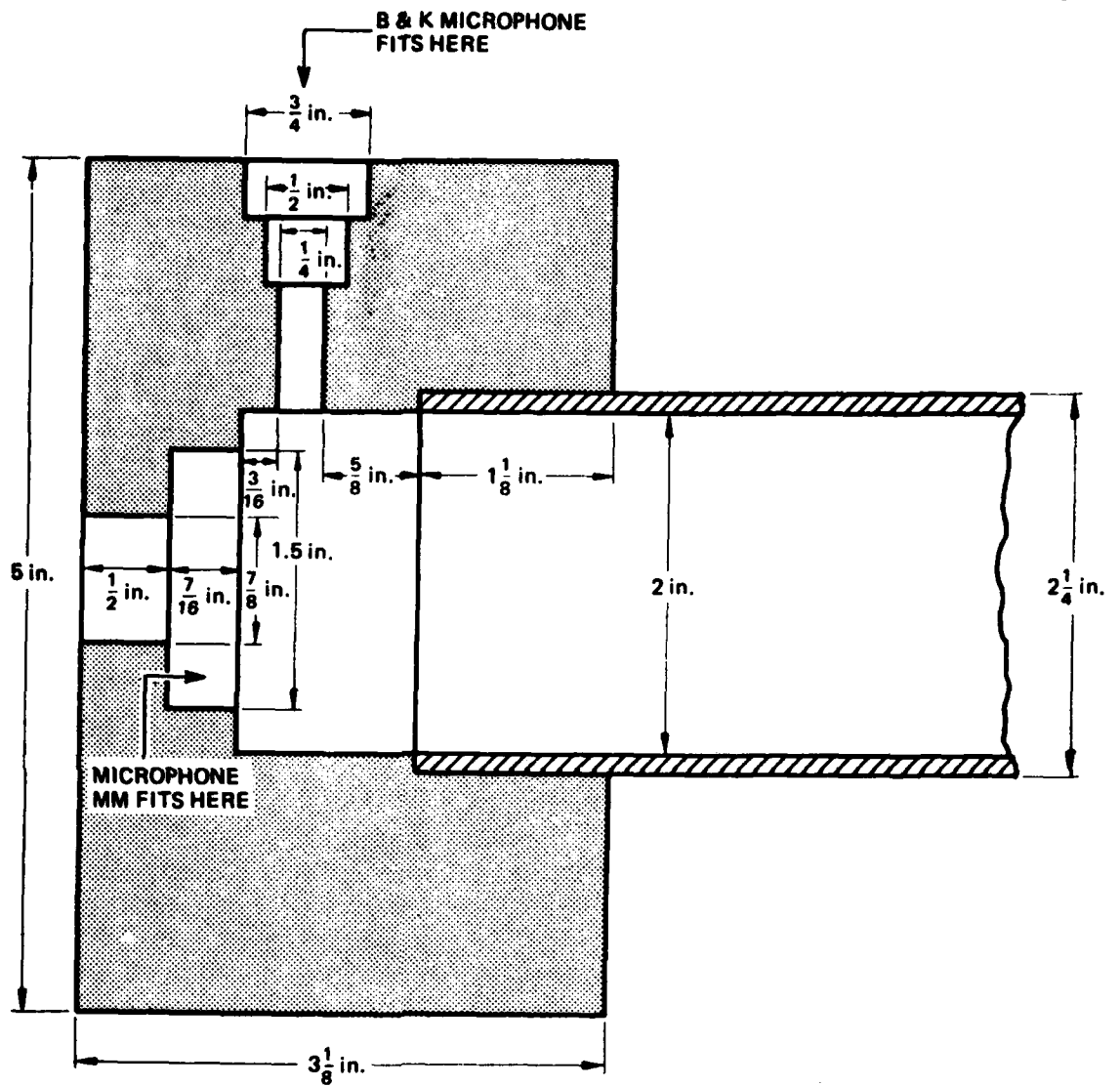
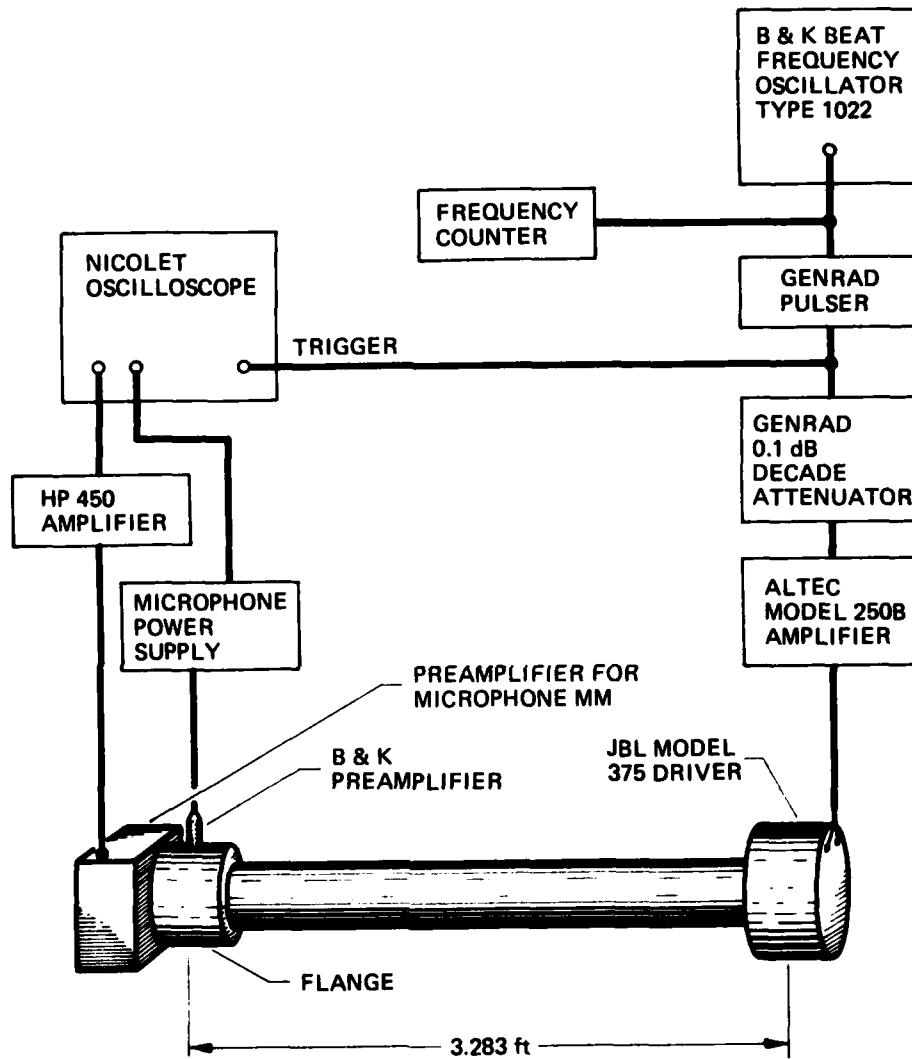


FIGURE 4.9  
FLANGE FOR CALIBRATION IN 2 in. TUBE



**FIGURE 4.10**  
**TUBE CALIBRATION APPARATUS**

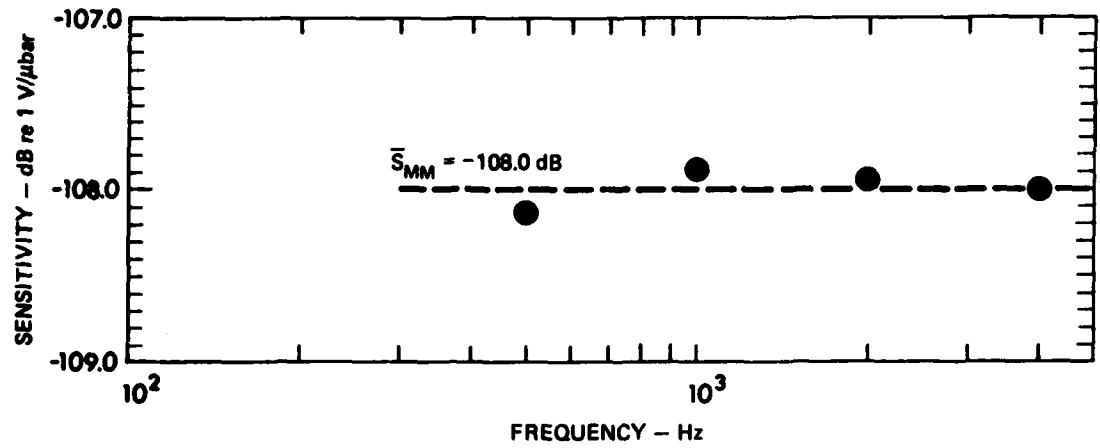


FIGURE 4.11  
COMPARISON METHOD CALIBRATION DATA

$$I = A e^{j\omega t} ,$$

then, because the surface is rigid, the reflected wave also has an amplitude  $A$  so that the total pressure is

$$P_{MM} = 2A e^{j\omega t} .$$

The combination of the incident plus reflected signals seen by the B&K microphone, which is  $\Delta x$  away from microphone MM, is

$$\begin{aligned} P_{BK} &= A e^{j\omega(t+\Delta x/c_0)} + A e^{j\omega(t-\Delta x/c_0)} \\ &= 2A \cos(k\Delta x) e^{j\omega t} . \end{aligned}$$

Therefore,

$$\frac{P_{BK}}{P_{MM}} = \cos(2\pi f\Delta x/c_0) . \quad (4.8)$$

The correction factor, in decibels, is written as

$$B = 20 \log[\cos(2\pi f\Delta x/c_0)] . \quad (4.9)$$

The corrections at the test frequencies are as follows: -0.018 dB at 0.5 kHz; -0.073 dB at 1 kHz; -0.293 dB at 2 kHz; and -1.213 dB at 4 kHz. The adjusted data is shown in Fig. 4.11. The average sensitivity is -108 dB re 1 V/ $\mu$ bar, a value that is within 1 dB of that measured by the first method. The validity of the first method, therefore, is confirmed. We used the sensitivity determined by the first method for our rise time measurements.

### C. Alignment and Procedure

Alignment of the spark source and microphone face was a critical aspect of this experiment. The better the alignment, the less

critical the fact that our microphone is not a true point receiver (see the discussion of microphone directivity in the section on the receiving system). The alignment was done with the light beam from a Hughes Model 31931H laser. First, the laser beam was aligned parallel with the axis of the optical bench. This was done by shining the laser beam on a screen mounted on the bench and adjusting the horizontal position of the laser until the beam did not shift when the screen was moved down the bench. The laser was then secured in that position. The spark gap and microphone face were aligned along an axis formed by the laser beam. The electrode holder and laser were adjusted vertically until the beam passed through the center of the spark gap and was reflected from the center of the microphone face. The electrode holder was then adjusted, by eye, until its plane was perpendicular to the laser beam. Finally the tilt of the microphone face was adjusted until the reflected laser beam was superimposed on the incident beam. We were then sure that the line between the center of the spark gap and microphone face was perpendicular to the microphone face.

After the apparatus was aligned, we were ready to take data. First, the microphone-preamplifier system was calibrated (as described above). Next, the temperature and relative humidity were measured and recorded. This was very important since the predictions of our models depended on these factors. The temperature, as measured with a mercury thermometer, remained fairly constant all year long at  $75^{\circ} \pm 2^{\circ}\text{F}$ . The humidity was measured with a Brooklyn direct reading hygrometer. The range of relative humidities was 40-66%. The lower humidities generally

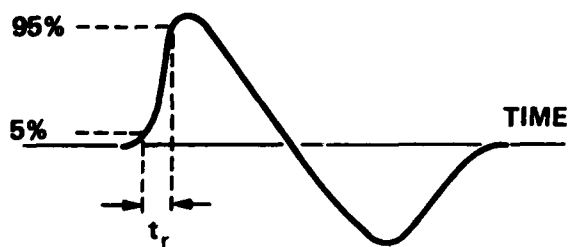
occurred in the winter months and the higher humidities in the spring and summer months.

Several data runs were then taken. Waveforms were captured at several source-receiver distances. The same averaging procedure used in the calibration was used to determine which waveforms to plot on the X-Y recorder. Some waveforms were also saved on a disk. The waveforms were then analyzed to determine the rise time. Two different definitions for rise time were used in this study, as shown in Fig. 4.12. In the first definition, the rise time is described as the time required for the local pressure to increase from 5% to 95% of its peak value. The rise time can also be defined in terms of the slope of the initial shock. In this case the rise time equals the amplitude divided by the slope of the rise at its midpoint. We use the second rise time definition to analyze our data. This definition is chosen because it is the one most currently in use in the literature.

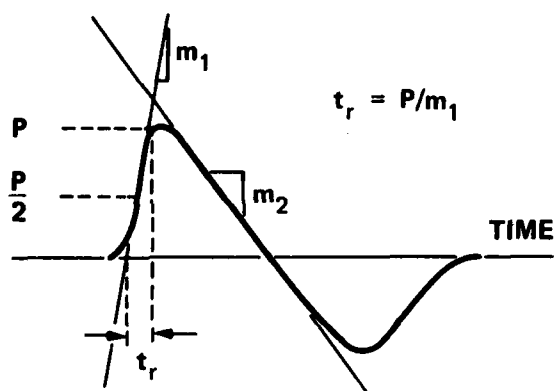
Some sample waveforms are shown in Fig. 4.13. A typical waveform with a very short rise time is shown in Fig. 4.13(a), one with a much longer rise time in Fig. 4.13(b).

#### D. Limits on Rise Time Measurement Capability

There are four factors which limit the rise time measurement capability of our measurement system. The first limitation is set by the oscilloscope. Since the time resolution is at best 0.5  $\mu\text{sec}/\text{point}$ , we could not possibly measure rise times shorter than 0.5  $\mu\text{sec}$ . The second limitation is set by the microphone. The shortest rise time we measured with microphone MM is about 0.65  $\mu\text{sec}$ . The third limitation is associated with the geometry of the spark source. For example, the electrode holder

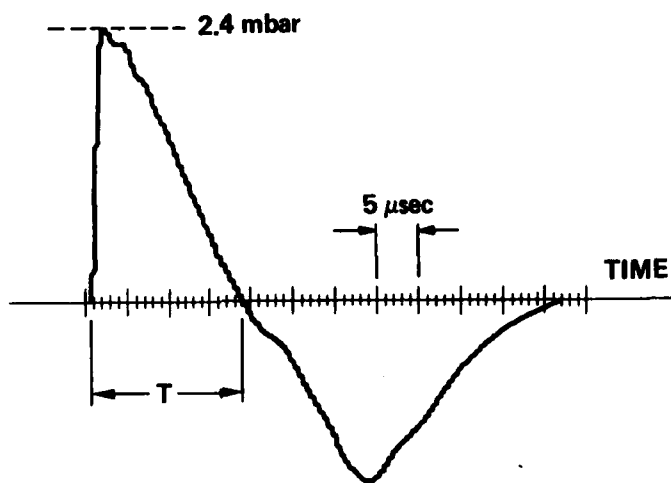


(a) RISE TIME DEFINITION No. 1

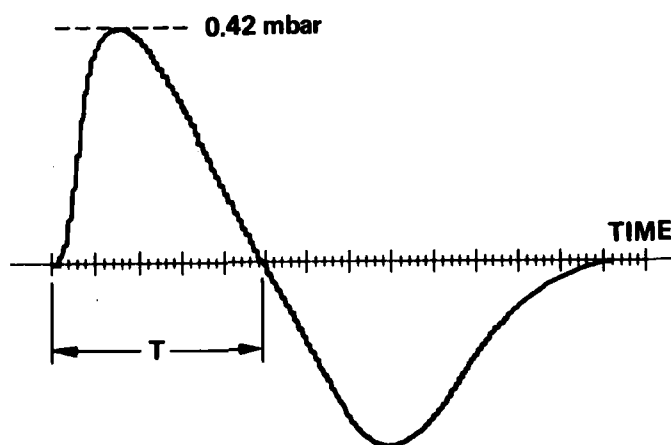


(b) RISE TIME DEFINITION No. 2

FIGURE 4.12  
DEFINITION OF RISE TIME



(a) PROPAGATION DISTANCE = 0.75 m



(b) PROPAGATION DISTANCE = 3.0 m

**FIGURE 4.13**  
**SAMPLE EXPERIMENTAL WAVEFORMS**  
SPARK ENERGY = 1.96 J  
TIME RESOLUTION = 0.5  $\mu\text{sec}$

is adjusted perpendicular to the laser beam by eye. If the gap were slightly tilted, one end of the source would be closer to the microphone face than the other. If the trigger electrode is not centered between the electrodes or not on the gap axis, there may be a path length difference from various parts of the spark to the microphone. Lastly, the electrodes may be slightly offset from each other. Although no real analysis of the effect of these misalignments was made, it is worthwhile noting that a path length difference corresponding to a time delay ( $\Delta t$ ) of 1.0  $\mu\text{sec}$  is

$$\begin{aligned}\Delta x &= c_0 \Delta t \\ &= 0.345 \text{ mm} \quad .\end{aligned}$$

If any of the problems discussed above results in a path length difference of 0.345 mm, our rise time limitation is 1.0  $\mu\text{sec}$ .

Although some of our initial waveforms might actually have rise times smaller than 1.0  $\mu\text{sec}$ , most of our data are not affected by the limitations imposed by the equipment. As will be seen in Chapter 5, most of our measured rise times were greater than 1.0  $\mu\text{sec}$ .

1

CHAPTER 5  
MEASUREMENTS AND COMPARISONS WITH THEORETICAL PREDICTIONS

A. Introduction

In this chapter we report our experimental results and compare them with the predictions obtained from the models described in Chaps. 2 and 3. In Section B our results are compared with the thermoviscous and relaxation model predictions. As noted in Chap. 2 these models are derived for a step shock. In Section C we present a comparison of the waveforms computed by our propagation algorithm with those from our experiments.

Three different kinds of data runs were taken. First, with the spark energy and gap length held constant, waveforms were captured at specific distances between 10 and 550 cm. In the second kind of data run we varied the spark energy, gap length, and propagation distance in such a way that the half duration was held constant. We took data with constant half duration, because we wanted to check whether there was no dependence of rise time on the half duration, as the analytical predictions indicate. In the last kind of data run spark energy, gap length, and propagation distance were varied so as to keep the peak pressure constant.

B. Comparison with Thermoviscous and Relaxation Models

We used two different graphical presentations to compare the data with the predictions from the models. The first is a plot of the rise time ( $t_r$ ) versus the inverse of the peak pressure (given by Eqs. (2.7b) and (2.14)). This method was chosen because the rise time is described as a

constant times the inverse of the peak pressure in the analytical models. The second plot is of the slope of the rise at its midpoint ( $m_1$ ) versus the peak pressure squared (given by Eqs. (2.7a) and (2.13a)). We chose to use this method after we compared some of our computed waveforms with the experimental waveforms. We found that although the peak pressures of the two waveforms were not exactly the same (error  $\approx 8.5\%$ ), the slope of the rises were. Since we also use the slope of the rise in one of our rise time definitions, this method seemed reasonable.

We took many runs with both constant energy and constant half duration. The runs presented here are representative samples. We list the different runs along with pertinent information about them in Tables 5.1(a) and 5.1(b).

#### 1. Rise Time versus Inverse Peak Pressure

##### a. Constant Spark Energy

Basically, we found that the rise times we observed are closer to those predicted by the thermoviscous model than those predicted by the relaxation model. Furthermore, the experimental rise times agree better with TV2 than TV1. A plot of the results from several data runs is shown in Fig. 5.1. As noted in Chap. 4, equipment limitations prevented us from measuring a rise time of less than about  $1.0 \mu\text{sec}$ . This accounts for the bunching of points around  $1.0 \mu\text{sec}$ . As noted in Chap. 2, the predictions given by the relaxation model are only valid for fully dispersed shocks, i.e.,  $P < 1 \text{ mbar}$ . Therefore, the relaxation prediction is inapplicable over most of the plot region. However, we include the rise time prediction for a relaxing medium in Figs. 5.1 and 5.2, for the purpose of comparison with the thermoviscous prediction.

TABLE 5.1  
SUMMARY OF DATA RUNS

(a) CONSTANT ENERGY

<u>SPARK ENERGY</u> (J)	<u>GAP LENGTH</u> (mm)	<u>TEMPERATURE</u> (°F)	<u>RELATIVE HUMIDITY</u> (%)	<u>INITIAL PRESSURE</u> (mbar)	<u>INITIAL HALF DURATION</u> (μsec)	<u>MEASUREMENT RANGE</u> (cm)
0.061	1	73	60	1.03	9.0	50-300
1.08	-	-	-	8.66	7.5	10-300
1.96	-	75	66	7.33	15.5	30-325
2.88	-	75	66	6.12	15.5	30-300
2.88	1	75	63-64	5.39	21.6	30-550
3.13	2	76	60	8.25	17.0	30-450
4.81	2	73	40	4.50	25.0	60-450
5.78	2	75	60	12.29	24.5	30-400
6.48	4	77.5	56	14.41	22.1	30-450
9.68	1	74	63	10.98	19.7	30-450

(b) CONSTANT HALF DURATION

<u>HALF DURATION</u> (μsec)	<u>MEASUREMENT RANGE</u> (cm)	<u>RANGE SPARK ENERGY</u> (J)	<u>GAP LENGTH RANGE</u> (mm)	<u>TEMPERATURE</u> (°F)	<u>RELATIVE HUMIDITY</u> (%)
21.5	50-400	0.28-4.41	-	75	66
29.5	75-550	3.24-6.76	-	75	66
30.0	50-450	2.0-9.03	2-3	76	52
32.0	100-500	2.21-8.00	-	75	66
34.0	100-450	4.96-11.50	2-4	72	50
41.5	75-600	8.64-26.50	3-5	75	66

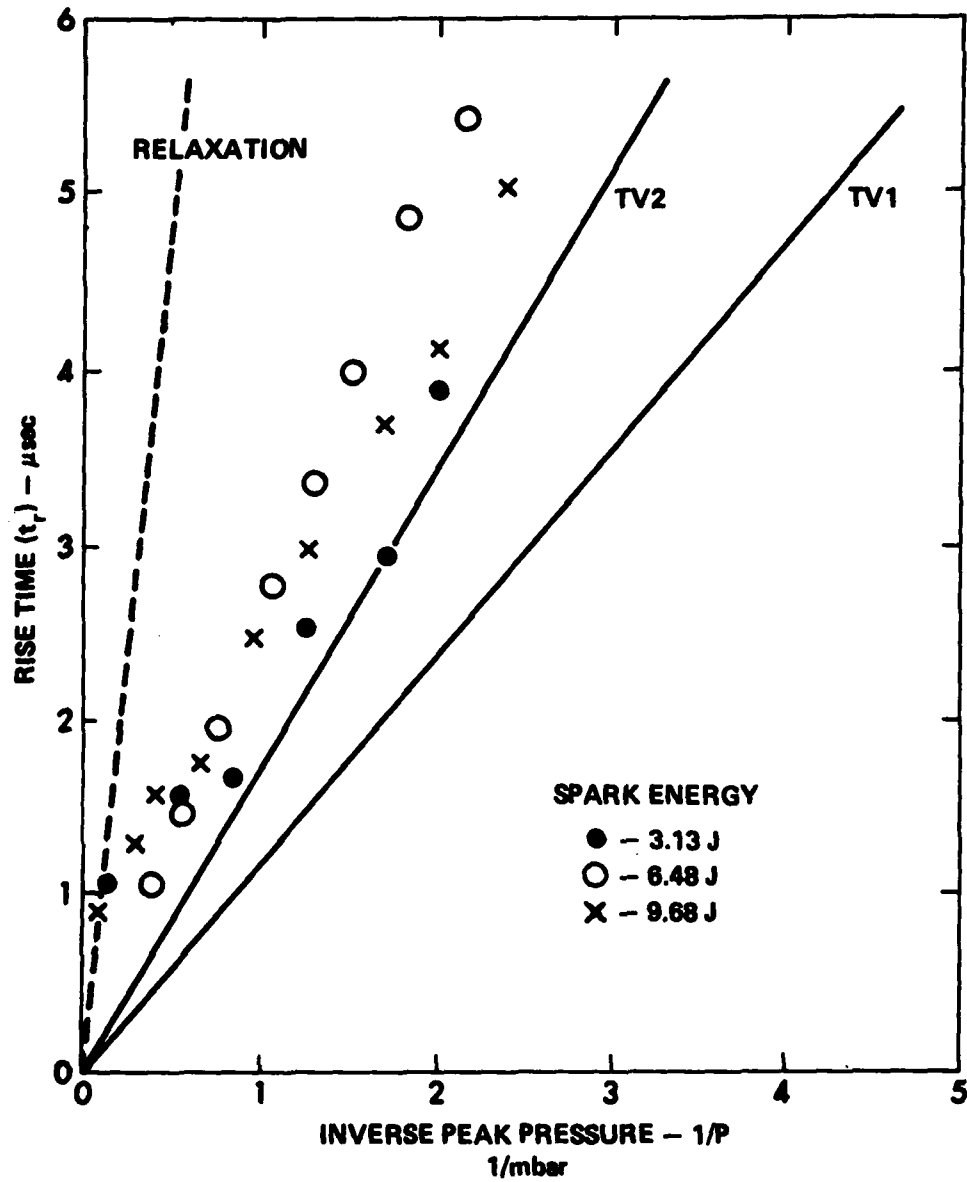


FIGURE 5.1  
FIRST METHOD OF ANALYSIS:  
CONSTANT SPARK ENERGY

b. Constant Half Duration

Again we found that the observed rise times were closer to those predicted by the thermoviscous model (TV2) than those predicted by the relaxation model. We captured waveforms with half durations from 21.5 to 41.5  $\mu\text{sec}$ . A plot of the results from three constant half duration runs is shown in Fig. 5.2. An interesting effect that may be seen in this plot is that the slope of the curve defined by the data points seems to increase as the half duration increases. This is rather curious because as the half duration increases the N wave begins to look more like a step shock. One conclusion is that the thermoviscous model is not necessarily better than the relaxation model. It may be that the half duration is not long enough to tell whether relaxation has an effect on the shock profile.

c. Constant Amplitude

Only one constant amplitude run was made. We captured several 0.62 mbar peak amplitude waveforms at source-receiver distances of 75-450 cm. According to both the thermoviscous and relaxation models, the rise times for all of these waveforms should be the same. We did not find this to be true. We measured the slope  $m_2$  of the linear decay portion of the waveforms and plotted the rise time versus slope; see Fig. 5.3. There is a fairly linear relationship between the rise time and the linear decay slope; as the slope increases the rise time decreases. These results confirm the results obtained in the constant half duration runs. As the half duration increases, the slope of the linear decay portion decreases and the rise time increases. It is possible that an N wave as long as a sonic boom would have a rise time

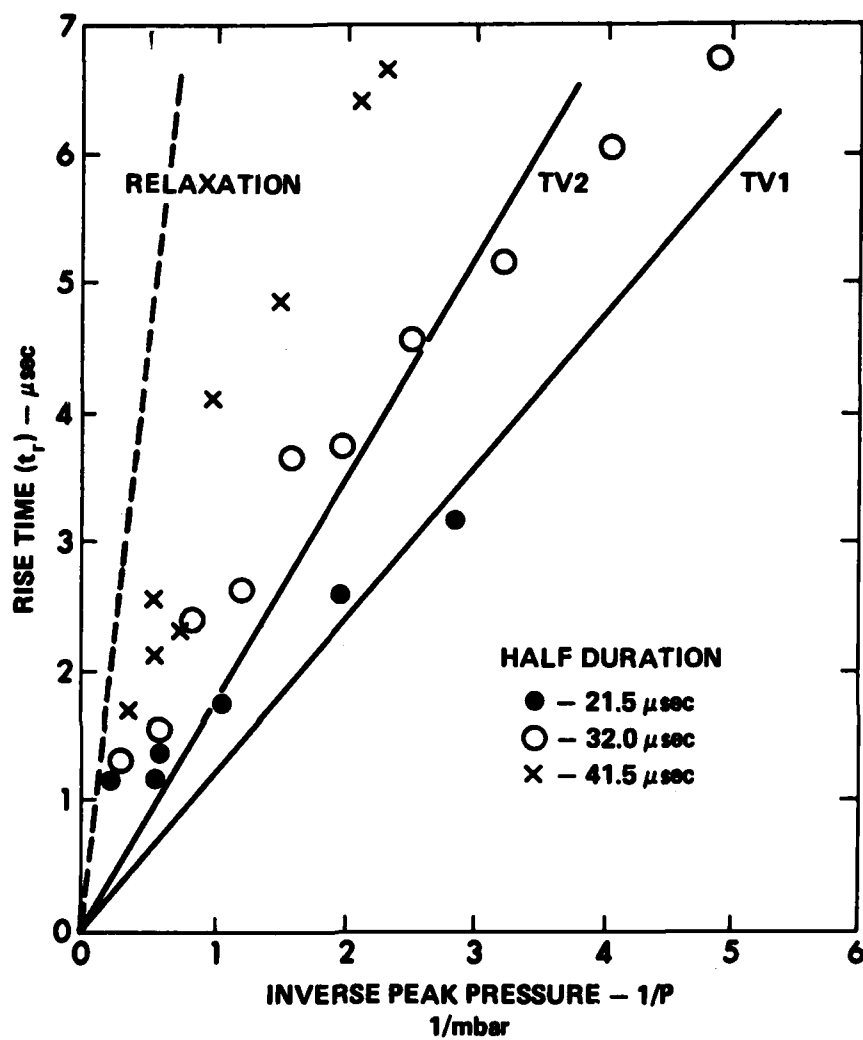


FIGURE 5.2  
FIRST METHOD OF ANALYSIS:  
CONSTANT HALF DURATION

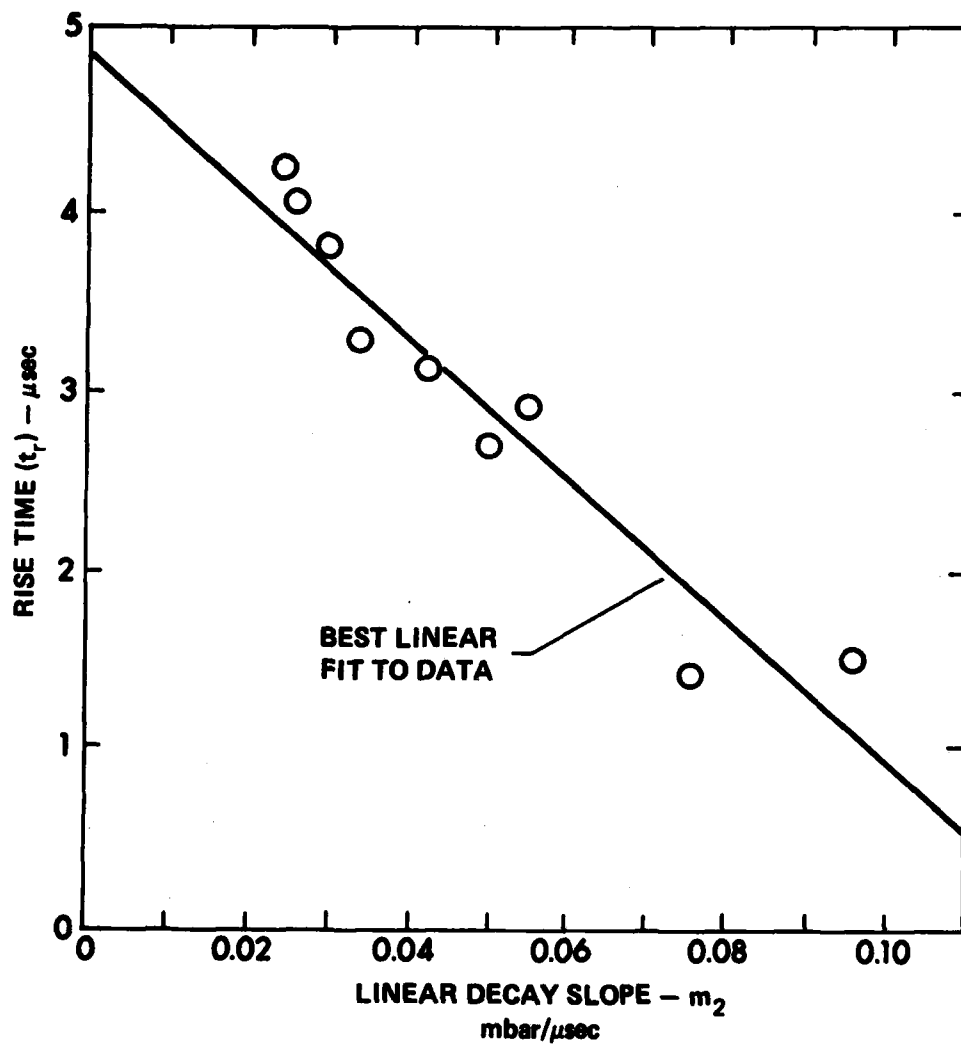


FIGURE 5.3  
CONSTANT PEAK AMPLITUDE RUN

equal to that predicted by the relaxation model, provided, of course, that the amplitude were low enough.

## 2. Slope of the Rise ( $m_1$ ) versus Peak Pressure Squared

### a. Constant Spark Energy

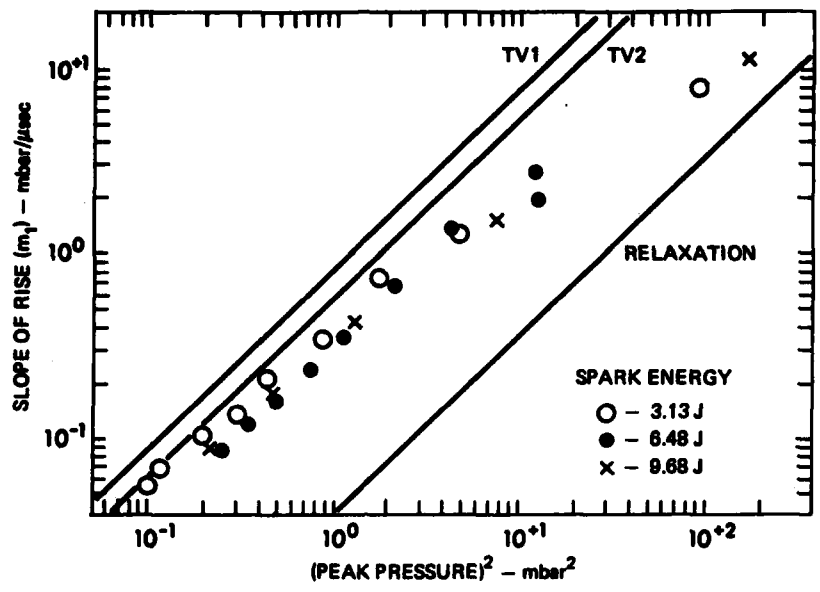
Again we find that our data fits better with the thermoviscous model (TV2) than with the relaxation model (see Fig. 5.4(a)). In this method of analysis the data points seem to fall closer together and the slope of a least squares fit is similar to the slope of the thermoviscous lines. There are a few points at very high peak pressures that fall near the relaxation line. However, the relaxation model is only valid for peak pressures under 1 mbar (see Chapter 2). Therefore we cannot compare these points with the results from the relaxation model. A better explanation for these points is that the rise is so fast at high amplitudes that we are approaching the limit of our experimental apparatus.

### b. Constant Half Duration

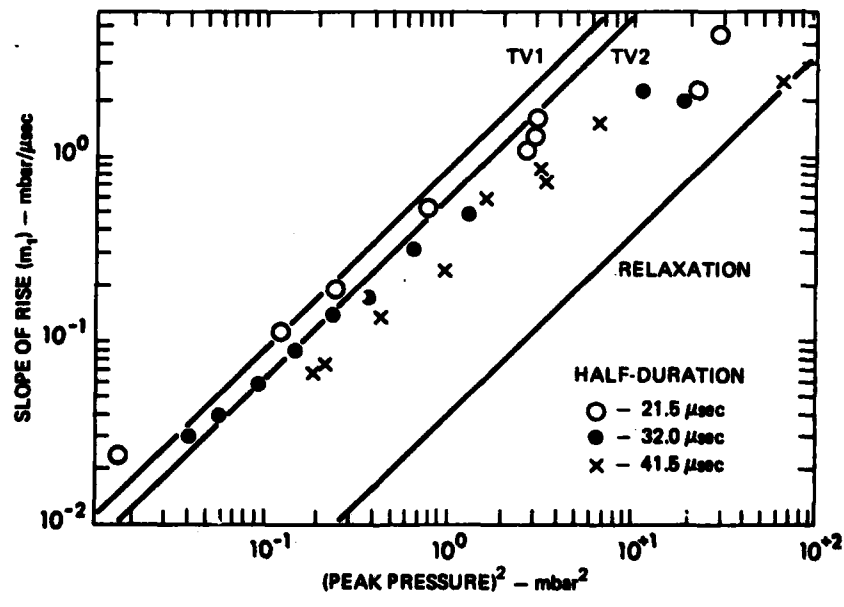
The effects of a lengthened half duration are not as pronounced in this method of analysis as in the previous method. A plot of the same constant half duration runs is shown in Fig. 5.4(b). However, it is still evident that as the half duration increases, the data seem to fall closer to the relaxation theory line. Again we have those few data points above  $3.2 \text{ mbar}^2$  that seem to "bend" towards the relaxation line. This is probably due to limitations of our apparatus.

### c. Comparison with Computer Propagation Algorithm

The results from the propagation algorithm can only be conveniently compared with data from our constant spark energy runs. We obtained very good agreement between our experimental waveforms and the



(a) CONSTANT SPARK ENERGY



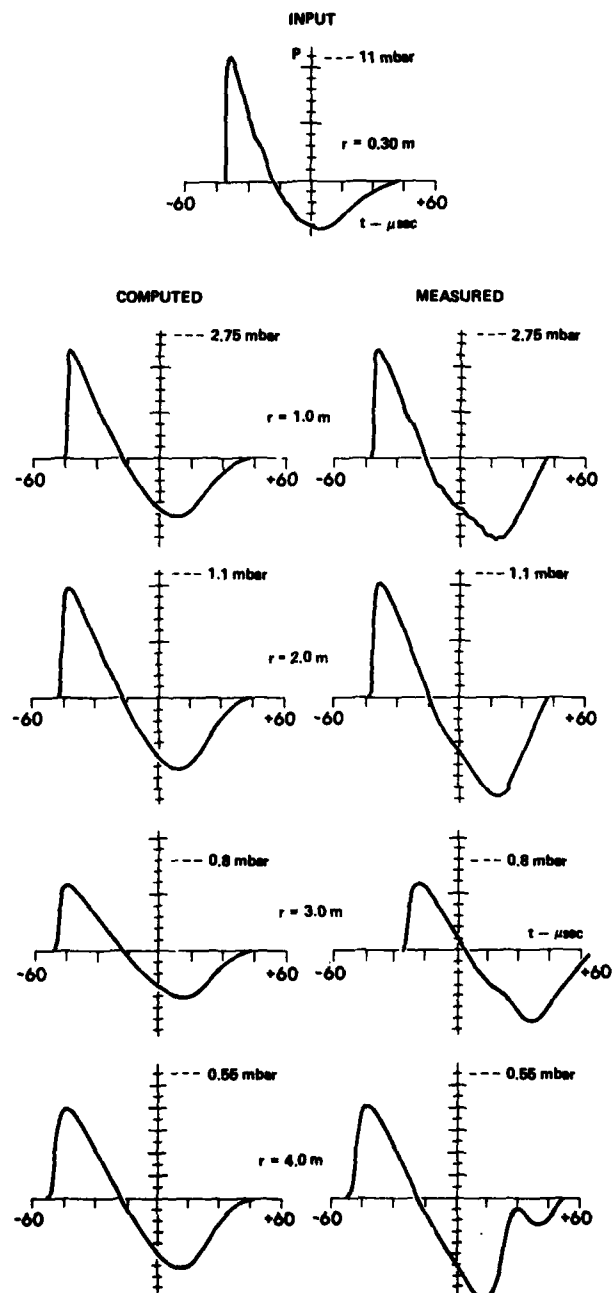
(b) CONSTANT HALF-DURATION

FIGURE 5.4  
SECOND METHOD OF COMPARISON

computed waveforms, in terms not only of general wave shape but of amplitude, half duration, and rise time. A comparison of one particular run is shown in Fig. 5.5. If we plotted the data from the computed waveforms in Fig. 5.1, the points would fall very close to the x's. Agreement is poor for the second half of the N wave, because the second half of our experimental N waves tend to be contaminated by reflected and/or diffracted signals. The maximum error in amplitude was 8.5% and the maximum error in half duration was 2.0%. Since we took our experimental data using several sparks, it is not surprising that we found some small error. In addition to spark variability, there is some error in the calibration process. The maximum error in rise time is 27%. This is a relatively large error. Most of the error can be directly attributed to error in measuring the amplitude because the slope of the head shock  $m_1$  was found to be very nearly the same for both experimental and computed waveforms. The percentage error between measured and predicted rise times is given in Table 5.2 for all four models.

TABLE 5.2  
PERCENTAGE DIFFERENCE BETWEEN  
EXPERIMENTAL AND COMPUTED RISE TIMES

r(cm)	TV1	TV2	RELAXATION	PROPAGATION ALGORITHM
30	81.91	74.27	- 155.6	----
100	52.84	32.84	- 566.45	25.4
200	27.56	- 3.10	- 922.73	26.6
300	18.61	-15.87	-1049.50	23.4
400	15.66	-23.92	-1091.43	23.1



**FIGURE 5.5**  
**COMPARISON OF MEASURED AND COMPUTED WAVEFORMS**  
**SPARK ENERGY = 9.68 J**

We attribute the success of our algorithm to the fact that it was able to accommodate the real N wave signal. A step shock did not have to be assumed. It is concluded that the half durations of the N waves used in our experiment are not long enough for our measurements to fairly test the step shock predictions.

The agreement between our experimental and computed waveforms led us to suspect that, despite the apparently poor showing in Figs. 5.1 and 5.2, relaxation does have an appreciable effect on the waveforms. In order to check this possibility, we ran the computer algorithm using the following absorptions: thermoviscous alone, thermoviscous and relaxation (including dispersion), and relaxation (including dispersion) alone. The computer runs were made using the same input waveform and initial conditions as the run shown in Fig. 5.5. Several representative waveforms are shown in Fig. 5.6. For  $r=1.5$  m, the slope of the head shock for the thermoviscous-only and relaxation-only cases is steeper than the slope for the combination case. However, the slope for the thermoviscous-only case is much closer to that of the combination case. Therefore, we concluded that thermoviscous absorption is playing a dominant role at  $r=1.5$  m. As the propagation distance ( $r$ ) increases, the slope of the head shock for the relaxation-only case decreases faster than that for the thermoviscous-only case. By the time we reach  $r=5.0$  m the slope of the head shock for the relaxation-only case is very close to that for the combination case. In the thermoviscous-only waveform, however, the head shock is much steeper. We therefore conclude that relaxation plays the dominant role in determining the head shock at  $r=5.0$  m.

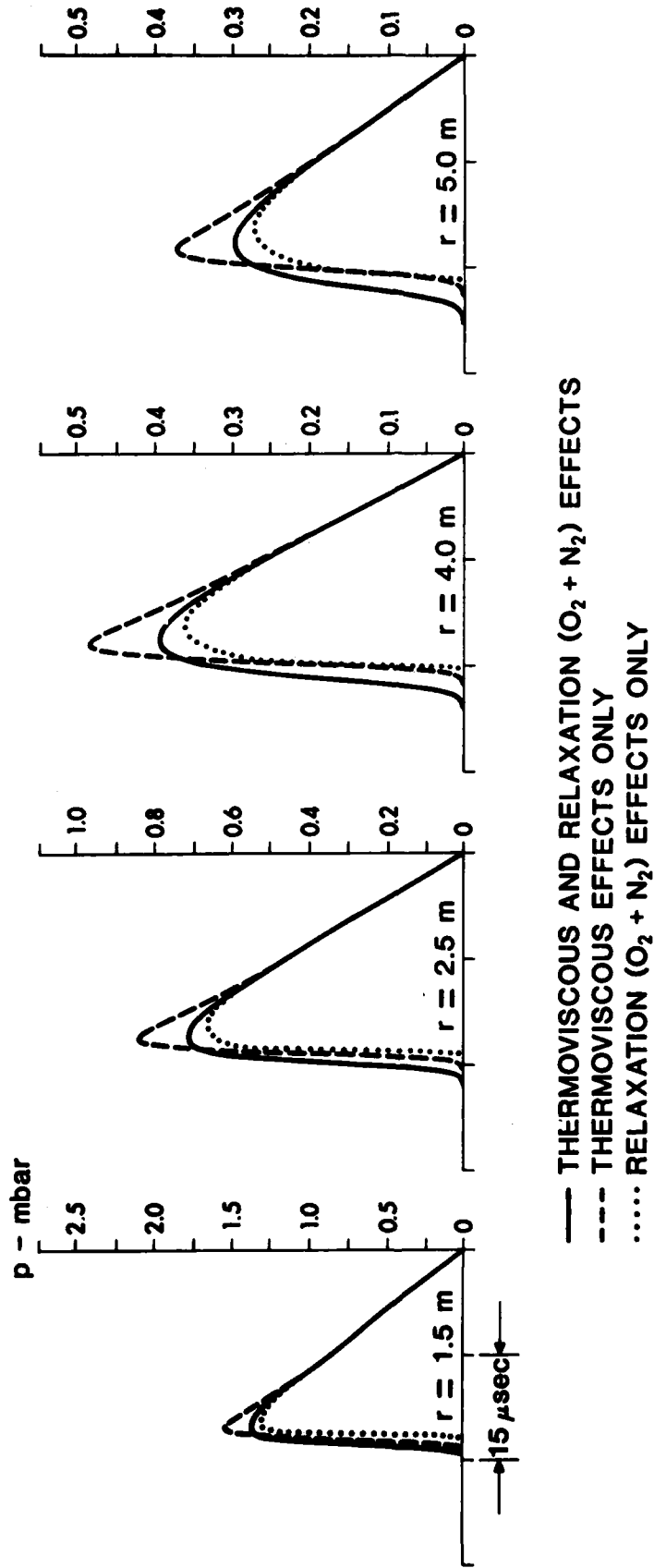
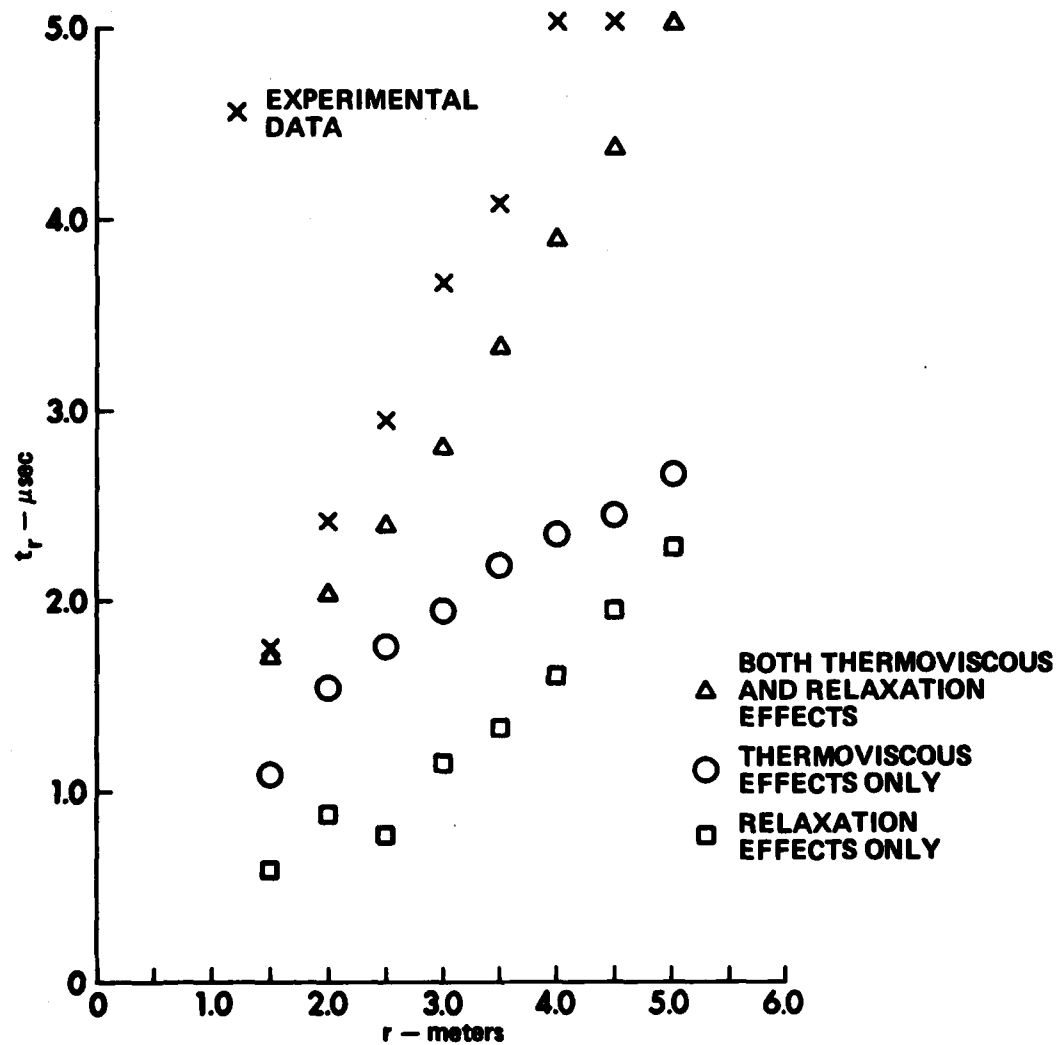


FIGURE 5.6  
COMPUTED WAVEFORMS FOR VARIOUS ABSORPTION MECHANISMS

The emerging role played by relaxation as the N wave becomes weaker can also be seen clearly in Fig. 5.7. Here we plot rise time versus propagation distance for all three cases and for the experimental data. As the propagation distance increases, the thermoviscous-only rise time increases more slowly, while the relaxation-only rise time increases more quickly.

An explanation for our findings is as follows. The frequency spectrum for an ideal N wave ( $t_r=0$ ) is proportional to  $|j_1(\omega T)|$ , where  $j_1$  is the spherical Bessel function of the first kind and order.<sup>39</sup> The high frequency envelope of the spectrum falls off at 6 dB/octave. If the N wave has a finite rise time, however, the envelope first falls at 6 dB/octave and then changes to a 12 dB/octave slope. The slope change occurs at a frequency that is approximately  $1/t_r$ .<sup>40</sup> Thus, as the rise time of the N wave increases, there is less and less high frequency energy. It is well known that for frequencies clearly above the relaxation frequency of the medium the dominant absorption mechanism is thermoviscous whereas for frequencies clearly below the relaxation frequency the dominant mechanism is relaxation. Near the relaxation frequency there is a sort of "saddle" region in which both mechanisms are important. For the particular temperature and humidity we used in our computer run, the relaxation frequency is about 74 kHz. The point at which relaxation absorption and thermoviscous absorption are equal is about 160 kHz, which corresponds to a rise time of 6.25  $\mu$ sec. Most of our rise times fall between 1.5 and 6.25  $\mu$ sec. At each end one of the absorption mechanisms dominate. In the middle, both mechanisms seem to affect the rise time of our N waves.



**FIGURE 5.7**  
**RISE TIME versus DISTANCE FOR VARIOUS**  
**ABSORPTION MECHANISMS**

CHAPTER 6  
CONCLUSIONS AND RECOMMENDATIONS  
FOR FURTHER WORK

An experiment has been carried out to measure the rise time of spherically spreading N waves produced in air by sparks. The main question is whether the rise time was determined by oxygen relaxation. For the N waves measured--amplitudes in the range 0.15-15 mbar and half durations in the range 7.5-41.5  $\mu$ sec--a conclusive answer to this question was not found. It did appear, however, that in many cases the amplitudes were so large that the shocks were, at best, only partly dispersed.

In the experiment, N waves were produced by means of an electric spark which was mounted on an optical bench. Waveforms were captured at specific source-receiver distances with a condenser microphone (of very wide bandwidth) and a digital oscilloscope. Data was taken under three different conditions: constant spark energy, constant half duration, and constant amplitude. The waveforms captured during these runs were analyzed to determine their rise time.

We have reviewed two analytical models used to predict the rise time of a step shock, the thermoviscous model and the relaxation model. Previous investigators have used these models to predict the rise time of sonic boom N waves. Since the sonic boom has a very long half duration ( $\approx 0.2$  sec), a step shock is a good approximation for it. Our N waves, however, have such a short half duration ( $\approx 20$   $\mu$ sec) that a step shock is hardly a good approximation for them. When we initially compared our

experimental rise times with those predicted by the models, we found that the experimental data seemed to fit the thermoviscous model better than the relaxation model. This finding should not be weighed heavily, however, because of the questionable applicability of the two analytical models.

In our comparisons using the constant half duration runs we noticed a curious pattern. As the half duration increased so did the rise time. This pattern was confirmed when we obtained a similar result using the constant amplitude run data. The discovery of this pattern put the initial findings described above in question. There was still a chance that the effects of oxygen and/or nitrogen relaxation were important but were masked by the assumption that an N wave could be approximated by a step shock.

In order to obtain theoretical predictions valid for our N waves, we took a direct approach to the problem. We used a wave propagation computer algorithm in which the effects of atmospheric absorption (and dispersion) and nonlinear propagation distortion are calculated directly. This algorithm is ideal for dealing with our N waves because it is designed to accommodate arbitrary waveforms. Given an experimentally measured N wave at a specified distance, our wave propagation algorithm predicts the shape of the N wave at subsequent distances. Atmospheric absorption was calculated using a digital implementation of the American National Standard Institute (ANSI) document S1.26-1978. The absorption calculation includes the effects of viscosity, heat conduction, and vibrational relaxation of oxygen and nitrogen molecules. Dispersion due to oxygen relaxation was also included. Nonlinear distortion

was calculated using standard theory of finite amplitude waves. The computed waveforms were compared with the experimental waveforms. The amplitude, half duration, and rise time were in good agreement for all the waveforms.

It is concluded that the existing thermoviscous and relaxation models, which are for step shocks, cannot be used to predict the rise time of short half-duration N waves. As for oxygen relaxation, the evidence is that it does have some effect on the rise time of our N waves. Computer calculations in which the thermoviscous and relaxation effects could be included or omitted show that the measured rise times cannot be attributed to either mechanism alone. Both mechanisms are important for the N waves for our experiments.

Our recommendation for further work is twofold. First, true solutions for spherically spreading N waves should be obtained for the thermoviscous and relaxing media. Our experimental results could then be used to test the solutions. Second, our experiment should be carried out with N waves of longer half duration and smaller amplitude. A greater range of results will be useful for checking theoretical predictions.

APPENDIX A

DERIVATION OF THE EQUATION OF STATE FOR A RELAXING MEDIUM<sup>28</sup>

A sound wave passing through a relaxing medium may cause a change in the thermodynamic equilibrium of the fluid. We introduce an "internal coordinate"  $\xi$  to account for these changes. If  $p = p(\rho)$  in a nonreacting medium, then for a relaxing medium we must write

$$p = p(\rho, \xi) \quad . \quad (A.1)$$

The Taylor series expansion of Eq. (A.1) is

$$p = (p - p_0) = \left( \frac{\partial p}{\partial \rho} \right)_{\xi} \rho' + \frac{1}{2} \left( \frac{\partial^2 p}{\partial \rho^2} \right)_{\xi} \rho'^2 + \left( \frac{\partial p}{\partial \xi} \right)_{\rho} \delta \xi \quad , \quad (A.2)$$

where  $\delta \xi = (\xi - \xi_0)$ ,  $\rho' = (\rho - \rho_0)$ , and  $\left( \frac{\partial p}{\partial \rho} \right)_{\xi}$  is the square of the frozen sound speed ( $c_f^2$ ). The relaxation (rate) equation is usually written

$$-\tau \frac{d\xi}{dt} = \xi - \xi_0 \quad ,$$

where  $\tau$  is the relaxation time of the medium and  $\xi_0$  is the equilibrium state of the internal coordinate. But it is necessary to take into account the dependence of  $\xi_0$  on density,

$$\xi_0 = \xi_{00} + \frac{\partial \xi_0}{\partial \rho} \rho' \quad ,$$

where  $\xi_{00}$  is the value of the internal coordinate undisturbed by the wave. The relaxation equation with density varying because of the presence of the sound wave is therefore

$$-\tau \frac{d\xi}{dt} = \xi - \xi_{00} - \frac{\partial \xi_0}{\partial \rho} \rho' \quad ,$$

or, if  $\delta\xi$  stands for  $\xi - \xi_{00}$ ,

$$\delta\xi = -\tau \xi_t + \frac{\partial \xi_0}{\partial \rho} \rho' \quad . \quad (A.3)$$

Substituting Eq. (A.3) into the last term on the right hand side of Eq. (A.2), we find that

$$p = \left[ c_f^2 + \frac{\partial \xi_0}{\partial \rho} \left( \frac{\partial p}{\partial \xi} \right)_\rho \right] \rho' + \frac{1}{2} \left( \frac{\partial^2 p}{\partial \rho^2} \right)_\xi \rho'^2 - \tau \left( \frac{\partial p}{\partial \xi} \right)_\rho \frac{d\xi}{dt} \quad . \quad (A.4)$$

If  $\xi$  is constant, i.e., the fluid is in equilibrium, the last two terms on the right hand side of Eq. (A.4) become zero. Thus, it can be seen that

$$\left[ c_f^2 + \frac{\partial \xi_0}{\partial \rho} \left( \frac{\partial p}{\partial \xi} \right)_\rho \right]$$

is equivalent to  $c_0^2$ . Substituting this result Eq. (A.4) now becomes

$$p = c_0^2 \rho' + \frac{1}{2} \left( \frac{\partial^2 p}{\partial \rho^2} \right)_\xi \rho'^2 - \tau \left( \frac{\partial p}{\partial \xi} \right)_\rho \frac{d\xi}{dt} \quad . \quad (A.5)$$

Taking the time derivative of Eq. (A.2) and multiplying by  $\tau$  we find that

$$\tau \frac{dp}{dt} = \tau c_f^2 \frac{d\rho'}{dt} + \frac{1}{2} \tau \left( \frac{\partial^2 p}{\partial \rho^2} \right)_\xi \frac{d\rho'^2}{dt} + \tau \left( \frac{\partial p}{\partial \xi} \right)_\rho \frac{d\xi}{dt} \quad . \quad (A.6)$$

Add Eqs. (A.5) and (A.6) to obtain

$$\left(1 + \tau \frac{d}{dt}\right) p = c_0^2 \rho' + \frac{1}{2} \left(\frac{\partial^2 p}{\partial \rho^2}\right)_\xi \left(1 + \tau \frac{d}{dt}\right) \rho'^2 + \tau c_f^2 \frac{d\rho'}{dt} .$$

Now, add and subtract  $(c_0^2) d\rho'/dt$  from the right hand side to obtain

$$\left(1 + \tau \frac{d}{dt}\right) p = \left(1 + \tau \frac{d}{dt}\right) \left[ c_0^2 \rho' + \frac{1}{2} \left(\frac{\partial^2 p}{\partial \rho^2}\right)_\xi \rho'^2 \right] + m \tau c_0^2 \frac{d\rho'}{dt} ,$$

where  $m = (c_f^2 - c_0^2)/c_0^2$ . This is Eq. (2.7), the nonlinear equation of state for a relaxing but inviscid, non heat-conducting medium.

APPENDIX B  
PROGRAM AND SUBROUTINE LISTINGS

Listings for Program LB01, Function DABSORP and Subroutines RESAMP, NWPLOT, FQPLOT, APWT, and TAYLOR are presented in this appendix. Program LB01 is used to compute propagated waveforms from a given direct waveform. Function DABSORP is used to compute atmospheric absorption and dispersion due to oxygen relaxation in accordance with ANSI Standard S1.26-1978. Subroutine RESAMP resamples the data points in equal time increments. Subroutines NWPLOT and FQPLOT are used to plot the computed waveforms in the time domain and the frequency domain, respectively. Subroutines APWT and TAYLOR are used to accurately find the frequency components of the N wave.

```

C      PROGRAM LB01 (NDATA,PLOT=0,INPUT,OUTPUT,RFSULT=0,TAPE2=NDATA)
C      CCCCCCCCCCCCCCCCCCCCCCCCCCCCCCCCCCCCCCCCCCCCCCCCCCCCCCCCCCCCC
C      THIS PROGRAM IS A WAVE PROPAGATION ALGORITHM. IT APPLIES
C      ABSORPTION AND DISPERSION ACCORDING TO THE ANSI S1.26-1978
C      STANDARD. NONLINEAR DISTORTION IS APPLIED USING WEAK SHOCK
C      THEORY.
C      PARAMFTFRS:
C      P - AMPLITUDE ARRAY
C      T - TIME ARRAY
C      N - NUMBER OF POINTS
C      NP - NUMBER OF PROPAGATIONS
C      X - PROPAGATION DISTANCE ARRAY
C      IOPT - THE PLOT OPTION
C      IF IOPT=0 THE FREQUENCY SPECTRUM IS PLOTTED
C      IF IOPT=1 THE TIME WAVEFORM IS PLOTTED
C      IF IOPT=2 BOTH ARE PLOTTED
C      FCOR - CONVERSION FACTOR FROM VOLTAGE TO PRESSURE
C      CCCCCCCCCCCCCCCCCCCCCCCCCCCCCCCCCCCCCCCCCCCCCCCCCCCCCCCCCCCCC
C      DIMENSION P(1500),T(1500),IWK(9150),WK(9150),X(20)
C      COMPLEX A(1500),ALFA(751)
C      EQUIVALENCE(WK(1),IWK(1))
C      DATA IRESULT,DELTA,AXSTP/6LHESULT,0.5E-6,0.9R77,6/
C      PRINT*,#INPUT # OF PTS IN WVF. # OF PROPS. (INCLUDING ORIG.)#
C      READ*,N,NP
C      PRINT*,#INPUT PROPAGATION DISTANCES INCLUDING INITIAL N-WAVE
C      DISTANCES#
C      DO 10 J=1,NP
C      READ*,X(J)
C      PRINT*,#INPUT # OF MICROSECONDS PER INCH ON X-AXIS#
C      READ*,THIC
C      PRINT*,#INPUT THE PLOTTING OPTION. IOPT (0,1,2)#
C      READ*,IOPT
C      PRINT*,#INPUT FRACTIONS OF MAXIMUM AMPLITUDE USED FOR SLOPE
C      CALCULATION#

```

```

C      READ*,F1,F2
C      DO 20 J=1,N
C      READ(2,*) P(J)
C
C      READ(2,*) FCON,TEMP,PRES,RH,PNORM
C
C      PRINT(IRESULT,*)N,NP,FCON,TEMP,PRES,RH,PNORM,F1,F2
C      DO 30 J=1,N
C      T(J)=(J-1)*DELTA
C      P(J)=P(J)*FCON
C      RN=X(I)
C
C      CCCCCCCCCCCCCCCCCCCCCCCCCCCCCCCCCCCCCCCCCCCCCCCCCCCCCCCCCCCCCC
C      IN THIS SECTION THE ABSORPTION AND DISPERSION COEFFICIENTS
C      ARE CALCULATED.
C
C      NF= N/2*1
C      IERR=0
C      DELF=1./((N-1)*DELTA)
C
C      DO 40 J=1,NF
C      F=NFLE*J
C      ALP="NABSORP(TEMP,PRES,RH,F,FRO,0ALPH)"
C      ALY=0ALPH*F/FRO
C      ALFA(J)=CMPLX(ALR,ALI)
C      CONTINUE
C      40
C      CCCCCCCCCCCCCCCCCCCCCCCCCCCCCCCCCCCCCCCCCCCCCCCCCCCCCCCCCCCCCC
C      IF (IOPT.EQ.1.OR.IOPT.EQ.2) CALL NWPL0T(P,T,M,PNORM,IRESULT,
C      1TMC,RN)
C
C      IFIRST=1
C      DO 110 I=2,NP
C      ISFT=i
C      CONTINUE
C      55
C
C      THE STEP SIZE IS CALCULATED
C      CALL NWSLOPE (P,DELTA,N,F1,F2,SLOPE,IERR)
C      SST=RN*(EXP(AXSTP/(RN*SLOPE))-1)
C      IF ((RN*SSI).GT.X(I)) SSI=X(I)-RN

```



```

C CCCCCCCCCCCCCCCCCCCCCCCCCCCCCCCCCCCCCCCCCCCCCCCCCCCCCCCCC
C NR=N-I
C THE POINTS ARE RESAMPLED SO THAT THERE ARE EQUAL TIME
C INCREMENTS BETWEEN THEM.
C CALL RESAMP(P,T,MK,NR,NDELT,IERR)
90 IF(YERR.EQ.0) GOTO 100
PRINTO,PERRR IN RESAMP IERR=#,IERR
PRINTO,PRN= #,RN
STOP
C CONTINUE
100 T(N)=T(N-1)*DELTY
P(N)=0.
RNT=RN*.1*SSI
IF(RNT.LT.X(I)) GOTO 55
C IF(TOPT.EQ.1.OR.IOPT.EQ.2) CALL NMPLOT(P,T,N,PNORM,IRESULT,
1TMC,RN)
CONTINUE
110 STOP
C CONTINUE
120 PRINTO,#SHOCK AT#,J
STOP
ENN

```

```

C      FUNCTION DABSORP(T,P,RH,F,FRO,ALPH)
C      PROGRAM CALCULATES ATMOSPHERIC ABSORPTION COEFFICIENT
C      ALGORITHM FROM FORMULAS GIVEN BY H. E. BASS IN WYLE LAR REPORT 72-2
C      P      FREQUENCY (HZ)
C      P      ATMOSPHERIC PRESSURE (ATMOSPHERES)
C      I      AIR TEMPERATURE (DEGREES KELVIN)
C      MH     RELATIVE HUMIDITY (PERCENT)
C      SOLUTION IN DRY/METER
C      ACCURACY OF SOLUTION
C      * OR - 5 PERCENT FOR T FROM 273 TO 313
C      RH FROM 0 TO 100
C      F FROM 50 HZ TO 10 MHZ
C      P FROM .03 TO 1 ATM
C      F/(P/P0) MUST BE LESS THAN 10MHZ
C      T1=273.16
C      RATIO=T1/T
C      ARG1=-8.29692*(1./RATIO-1.)
C      ARG2=4.76955*(1.-RATIO)
C      ARG3=10.79586*(1.-RATIO)-5.02808*ALOG10(1./RATIO)+1.50474F-04*
C      1 (1.-10**ARG1) +4.2873E-04*(10**ARG2-1.)-2.2195983
C      PSP=10**ARG3
C      H=RH*P/P
C      FRO=P*(24.+4.41E+04*((.05+H)/(.391+H))*H)
C      TRATIO=T/293.15
C      FRN=P/SORT(TRATIO)*(9.+350.*H*EXP(-6.142*(TRATIO**1
C      1 -.333333333333))-1.))
C      ARG4=R.6859*SORT(TRATIO)*(F**2.)/P
C      ARG5=2.1913E-04/TRATIO*(1239./T)**2.*EXP(-2239./T)
C      ARG6=1.84E-11*.1619E-04/THATIO**((J352./T)**2.)*EXP(-3352./T)/
C      1 (F*H**F**2./FRN)
C      ALPH=ARG4**ARG5
C      DABSORP=ARG4*(ARG5+ARG6)
C      RETURN
C      END

```









91/06/10. 16.4].64

FTN 4.8+52R

73/171 OPT=2

SUBROUTINE APWT

```

1 SUBROUTINE APWT(WT, NP, KFCN, XP, GI)
2 DIMENSION WT(1)
3
4 *****
5 APWT -- COMPUTES NP APERTURE SHADING COEFFICIENTS, SYMMETRIC ABOUT APWT
6 APERTURE CENTROID. THE AVAILABLE WEIGHT FUNCTIONS ARE -
7 KFCN (BCD) / DESCRIPTION
8 HANNING, OR EXTENDED COSINE. (FLAT TOP W/APWT
9 COSINE TAPER.)
10 COSINE**2
11 XP IS TOTAL PERCENT OF COSINE TAPER.
12 COSINE**2
13 XP IS ARGUMENT MAXIMUM. IN DEGREES. (47.5
14 IMATES FLNR.)
15 TAYLOR
16 XP IS PEAK SLOPE RATIO. POSITIVE.
17 GI IS INVERSE GAIN FACTOR OF ARRAY. ALL WEIGHTS ARE NORMALIZED TO APWT
18 *****
19 NP=NP
20 CALL SET1 (WT(1), WT(NP), 1.0)
21 WTACC=NP
22 PI=3.141592654
23 IF (KFCN.EQ.#HANNING#) GO TO 10
24 IF (KFCN.EQ.#COSINE**2#) GO TO 40
25 IF (KFCN.EQ.#TAYLOR#) GO TO 60
26 GO TO 80
27
28 ***** HANNING WEIGHT.
29
30 C
31 10 XNP2=NP*XP/200.
32 NP2=XNP2
33 IF (NP2.EQ.0) GO TO 30
34 DO 20 IP=1, NP2
35 JP=NP+1-IP
36 THETA=PI*(XNP2-IP)/XNP2
37 WTX=(1.0+COS(THETA))/2.
38 WT(IP)=WTX
39 WTACC=WTACC+2.0+2.0*WTX
40

```





91/06/10. 16.41.44

TAYLOR 40  
 TAYLOR 41  
 TAYLOR 42  
 TAYLOR 43  
 TAYLOR 44  
 TAYLOR 45  
 TAYLOR 46  
 TAYLOR 47  
 TAYLOR 48  
 TAYLOR 49  
 TAYLOR 50  
 TAYLOR 51  
 TAYLOR 52  
 TAYLOR 53  
 TAYLOR 54

FTN 4.R.52A

ROUTINE TAYLOR 73/17) OPT=2

```

40 NP2=(NP+1)/2
   NP=2./(NP-1)
   P=1.0
   DO 50 I=1,NP2
     J=NP+1-I
     T=0.0
     DO 40 M=1,NRARM1
       T=T+FM*FM*P*P*SCALE
     T=I*T
     T(I)=T
   T(I)=T
50 P=P-DM
   RETURN
   C
   END

```

## REFERENCES

1. W. D. Hayes, R. C. Haefeli, and H. E. Kulsrud, "Sonic Boom Propagation in a Stratified Atmosphere with Computer Program," NASA CR-1299, National Aeronautics and Space Administration, Washington, D.C., 1969.
2. W. D. Hayes and H. L. Runyan, Jr., "Sonic-Boom Propagation through a Stratified Atmosphere," Proceedings of the Second Sonic Boom Symposium, Houston, Texas, 3 November 1970, p. 25.
3. A. D. Pierce, "Spikes on Sonic-Boom Pressure Waveforms," J. Acoust. Soc. Am. 44, 1052-1061 (1968).
4. A. D. Pierce, "Statistical Theory of Atmospheric Turbulence Effects on Sonic-Boom Rise Times," J. Acoust. Soc. Am. 49, 906-924 (1971).
5. J. P. Hodgson and N. H. Johannesen, "Real-Gas Effects in Very Weak Shock Waves in the Atmosphere and the Structure of Sonic Bangs," J. Fluid Mech. 50, Part 1, 17-20 (1971).
6. N. H. Johannesen and J. P. Hodgson, "The Physics of Weak Waves in Gases," Rep. Prog. Phys. 42, 629-676 (1979).
7. American Institute of Physics, New York, "American National Standard Method for the Calculation of the Absorption of Sound by the Atmosphere," S1.26-1978/ASA 23, 1978.
8. G. G. Stokes, "On a Difficulty in the Theory of Sound," Philos. Mag. 33 (Series 3), 349-356 (1848).
9. S. D. Poisson, "Mémoire sur la Théorie du Son," J. de l'École Polytechnique 7, 319 (1808).

10. W. J. M. Rankine, "On the Thermodynamic Theory of Waves of Finite Longitudinal Disturbance," *Philos. Trans. Roy. Soc.* 160 277-288 (1870).
11. Lord Rayleigh, "Aerial Plane Waves of Finite Amplitude," *Proc. Roy. Soc., London, Ser. A*, 84, 247-284 (1910).
12. G. I. Taylor, "The Conditions Necessary for Discontinuous Motion in Gases," *Proc. Roy. Soc., London, Ser. A*, 84, 371-377 (1910).
13. J. M. Burgers, "A Mathematical Model Illustrating the Theory of Turbulence," *Advances in Applied Mechanics*, Vol. I, edited by R. von Mises and T. von Karman (Academic Press, New York, 1948), pp. 171-199.
14. E. Hopf, "The Partial Differential Equation  $u_t + uu_x = u_{xx}$ ," *Commun. Pure Appl. Math.* 3, 201-230 (1950).
15. J. D. Cole, "On a Quasi-Linear Parabolic Equation Occurring in Aerodynamics," *Quarterly of Applied Mathematics* 9, No. 3, 225-236 (1951).
16. M. J. Lighthill, "Viscosity Effects in Sound Waves of Finite Amplitude," in *Surveys of Mechanics*, edited by G. K. Batchelor and R. M. Davies (Cambridge University Press, Cambridge, 1956).
17. A. L. Polyakova, S. I. Soluyan, and R. V. Khokhlov, "Propagation of Finite Disturbances in a Relaxing Medium," *Sov. Phys.-Acoust.* 8 (1962).
18. H. Ockenden and D. A. Spence, "Non-Linear Wave Propagation in a Relaxing Gas," *J. Fluid Mech.* 39, Part 2, 329-345 (1969).

19. C. L. Morfey, "Absorption of Sound Waves in the Atmosphere," AGARD Report No. 686, Section 9, Special Course on Acoustic Wave Propagation, NATO, Advisory Group for Aerospace and Development, Neuilly, Sur Seine, France, 1979 (ADA 077420).
20. J. F. Clarke and J. B. Rodgers, "Shock Waves in a Gas with Several Relaxing Internal Energy Modes," J. Fluid Mech. 21, Part 4, 591-610 (1965).
21. D. G. Crighton and J. F. Scott, "Asymptotic Solutions of Model Equations in Nonlinear Acoustics," Philos. Trans. Roy. Soc., London, Ser. A, 292 (1979).
22. H. Honma, I. I. Glass, O. Holst-Jensen, and Y. Tsumita, "Weak Spherical Shock-Wave Transitions of N-Waves in Air with Vibrational Excitation," 13th International Symposium on Shock Tubes and Waves, 7-9 July 1981.
23. H. Honma, I. I. Glass, and Y. Tsumita, "An Application of the Random-Choice Method to Weak Blast Waves," Bull. Inst. Space Aero. Sci., Special Issue No. 3, (in Japanese) 121-136 (1982).
24. Olé Holst-Jensen, "An Experimental Investigation of Rise Times of Very Weak Shock Waves," UTIAS Technical Note No. 229 (CN ISSN 0082-5263), Institute for Aerospace Studies, University of Toronto, March 1981.
25. Wayne M. Wright, "Studies of N Waves from Weak Sparks in Air, Final Report," ONR Report NR-384-321, Physics Department, Kalamazoo College, Kalamazoo, Michigan, June 1971 (AD 725865).
26. M. Greenspan, "Rotational Relaxation in Nitrogen, Oxygen, and Air," J. Acoust. Soc. Am. 31, 55-60 (1959).

27. American Institute of Physics Handbook, 3rd Edition, edited by D. Gray (McGraw-Hill Book Co., Inc., New York, 1972).
28. O. V. Rudenko and S. I. Soluyan, "Propagation of Finite-Amplitude Waves in an Ideal Dissociating Gas," *Sov. Phys.-Acoust.* 16, No. 1 (1970).
29. Frederick M. Pestorius, "Propagation of Plane Acoustic Noise of Finite Amplitude," Applied Research Laboratories Technical Report No. 73-23 (ARL-TR-73-23) (AFOSR-TR-74-0711), Applied Research Laboratories, The University of Texas at Austin, August 1973 (AD 778868).
30. Mark O. Anderson, "The Propagation of a Spherical N Wave in an Absorbing Medium and Its Diffraction by a Circular Aperture," Applied Research Laboratories Technical Report No. 74-25 (ARL-TR-74-25) (AFOSR-TR-74-1736), Applied Research Laboratories, The University of Texas at Austin, August 1974 (AD 787878).
31. Mark A. Theobald, "Experimental Study of Outdoor Propagation of Spherically Spreading Periodic Acoustic Waves of Finite Amplitude," Applied Research Laboratories Technical Report No. 77-5 (ARL-TR-77-5) (AFOSR-TR-77-0521), Applied Research Laboratories, The University of Texas at Austin, January 1977 (ADA 039020).
32. Robert D. Essert, Jr., "Axisymmetric Propagation of a Spherical N Wave in a Cylindrical Tube," Applied Research Laboratories Technical Report No. 81-22 (ARL-TR-81-22), Applied Research Laboratories, The University of Texas at Austin, 4 May 1981 (ADA 099990).

33. D. T. Blackstock, "Generalized Burgers Equation for Plane Waves," 9th International Symposium on Nonlinear Acoustics, Leeds, England, Book of Abstracts, July 1981, p. 7.
34. T. T. Taylor, "Design of Line-Source Antennas for Narrow Beam-Width and Low Side Lobes," IRE Trans. Antennas Propag. AP-3, 16-28 (1955).
35. E. P. Cornet, "Focusing of an N wave by a Spherical Mirror," Applied Research Laboratories Technical Report No. 72-40 (ARL-TR-72-40) (AFOSR-TR-73-0624), Applied Research Laboratories, The University of Texas at Austin, 19 September 1972 (AD 157035).
36. M. J. Crocker, "Measurement of Sonic Boom with Limited Frequency Response Instrumentation: A Theoretical Study," WR Research Staff Report 66-20, Wyles Labs, April 1966.
37. B. A. Davy and D. T. Blackstock, "Measurements of the Refraction and Diffraction of a Short N Wave by a Gas-Filled Soap Bubble," J. Acoust. Soc. Am. 49, 732-737 (1971).
38. Wesley N. Cobb, "Diffraction of a Plane N Wave of Finite Amplitude by a Slit," Applied Research Laboratories Technical Report No. 77-43 (ARL-TR-77-43) (AFOSR-TR-78-0149), Applied Research Laboratories, The University of Texas at Austin, August 1977 (ADA 050410).
39. J. R. Young, "Energy Spectral Density of the Sonic Boom," J. Acoust. Soc. Am. 40, 496-498 (1966).
40. P. B. Oncley and D. G. Dunn, "Frequency Spectrum of N Waves with Finite Rise Time," J. Acoust. Soc. Am. 43, 889-890 (1968).

DISTRIBUTION LIST FOR  
 ARL-TR-82-51  
 UNDER CONTRACT N00014-75-C-0867

<u>Copy No.</u>		<u>Copy No.</u>	
1 - 3	Office of Naval Research Physics Program Office (Code 421) 800 North Quincy Street Arlington, VA 22217		Director, National Bureau of Standards Department of Commerce Washington, DC 20234 Attn: Technical Library
		28	
4	Office of Naval Research Director, Technology (Code 200) 800 North Quincy Street Arlington, VA 22217	29 - 31	Commanding Officer Office of Naval Research Western Regional Office 1030 East Green Street Pasadena, CA 91101
	Director Defense Advanced Research Projects Agency 1400 Wilson Blvd. Arlington, VA 22209	32 - 34	Commanding Officer Office of Naval Research Eastern/Central Regional Office 666 Summer Street Boston, MA 02210
5 - 7	Attn: Technical Library		
	Naval Research Laboratory Department of the Navy Washington, DC 20375		Commandant of the Marine Corps Washington, DC 20380
8 - 10	Attn: Technical Library	35	Attn: Scientific Advisor (Code RD-1)
11 - 13	Office of the Director of Defense Research and Engineering Information Office Library Branch The Pentagon Washington, DC 20301	36	Naval Ordnance Station Indian Head, MD 20640 Attn: Technical Library
		37	Naval Postgraduate School Monterey, CA 93940 Attn: Technical Library (Code 0212)
14 - 15	U. S. Army Research Office Box 12211 Research Triangle Park, NC 27709		
		38	Naval Missile Center Point Mugu, CA 93010 Attn: Technical Library (Code 5632.2)
16 - 27	Defense Technical Information Center Cameron Station, Bldg. 5 5010 Duke Street Alexandria, VA 22314	39	Naval Ordnance Station Louisville, KY 40214 Attn: Technical Library

Dist. List for ARL-TR-82-50 (cont'd)

<u>Copy No.</u>		<u>Copy No.</u>	
40	Commanding Officer Naval Ocean Research & Development Activity NSTL Station, MS 39529 Attn: Technical Library	51	Air Force Weapons Laboratory Kirtland Air Force Base Albuquerque, NM 87117 Attn: Technical Library
41	Naval Explosive Ordnance Disposal Facility Indian Head, MD 20640 Attn: Technical Library	52	Air Force Avionics Laboratory Air Force Systems Command Wright-Patterson Air Force Base Dayton, OH 45433 Attn: Technical Library
42	Naval Ocean Systems Center Department of the Navy San Diego, CA 92152 Attn: Technical Library	53	Lawrence Livermore Laboratory University of California P. O. Box 808 Livermore, CA 94550 Attn: Dr. W. F. Krupke
43	Naval Surface Weapons Center White Oak Laboratory Department of the Navy Silver Spring, MD 20910 Attn: Technical Library	54	Harry Diamond Laboratories 2800 Powder Mill Road Adelphi, MD 20783 Attn: Technical Library
44	David W. Taylor Naval Ship Research and Development Center Department of the Navy Bethesda, MD 20084 Attn: Central Library (Code L42 and L43)	55	Naval Air Development Center Department of the Navy Johnsville Warminster, PA 18974 Attn: Technical Library
45	Naval Avionics Facility Department of the Navy Indianapolis, IN 46218 Attn: Technical Library	56	Naval Weapons Center Department of the Navy China Lake, CA 93555 Attn: Technical Library (Code 753)
46	Director U. S. Army Engineering Research and Development Laboratories Fort Belvoir, VA 22060 Attn: Technical Documents Center	57	Naval Training Equipment Center Department of the Navy Orlando, FL 32813 Attn: Technical Library
47 - 49	ODR&E Advisory Group on Electron Devices 201 Varick Street New York, NY 10014	58	Naval Underwater Systems Center New London Laboratory Detachment Technical Center New London, CT 06320
50	Air Force Office of Scientific Research Department of the Air Force Bolling AFB, DC 22209		

Dist. List for ARL-TR-82-50 (cont'd)

<u>Copy No.</u>		<u>Copy No.</u>	
59	Office of Naval Research Resident Representative Room No. 582, Federal Building Austin, TX 78701	69	University of Tennessee Department of Physics Knoxville, TN 37916 Attn: M. A. Breazeale
60 - 61	University of Toronto Institute of Aerospace Studies 4925 Dufferin St. Downsview, Ontario Toronto Canada, M3H 5T6 Attn: I. I. Glass	70	Technical University of Denmark Fluid Mechanics Department Building 404 DK-2800 Lyngby DENMARK Attn: L. Bjørnø
62	Brown University Department of Physics Providence, RI 02912 Attn: R. T. Beyer	71	Yale University Mason Laboratory M4 New Haven, CT 06511 Attn: R. E. Apfel
63 - 64	NASA Langley Research Center Acoustics and Noise Reduction Division Hampton, VA 23365 Attn: J. M. Seiner, Mail Stop 460  W. L. Willshire, Mail Stop 460	72	University of Leeds Department of Mathematics Leeds, Yorkshire, LS2 9JT ENGLAND Attn: David G. Crighton
65	Georgia Institute of Technology School of Mechanical Engineering Atlanta, GA 30332 Attn: A. D. Pierce	73	Institute of Sound Vibration Research The University Southampton SO9 5NH ENGLAND Attn: Dr. C. L. Morfey
66	Kalamazoo College Department of Physics Kalamazoo, MI 49007 Attn: W. M. Wright	74	David R. Kleeman Lockheed Missiles and Space Co. P. O. Box 504 Sunnyvale, CA 94086
67	Naval Postgraduate School Physics and Chemistry Department Monterey, CA 93940 Attn: A. B. Coppens	75	Dr. Akira Nakamura The Institute of Scientific & Industrial Research Osaka University Yamadakami, Suita-Shi Osaka 565 JAPAN
68	New London Laboratory Naval Underwater Systems Center New London, CT 06320 Attn: M. B. Moffett	76	Louis C. Sutherland Wyle Labs 128 Maryland St. El Segundo, CA 90245
		77	Henry E. Bass Department of Physics and Astronomy University of Mississippi University, MS 38677

Dist. List for ARL-TR-82-50 (cont'd)

<u>Copy No.</u>		<u>Copy No.</u>	
78	David F. Pernet National Physical Laboratory Division of Radiation Science and Acoustics Teddington, Middlesex ENGLAND	86	L. Dwynn Lafleur The University of Southwestern Louisiana Department of Physics Lafayette, LA 70504
79	Joseph A. Clark Catholic University of America Mechanical Engineering Department Washington, DC 20064	87	Robert D. Essert Artec Consultants 245 Seventh Avenue Eighth Floor New York, NY 10001
80	Donald B. Cruikshank, Jr. Department of Physics Anderson College Anderson, IN 46011	88	Richard A. Raspet U. S. Army Construction Engineering Research Laboratory Box 4005 Champaign, IL 61820
81	J. A. Gallego-Juárez Instituto de Acústica Centro de Física Aplicada "Leonardo Torres Quevedo" Serrano, 144-Madrid-6 SPAIN	89	N. H. Johannesen Department of the Mechanics of Fluids University of Manchester Manchester M13 9PL ENGLAND
82	T. Kamakura Department of Electrical Engineering Nagoya University Furo-Cho, Chikusa-Ku Nagoya, 464 JAPAN	90	Pia Samuelsson-Fihn IFM Akustibyran AB Dirigentgatan 2 Box 30021 400 43 Göteborg 30 SWEDEN
83	F. Michael Pectorius 7 Brigadier Drive Charleston, SC 29407	91	C. M. Bickerstaff Acoustics Department British Aerospace Brooklands Road Weybridge Surrey KT13 0SF ENGLAND
84	Wesley N. Cobb Yale University Mason Laboratory New Haven, CT 06511	92	Mark Theobald 177 Lexington Street Bellmont, MA 02178
85	David T. Shaw State University of New York at Buffalo Faculty of Engineering and Applied Sciences 4232 Ridge Lea Road Buffalo, NY 14226	93	Mark Schaffer c/o Atlas Air Conditioning Company 5420 Gulfton Houston, TX 77081